Une nouvelle approche basée sur la méthode des éléments finis pour le calcul numérique des propriétés effectives des matériaux composites : méthode des éléments finis du domaine fantôme

Tianlong He

Normandie Université

THÈSE

Pour obtenir le diplôme de doctorat

Spécialité MECANIQUE DES SOLIDES, GENIE MECANIQUE, PRODUCTIQUE, TRANSPORT ET GENIE CIVIL

Préparée au sein de l'Université de Caen Normandie

A new approach based on finite element method for numerical computation of effective properties for composite materials : Phantom Domain Finite Element Method

Présentée et soutenue par
Tianlong HE

Thèse soutenue publiquement le 30/06/2020 devant le jury composé de		
M. ANTOINE LEGAY	Professeur, Conservatoire Nal des Arts et Métiers	Rapporteur du jury
M. PHILIPPE VIDAL	Professeur, IUT VILLE AVRAY (NANTERRE)	Rapporteur du jury
M. DANIEL CHOI	Maître de conférences, Université Caen Normandie	Membre du jury
Mme VÉRONIQUE LAZARUS	Professeur, ENSTA PARIS	Président du jury
M. PHILIPPE KARAMIAN	Maître de conférences HDR, Université Caen Normandie	Directeur de thèse

Thèse dirigée par PHILIPPE KARAMIAN, Laboratoire de Mathématiques 'Nicolas Oresme' (Caen)

UNIVERSITÉ CAEN NORMANDIE

Contents

Introduction

Background

In recent years, composite materials have been widely developed in many industrial sectors such as equipment, construction, medical prostheses, railways, automobile and aeronautics. This development is mainly due to the favorable features of the composites which result from the performances of their constituents. For example, we use thermoplastic composites to meet the environmental requirements while preserving the mechanical properties and to improve the thermal conductivity of these composites. The use of such composites contribute to the reduction of fossil fuel consumption and the reduction of greenhouse gases.

A composite material is an heterogeneous material, composed at least of two different constituents : a matrix, usually serving as a binder, and inclusions made of one or more materials. The inclusions are often called reinforcements as the aim of manufacturing composite materials is to combine the properties of the matrix/inclusions to produce material with different properties from the individual constituents.

An experimental study of composite properties is laborious and difficult. One of the objective of MA team (Modeling and Applications) of LMNO (Nicolas Oresme Mathematical Laboratory) is to develop tools allowing the modeling of composites such as multi-scale numerical homogenization methods. This approach enables the determination of the thermal and elastic properties of composite materials by using finite element methods (FEM) or Fast Fourier Transform (FFT).

High performance computing and the development of innovative numerical methods enable a better understanding of the phenomena involved in the microscopic scale which have an impact on the macroscopic behavior of the composite materials. The work presented in this thesis falls within this framework. The primary objective is to have a fast, reliable and efficient tool capable of calculating the effective properties of composite materials from the thermal and elastic point of view.

Motivation and Contribution

As the composite structure becomes more complex, especially in the cases of tiny inclusions or coated inclusions with a thin film, some difficulties arise: to accurately model such composites, we need a mesh involving a huge number of nodes (especially in three dimensional case) for FEM based methods or a high resolution image for FFT based methods. Although some numerical advances allow the study of very high resolution 3D images, the need to efficiently compute the effective properties of more and more complex composite subsists.

In the case of finite element methods, one difficulty, due to the heterogeneity, is to accurately approximate integrals defining the energy bi-linear form involved in the weak formulation of the homogenization modeling see [7,24,95]. It usually requires a conformal mesh but building such a conformal and periodic mesh with complex composites is not trivial, see for instance [96].

To circumvent the meshing difficulty, an original finite element method, named Phantom domain Finite Element Method (PFEM), is proposed in this thesis. The PFEM relies on computations of integrals with independent meshes based on a Fictitious Domain principle. In other words, one structured mesh is used for the entire domain, including the matrix phase and the inclusions phase. Meanwhile, we use non-structured independent meshes for the inclusions. We then compute integrals defined both on the whole domain and the inclusions. The inclusion meshes will be related to the structured mesh through a substitution matrix. The PFEM Method can be directly applied to inclusions of any kind of shape or geometry, as long as a mesh is available.

We developed the Phantom domain Finite Element Method for Dirichlet and Neumann boundary value problems in both thermal and elastic cases. The main difficulty is to bind the degrees of freedom (DOFs) of the inclusion's mesh to the DOFs of the entire domain's mesh. With isoparametric elements and a structured mesh, it can be achieved by building a substitution matrix. Although the mesh of the inclusion is independent, it should be fine enough to obtain an accurate approximation of the integrals forms. We accomplished a study to find the favorable resolution of the inclusion mesh. Convergence studies and error localization referenced to conformal finite element method are performed to validate and evaluate the PFEM with inclusions of elementary geometry such as disk and square. For square inclusions, in a special case of which the mesh of the entire domain and the mesh of the inclusion are matching, the PFEM will coincide with a conformal FEM. This observation allows us to measure the error produced by the PFEM.

We then extend the PFEM for numerical homogenization, which means the computation of effective properties of composite materials on a represen-

tative volume element (RVE). We employ three type of boundary conditions: Dirichlet, Neumann and periodic boundary conditions. The homogenization development of the PFEM is realized for both thermal conductivity and linear elasticity problems. Numerical experiments are performed for RVE with one spherical inclusion, one cubic inclusion and one ellipsoidal inclusion. Afterwards, in order to show the advantages of the PFEM, we illustrate some cases which are difficult to mesh by conformal finite element method, but can be easily treated by PFEM.

We developed a finite element library code, using object-oriented programming, to perform the computation of the PFEM. The main structure of the code is programmed in Python, while the computation part is programmed in Fortran. A lot of works are devoted to the PFEM code. Several versions of the PFEM code are programmed for the reason of efficiency and for the extension to all the cases involved (thermal, elastic, 2D, 3D, boundary value problems, periodic homogenization etc).

Organization

The rest of this dissertation is organized as follows:

In chapter 1, we present the overview of different analytical and numerical homogenization approaches for both thermal conductivity problem and linear elasticity problem. We focus on classical bounds, Mori-Tanaka model and Self-consistent model for the mean field methods. In the full field method part, we introduce the notion of Representative Volume Element (RVE) and recall the basic principle of effective properties computation of a composite material using the finite element method with Dirichlet, Neumann and periodic boundary conditions. An emphasis is put on the periodic homogenization which is based on a multi-scale approach and asymptotic analysis. At the end of the first chapter, we mention other homogenization methods such as Fast Fourier Transform method and eXtended Finite Element Method.

In chapter 2, we introduce the PFEM based on the use of independent meshes to represent composite materials. The method is presented for linear static thermal or elasticity problems defined as boundary value problems. We describe the construction of a substitution matrix which allows to substitute the degrees of freedom from inclusion mesh into matrix mesh and compute the energy forms involved in the equivalent variational form associated with the considered boundary value problem. In the second part of this chapter, we show some numerical experiments with two-dimensional inclusion geometries, such as disk and square.

In chapter 3, we present the extension of PFEM to homogenization tech-

nique on a RVE with Dirichlet, Neumann and periodic boundary condition. Numerical experiments with three-dimensional elementary inclusion geometries have been presented for one or several inclusion cases. We perform convergence studies in terms of mesh resolution and parametric studies in terms of volume fraction in order to compare the effective properties computed by PFEM with reference solutions to discuss the performance of the PFEM for composite materials.

Chapter 1

Homogenization

Contents

1.1 Principle of homogenization

The main objective of homogenization is to calculate the effective properties of a composite material from knowledge of the topology of its constituents. This allows one to replace the composite medium with an equivalent homogeneous medium in the macroscopic level.

Let us consider Ω a domain representing a continuum body of heterogeneous material. Two scales are considered: the macroscopic scale (the continuum media scale) and the microscopic scale (the inclusion scale). The distribution, the

form and the elastic/thermal properties of each inclusions inside the matrix and the matrix itself are supposed known. The aim is to estimate the macroscopic behavior of the heterogeneous medium by determining its effective or homogenized properties. This principle is illustrated in Figure 1.1.

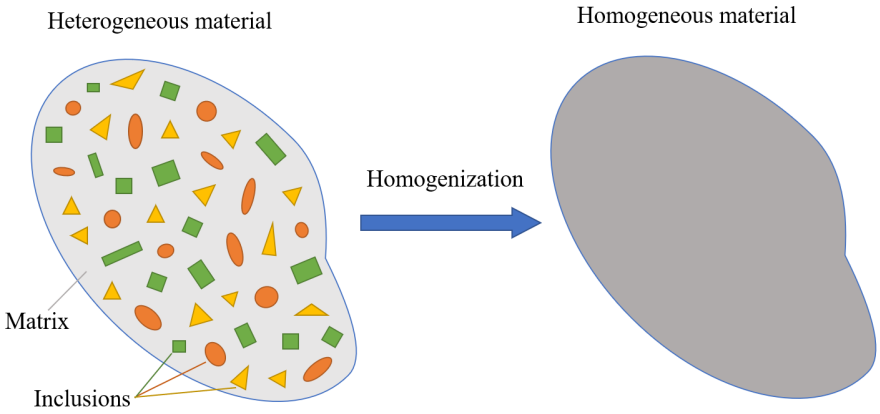

Figure 1.1: Homogenization principle

We are interested in methods who can evaluate homogenized thermal conductivity tensor Λ^{hom} and the homogenized elastic tensor $\mathbb{C}^{hom}$. We can distinguish two kinds of homogenization method : the mean field methods [11, 107] and the full field methods [83]. The mean field methods are used with an incomplete knowledge of the composite: only the volume fraction and the specific geometry of the inclusions are known. These methods allow to estimate the effective behavior of the microstructure with an analytical approach. The full field methods require a complete knowledge of the microstructure: properties of materials, geometry of inclusions and their distribution. When the entire microstructure is identified, the stress/strain tensors or the heat flux/temperature can then be calculated at any point in the microstructure via Finite Element Methods (FEM) or Fast Fourier Transform (FFT) by a numerical approach.

1.2 Mean field methods

The mean field methods are analytic or semi-analytic methods, such as the Mori-Tanaka method [76] or the self consistent method [47]. As they are based on the study of the Eschelby's tensor, see [26], they are usually restricted to spherical and ellipsoidal inclusions and a low volume fraction of inclusions, see [8, 48].

1.2.1 The classic bounds

Rule of mixtures

For a composite material made up of matrix and continuous fiber inclusions, a general rule of mixtures can be used to predict the effective properties by providing analytical upper and lower bound for elasticity and thermal conductivity.

In the case of elasticity, the rule of mixture states that the effective property in the direction parallel to the fibers is:

$$\mathbb{C}^{hom} = \rho_0 \mathbb{C}_0 + \rho_1 \mathbb{C}_1 \tag{1.1}$$

where $\mathbb{C}^{hom}$, $\mathbb{C}_0$ and $\mathbb{C}_1$ denote the elastic tensor of the homogenized material, the matrix and the inclusion respectively, so as the volume fraction ρ. This is known as the upper bound.

The inverse rule of mixture states that the effective property in the direction normal to the fibers is:

$$\mathbb{C}^{hom^{-1}} = \rho_0 \mathbb{C}_0{}^{-1} + \rho_1 \mathbb{C}_1{}^{-1} \tag{1.2}$$

This quantity is called the lower bound.

In the case of thermal conductivity, the rule of mixture states the same ways as in the elasticity, the effective property in the direction parallel to the fibers (the upper bound) writes:

$$\lambda^{hom} = \rho_0 \lambda_0 + \rho_1 \lambda_1 \tag{1.3}$$

where λ^{hom}, λ_{mat} and λ_{inc} denote the thermal conductivity of the homogenized material, the matrix and the inclusion respectively.

The inverse rule of mixture states that the effective property in the direction perpendicular to the fibers (the lower bound) is:

$$\frac{1}{\lambda^{hom}} = \frac{\rho_0}{\lambda_0} + \frac{\rho_1}{\lambda_1} \tag{1.4}$$

Voigt-Reuss bounds

Within the framework of the linear elasticity, the Voigt-Reuss bounds [91,102] only require the knowledge of the volume fractions and the elastic behavior of each phase composing the heterogeneous medium. These bounds are obtained by assuming either the strain tensor $\overline{e}$ or the stress tensor $\overline{\sigma}$ are uniform in the

material. In the first case, we have the Voigt bound (an upper bound) and in the second, the Reuss bound (a lower bound), that read:

$$\mathbb{C}^V = \frac{\overline{\sigma}}{\overline{e}} = \frac{\sum \rho_i \, \overline{\sigma}_i}{\overline{e}} = \frac{\sum \rho_i (\mathbb{C}_i \, \overline{e})}{\overline{e}} = \sum \rho_i \mathbb{C}_i$$

$$\mathbb{C}^R = \{\sum \rho_i {\mathbb{C}_i}^{-1}\}^{-1} \tag{1.5}$$

$$\mathbb{C}^R \leqslant \mathbb{C}^{hom} \leqslant \mathbb{C}^V$$

where $\mathbb{C}^V$ and $\mathbb{C}^R$ denote the strain tensor of the Voigt bound and Reuss bound respectively, ρ_i the volume fraction of the phase i. Since these are upper and lower bounds, an estimate of the effective value is sometimes taken as the average of the two, known as the Voigt-Reuss-Hill average:

$$\mathbb{C}^{VRH} = \frac{\mathbb{C}^R + \mathbb{C}^V}{2} \tag{1.6}$$

For a two-phase isotropic medium (the volume fraction of the matrix noted as ρ_0 and the volume fraction of the inclusion noted as ρ_1), we obtain the bounds of the bulk modulus k and the shear modulus μ as follows:

$$\begin{aligned} k^V &= \rho_1 k_0 + \rho_1 k_1 \\ \mu^V &= \rho_0 \mu_0 + \rho_1 \mu_1 \\ \frac{1}{k^R} &= \frac{\rho_0}{k_0} + \frac{\rho_1}{k_1} \\ \frac{1}{\mu^R} &= \frac{\rho_0}{\mu_0} + \frac{\rho_1}{\mu_0} \end{aligned} \tag{1.7}$$

In the thermal case, these bounds are known as Wiener bounds [103], which is initially developed to evaluate the effective conductivity for a heterogeneous dielectric medium. Subsequently, Wiener bounds are adapted to the thermal conductivity by Springer [98].

The upper Weiner bound is based on a serial layer model and the lower Weiner bound is based on a parallel layer model. For a two-phase medium (the volume fraction noted as ρ_0 and ρ_1 for respectively the matrix and the inclusion, the thermal conductivity noted as λ_0 and λ_1 respectively for the matrix and the inclusion, hence the bounds write:

$$\begin{aligned} \lambda_{hom}^{W+} &= \rho_0 \lambda_0 + \rho_1 \lambda_1 \\ \frac{1}{\lambda_{hom}^{W-}} &= \frac{\rho_0}{\lambda_0} + \frac{\rho_1}{\lambda_1} \end{aligned} \tag{1.8}$$

Hashin-Shtrikman bounds

Compared to the the Voigt-Reuss bounds, the Hashin-Shtrikman bounds [40, 42] are narrower and defined in a macroscopically isotropic two-phase material medium. The homogenized behavior is defined by the bulk modulus k^{hom} and the shear modulus μ^{hom} with the assumption $k_1 > k_0$ and $\mu_1 > \mu_0$:

$$k^{HS-} \leq k^{hom} \leq k^{HS+}$$

$$\text{with} \quad \begin{cases} k^{HS-} = k_0 + \dfrac{\rho_1}{\dfrac{1}{k_1 - k_0} + \dfrac{3\rho_0}{3k_0 + 4\mu_0}} \\ k^{HS+} = k_1 + \dfrac{\rho_0}{\dfrac{1}{k_0 - k_1} + \dfrac{3\rho_1}{3k_1 + 4\mu_1}} \end{cases} \tag{1.9}$$

$$\mu^{HS-} \leq \mu^{hom} \leq \mu^{HS+}$$

$$\text{with} \quad \begin{cases} \mu^{HS-} = \mu_0 + \dfrac{\rho_1}{\dfrac{1}{\mu_1 - \mu_0} + \dfrac{6\rho_0(k_0 + 2\mu_0)}{5\mu_0(3k_0 + 4\mu_0}} \\ \mu^{HS+} = \mu_1 + \dfrac{\rho_0}{\dfrac{1}{\mu_0 - \mu_1} + \dfrac{6\rho_1(k_1 + 2\mu_1)}{5\mu_1(3k_1 + 4\mu_1)}} \end{cases} \tag{1.10}$$

where ρ_0 and ρ_1 denote respectively the volume fraction of the matrix and the inclusion. Microstructures such as the assembly of the Hashin spheres [40] make it possible to calculate the bulk modulus bound and the shear modulus bound.

From the Hashin-Shtrikman model, the thermal conductivity bounds are developed in several lectures [10, 17, 71, 89, 104], by assuming $\lambda_1 > \lambda_0$, we have:

$$\lambda_{hom}^{HS-} = \lambda_0 \left(1 + \frac{3\rho_1(\lambda_1 - \lambda_0)}{3\lambda_0 + \rho_0(\lambda_1 - \lambda_0)}\right) \tag{1.11}$$

$$\lambda_{hom}^{HS+} = \lambda_1 \left(1 + \frac{3\rho_0(\lambda_0 - \lambda_1)}{3\lambda_1 + \rho_1(\lambda_0 - \lambda_1)}\right) \tag{1.12}$$

1.2.2 Mori-Tanaka method

The Mori-Tanaka model [8, 76] is defined for a heterogeneous medium of reinforced matrix type, which is consisted of isotropically distributed inclusions. The inclusions are treated as isolated inclusions in an infinite matrix. We assume that the interface bond between inclusions and their surrounding matrix is perfect.

To determine the elastic properties, we consider a macroscopic material point at $\mathbf{x}$ position in a Cartesian frame. In the case of linear elasticity, the

macroscopic stress tensor $\overline{T}$ and the macroscopic strain tensor $\overline{E}$ are related with the help of a homogenized stiffness tensor (also called effective stiffness tensor) $\mathbb{C}^{hom}$:

$$\langle \overline{T} \rangle_V = \mathbb{C}^{hom} \langle \overline{E} \rangle_V \tag{1.13}$$

with the averaging operator over volume V, $\left(\langle \bullet \rangle_V = \frac{1}{|V|} \int_V \bullet dy \right)$.

Let $\overline{e}$ be the microscopic strain within the volume V. The local mechanical behavior of each inclusion is related to the macroscopic behavior via the strain concentration tensor $\mathbb{A}$ according to:

$$\overline{e}(\mathbf{x}) = \mathbb{A}(\mathbf{x}) \overline{E} \tag{1.14}$$

In the following, we use $\mathbb{A}$ to describe the volume average of $\mathbb{A}(\mathbf{x})$ over volume V, $\mathbb{A} = \langle \mathbb{A}(\mathbf{x}) \rangle_V$. Proposed by Hill [46, 47], for two phases composite, the homogenized stiffness tensor is given by:

$$\mathbb{C}^{hom} = \langle \mathbb{C}\mathbb{A} \rangle_V \tag{1.15}$$

If the heterogeneous medium is a composite made of matrix (index 0) reinforced by several inclusions (index i ranging from 1 to n), the Mori-Tanaka strain concentration tensor for inclusion i of volume V_i, $\mathbb{A}_i^{MT} = \langle \mathbb{A}^{MT} \rangle_{V_i}$ can be calculated by:

$$\mathbb{A}_i^{MT} = \mathbb{T}_i^{MT} \left(\sum_{j=0}^{n} \rho_j \mathbb{T}_j^{MT} \right)^{-1} \tag{1.16}$$

with:

$$\mathbb{T}_i^{MT} = \left[\mathbb{I} + \mathbb{S}_i^E (\mathbb{C}_0)^{-1} (\mathbb{C}_i - \mathbb{C}_0) \right]^{-1} \tag{1.17}$$

where $\mathbb{S}_i^E$ designates the Eshelby tensor corresponding to the i^{th} inclusion (the expression of the Eshelby tensor is given in Appendix C), $\mathbb{I}$ is the identity matrix, $\mathbb{C}_0$ the stiffness tensor of the matrix, $\mathbb{C}_i$ the stiffness tensor of the inclusion i, and $\rho_i = V_i/V$ denotes the volume fraction of the inclusion i with respect to the total volume V of the RVE, which is subjected to the restriction $\sum_{i=0}^{n} \rho_i = 1$ and $\sum_{i=0}^{n} \rho_i \mathbb{A}_i = \mathbb{I}$.

According to (1.15), the expression of the homogenized stiffness tensor $\mathbb{C}^{hom}$ is given by:

$$\mathbb{C}^h = \sum_{i=0}^{n} \rho_i \mathbb{C}_i \mathbb{A}_i = \mathbb{C}_0 + \sum_{i=1}^{n} \rho_i (\mathbb{C}_i - \mathbb{C}_0) \mathbb{A}_i \tag{1.18}$$

Substituting the Mori-Tanaka strain concentration tensor $\mathbb{A}^{MT}$(1.16) in the equation (1.18), we get the expression of the effective tensor $\mathbb{C}^{MT}$:

$$\mathbb{C}^{MT} = \mathbb{C}_0 + \sum_{i=1}^{n} \rho_i (\mathbb{C}_i - \mathbb{C}_0)\mathbb{T}_i^{MT} \left(\sum_{j=0}^{n} \rho_j \mathbb{T}_j^{MT} \right)^{-1} \tag{1.19}$$

Since the stiffness tensors $\mathbb{C}_0$ and $\mathbb{C}_i$ are known , the $\mathbb{C}^{MT}$ formula is explicit. However, this model remains valid for weak volume fractions of inclusions.

In the thermal case, the expression of the homogenized conductivity tensor Λ^{hom} is given by a similar way compared to the elastic case:

$$\Lambda^{hom} = \Lambda_0 + \sum_{i=1}^{n} \rho_i (\Lambda_i - \Lambda_0)\mathbb{A}_i \tag{1.20}$$

where Λ_0 designates the thermal conductivity tensor of the matrix, Λ_i the thermal conductivity tensor of the inclusion i, ρ_i the volume fraction of the inclusion i, and $\mathbb{A}_i$ denotes the heat concentration tensor (analogous to the strain concentration tensor in the elastic case).

1.2.3 Self-consistent method

The self consistent method is based on the solution of an auxiliary inclusion problem where a single spherical or ellipsoidal inclusion is embedded in an infinite matrix [13]. The matrix has the effective properties $\mathbb{C}^{SC}$ of the composite that is felt by each inclusion. The interaction between the inclusions and the homogeneous matrix was given by Eshelby [26].

The self-consistent strain concentration tensor $\mathbb{A}_i^{SC}$ for the inclusion i is determined via the equation:

$$\mathbb{A}_i^{SC} = \left[\mathbb{I} + \mathbb{S}_i^E (\mathbb{C}^{SC})^{-1} (\mathbb{C}_i - \mathbb{C}^{SC}) \right]^{-1} \tag{1.21}$$

Substituting this strain concentration tensor $\mathbb{A}_i^{SC}$ in the equation (1.18), we have the expression of the self-consistent effective stiffness tensor $\mathbb{C}^{SC}$:

$$\mathbb{C}^{SC} = \mathbb{C}_0 + \sum_{i=1}^{n} \rho_i (\mathbb{C}_i - \mathbb{C}_0) \left[\mathbb{I} + \mathbb{S}_i^E (\mathbb{C}^{SC})^{-1} (\mathbb{C}_i - \mathbb{C}^{SC}) \right]^{-1} \tag{1.22}$$

As we can see from equation (1.22), the formula of $\mathbb{C}^{SC}$ is implicit. A common method to find out $\mathbb{C}^{SC}$ is to use an iterative fixed-point method by initializing $\mathbb{C}^{SC}$ through the Voigt-Reuss bound or by the Mori-Tanaka model.

This is a widely used model for polycrystalline and granular media [89].

1.3 Full field methods

Full field methods can consider more general composites than mean field methods, but require the exact knowledge of the geometry. Effective properties can be calculated with the help of various numerical methods such as the finite element method [24] or iterative methods based on Fast Fourier Transform technique [78, 79]. In this section, we distinguish two cases: the determination of effective properties with non-periodic conditions and the periodic homogenization.

1.3.1 Representative Volume Element

First, we introduce the notion of Representative Volume Element (RVE). The concept of RVE is important in the field of numerical modeling of heterogeneous media. The term RVE seems to have been created by Hill [46] and has also been detailed extensively by Hashin and co-workers (reviewed in [41]). The effective properties of composites can be determined not only by numerical simulations with large volume elements of heterogeneous material, but also as mean values of apparent properties of rather small volumes, provided that a sufficient number of realizations is taken into account.

From a statistical point of view, Homogenization problems can be solved by means of numerical techniques on samples of microstructure. And RVE is the smallest sample which is large enough to be stochastically representative of the composite. The notion of RVE is very important, since computations on large volumes are usually prohibitive. And it should be noticed that the RVE is a representative motif of the microstructure of a multi-phase medium. The key point is to understand under which assumptions the representativity of the composite is respected. Several definitions have been given during the last decades among which we can retain the following ideas:

- The RVE must contain enough information on the microstructure and therefore include a sample of heterogeneities such as voids, fibers, inclusions, grains, etc [41, 46];

- According to Kanit et al. [53], the size of RVE must be considered as a function of five parameters: the physical property, the contrast of properties, the volume fractions of components, the wanted relative precision for the estimation of the effective property and the number of realizations of the microstructure associated with the computations;

- By Drugan and Willis [22], the RVE must be the smallest material volume element of the composite for which the usual spatially constant

(overall modulus) macroscopic constitutive representation is a sufficiently ensured model to represent mean constitutive response. The definition is based on a numerical criterion according to the homogenization calculation. This is to verify that the representation of the macroscopic medium in terms of properties or modules is equivalent to that of the expected average response;

- The chosen volume of RVE cannot be taken as small as one may wish, because there exists in general a bias in the estimation of the effective properties. This bias is due to the type of boundary conditions [53];

The evaluation of RVE dimensions is important. It has to respect a compromise between the richness of the collected information and the cost of calculation. Furthermore, in the case of periodic homogenization, we can assume the considered RVE is the period of the composite material. And in that case, we can obtain the homogenized conductivity or elasticity tensor.

1.3.2 Determination of effective properties

In this section, we introduce the notations and elements of the determination of effective properties which can be found in reference papers like [53]. The following studies are presented for thermal conductivity and linear elasticity.

The approach of effective properties determination presented in this section is different than the periodic homogenization which is based on a multi-scale approach and asymptotic analysis. It is developed in accordance with two different type of boundary conditions: the Dirichlet condition and the Neumann condition.

Thermal conductivity

We briefly summarize here the approach to compute the effective properties for composite material with finite elements methods. Let us consider the domain Ω representing the space occupied by a composite material. To fix the ideas, let Ω be a subset of the space $\mathbb{R}^D$ (with $D = 2, 3$ the dimension of the domain). Let $\partial\Omega$ be the boundary of the domain Ω. For the sake of simplicity, we set $|\Omega| = 1$. The approach presented below is in three dimensional case, while the two dimensional case is the same.

To calculate effective properties using a Finite Element Method, one can solve specific boundary value problems. With the help of the solutions obtained, we are able to determine effective properties. Let us present here the principle of calculating effective properties in the case of steady state thermal conductivity problems.

For the temperature u, we associate the thermal flux defined as

$$\mathbf{q} = \Lambda \nabla u, \tag{1.23}$$

where Λ is the second order thermal conductivity tensor, ∇u is the temperature gradient; (1.23) defines the thermal properties of the material. we remind that for a composite material, the second order thermal conductivity tensor Λ is not constant every where over Ω but can be piecewise constant.

The effective properties are represented by a constant second order tensor Λ^{eff} satisfying the relation

$$\int_\Omega \mathbf{q} = \Lambda^{eff} \int_\Omega \nabla u, \tag{1.24}$$

for some specific cases.

The effective properties tensor Λ^{eff} will have different expressions depending on the imposed boundary conditions. Two types of boundary conditions are considered : Pure Dirichlet boundary conditions and Pure Neumann boundary conditions. For thermal conductivity problems, the boundary conditions are originally called Uniform Heat Flux and Uniform Gradient of Temperature, see [53]. For linear elasticity problems, the boundary conditions are called Kinematic Uniform Boundary Conditions (KUBC) and Static Uniform Boundary Condition (SUBC). For the sake of clarity, we chose to use the terminology of elasticity problems for both cases.

- Kinematic Uniform Boundary Conditions (KUBC)

In thermal case, a uniform gradient of temperature is imposed at the boundary, the pure Dirichlet boundary value problem writes:

$$\begin{cases} div\ \mathbf{q} = 0 & \text{in } \Omega \\ u = \mathbf{g}.\mathbf{x} & \text{on } \partial\Omega \end{cases} \tag{1.25}$$

with $\mathbf{g}$ a constant vector independent of $\mathbf{x}$, ' . ' symbolize the dot product of two vectors :

$$\mathbf{g}.\mathbf{x} = \sum_{i=1}^{3} g_i\, x_i$$

The problem (1.25) is well-posed and implies that:

$$\int_\Omega \nabla u = \mathbf{g} \tag{1.26}$$

See Appendix A.1 for the proof of the equation (1.26). With the spatial average operator $\langle ... \rangle$ and $|\Omega| = 1$, we have:

$$\begin{aligned} \langle \nabla u \rangle &= \frac{1}{|\Omega|} \int_\Omega \nabla u \\ &= \mathbf{g} \end{aligned}$$

The macroscopic flux vector $\mathbf{Q}$ is defined by the spatial average:

$$\begin{aligned}\mathbf{Q} &= \langle \mathbf{q} \rangle \\ &= \int_\Omega \Lambda \nabla u \\ &= \Lambda^{kubc} \langle \nabla u \rangle\end{aligned}$$

so that we have:

$$\Lambda^{kubc} \mathbf{g} = \int_\Omega \Lambda \nabla u \tag{1.27}$$

Solving all three problems with $\mathbf{g} = [1,0,0]$, $[0,1,0]$ and $[0,0,1]$ by using finite element method, we get the effective conductivity tensor Λ^{kubc} column by column.

- Static Uniform Boundary Condition (SUBC)

A uniform heat flux is imposed at the boundary as Neumann condition, which reads:

$$\begin{cases} div\ \mathbf{q} = 0 & \text{in } \Omega \\ \mathbf{q}.\mathbf{n} = \mathbf{Q}.\mathbf{n} & \text{on } \partial\Omega \end{cases} \tag{1.28}$$

In Appendix A.2, we proof that:

$$\mathbf{Q} = \int_\Omega \mathbf{q}$$

which implies:

$$\begin{aligned}\mathbf{Q} &= \langle \mathbf{q} \rangle \\ &= \Lambda^{subc} \langle \nabla u \rangle\end{aligned}$$

so that we have:

$$\mathbf{Q} = \Lambda^{subc} \int_\Omega \nabla u \tag{1.29}$$

By imposing $\mathbf{Q} = [1,0,0]$, then $\mathbf{Q} = [0,1,0]$ and $\mathbf{Q} = [0,0,1]$, we obtain $(\Lambda^{subc})^{-1}$ column by column.

Linear elasticity

For steady state linear elasticity problems, we are able to determine effective properties by solving a specific boundary value problem using a Finite Element Method.

In the case of linear elasticity, the stress tensor $\overline{\sigma}$ and the strain tensor $\overline{e}$ are related by Hooke's law:

$$\overline{\sigma} = \mathbb{C}\,\overline{e} \tag{1.30}$$

where $\mathbb{C}$ is a fourth order stiffness tensor (the expression of $\mathbb{C}$ is given in appendix B); (1.30) defines the elastic properties of the material. $\mathbb{C}$ is a piecewise constant in Ω of a composite material.

The effective properties are represented by a constant fourth order tensor $\mathbb{C}^{eff}$ satisfying the relation:

$$\int_\Omega \overline{\sigma} = \mathbb{C}^{eff} \int_\Omega \overline{e} \tag{1.31}$$

for some specific cases.

The effective properties tensor $\mathbb{C}^{eff}$ will have different expressions depending on the imposed boundary conditions. Two types of boundary conditions are considered : Pure Dirichlet boundary conditions, Pure Neumann boundary conditions.

- Kinematic Uniform Boundary Conditions (KUBC)

For the kinematic uniform boundary conditions, we impose a displacement at point $\mathbf{x}$ belonging to the boundary $\partial\Omega$, the pure Dirichlet boundary value problem writes:

$$\begin{cases} div\ \overline{\sigma} = 0 & \text{in } \Omega \\ \mathbf{u} = \overline{E}\,\mathbf{x} & \text{on } \partial\Omega \end{cases} \tag{1.32}$$

with $\overline{E}$ a symmetrical tensor which does not depend on $\mathbf{x}$. The spatial average of strain gives:

$$\begin{aligned} \langle \overline{e} \rangle &= \int_\Omega e_{ij}(\mathbf{u}) \\ &= \frac{1}{2}\left(\int_\Omega u_{i,j} + \int_\Omega u_{j,i} \right) \end{aligned}$$

In Appendix A.3, we demonstrate in detail that:

$$\langle \overline{e} \rangle = \overline{E}$$

The macroscopic stress tensor is defined by the spatial average:

$$\begin{aligned} \overline{\Sigma} &= \langle \overline{\sigma} \rangle \\ &= \mathbb{C}^{kubc} \langle \overline{e} \rangle \\ &= \mathbb{C}^{kubc}\, \overline{E} \end{aligned}$$

where $\mathbb{C}^{kubc}$ denotes the effective elasticity tensor calculated with KUBC method, and then we have:

$$\langle \overline{\sigma} \rangle = \int_\Omega \mathbb{C}\, \overline{e}(\mathbf{u})$$

which leads to:

$$\mathbb{C}^{kubc}\,\overline{E} = \int_{\Omega} \mathbb{C}\,\overline{e}(\mathbf{u}) \tag{1.33}$$

Solving the six problems in Voigt notation with $\overline{E} = [1,0,0,0,0,0]$, $[0,1,0,0,0,0]$, $[0,0,1,0,0,0]$, $[0,0,0,1,0,0]$, $[0,0,0,0,1,0]$, $[0,0,0,0,0,1]$ by using finite element method, we obtain $\mathbb{C}^{kubc}$ column by column.

- Static Uniform Boundary Conditions (SUBC)

With the static uniform boundary condition (Neumann condition), we prescribe a traction vector at the boundary, reads:

$$\begin{cases} div\ \overline{\sigma} = 0 & \text{in } \Omega \\ \overline{\sigma}\,\mathbf{n} = \overline{\Sigma}\,\mathbf{n} & \text{on } \partial\Omega \end{cases} \tag{1.34}$$

where $\mathbf{n}$ denotes the outgoing normal unit vector to $\partial\Omega$ at $\mathbf{x}$, $\overline{\Sigma}$ is a symmetrical second-rank tensor independent of $\mathbf{x}$.

In Appendix A.4, we proof that:

$$\overline{\Sigma} = \langle \overline{\sigma} \rangle$$

We introduce $\mathbb{C}^{subc}$, the effective elastic tensor calculated by SUBC method:

$$\begin{aligned} \langle \overline{\sigma} \rangle &= \int_{\Omega} \overline{\sigma} \\ &= \int_{\Omega} \mathbb{C}\,\overline{e}(\mathbf{u}) \\ &= \mathbb{C}^{subc} \int_{\Omega} \overline{e}(\mathbf{u}) \end{aligned}$$

Finally, we have:

$$\overline{\Sigma} = \mathbb{C}^{subc} \int_{\Omega} \overline{e}(\mathbf{u}) \tag{1.35}$$

By solving the six problems in Voigt notation with $\overline{\Sigma} = [1,0,0,0,0,0]$, $[0,1,0,0,0,0]$, $[0,0,1,0,0,0]$, $[0,0,0,1,0,0]$, $[0,0,0,0,1,0]$, $[0,0,0,0,0,1]$, we obtain $(\mathbb{C}^{subc})^{-1}$ column by column.

1.3.3 Periodic homogenization

In this section, we recall the periodic homogenization theory and its numerical implementation with the finite element method [24].

Periodic material is a material with cavities or inclusions periodically arranged in one, two or three directions of space, as shown in Figure 1.2.

The material period can be identified as the RVE. In other words, the whole microstructure of the periodic composite is generated by periodic repetition

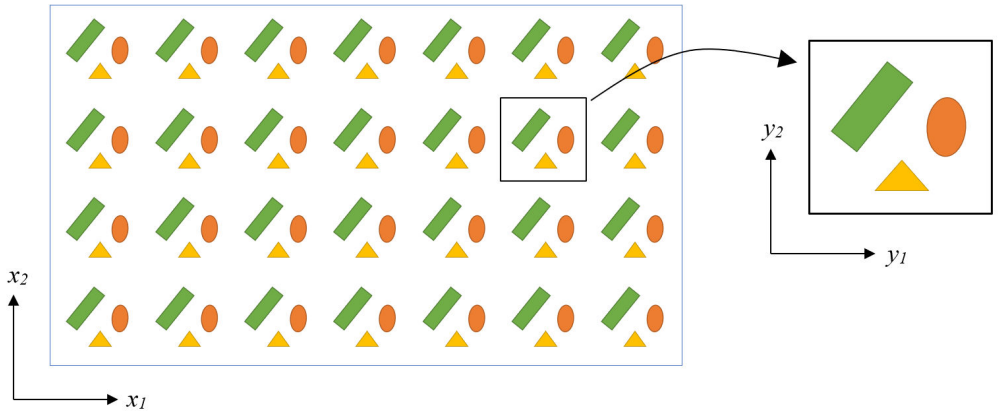

Figure 1.2: Periodic materials

of the RVE. And the overall property of the composite is specified from the geometrical and material properties of RVE.

We present the periodic homogenization theory in the case of thermal properties and elastic properties. The multi-scale modelling based on asymptotic expansion is described by Bensoussan et al. [7] and Sanchez-Palencia [95].

Let us consider a εP periodic material, P thus constitutes the Representative Volume Element (RVE), ε denotes the characteristic length of the RVE. To fix the ideas the RVE P is the unit cube $[0,1]^3$.

The multiscale modeling consider macrocospic and local space variables. To the macroscopic space variables $\mathbf{x} \in \mathbb{R}^3$, we associate the local (microscopic) space variables:

$$\mathbf{y} = \frac{1}{\varepsilon}\mathbf{x} \in P$$

The divergence and gradient differential operators are respectively denoted as:

$$div = div_x + \frac{1}{\varepsilon} div_y$$

$$\nabla = \nabla_x + \frac{1}{\varepsilon}\nabla_y$$

where div_x and ∇_x (resp. div_y and ∇_y) denote the divergence and the gradient differential operator with respect to the macroscopic variables $\mathbf{x}$ (resp. the local variables $\mathbf{y}$).

Thermal conductivity problem

With a periodic heterogeneous media, the thermal constitutive law writes:

$$\mathbf{q} = \Lambda \nabla u \tag{1.36}$$

where u denotes the temperature and $\mathbf{q}$ the heat flow, the conductivity tensor Λ is εP periodic.

Under the action of external heat source f, the thermal equilibrium writes:

$$div\ \mathbf{q} + f = 0 \tag{1.37}$$

We set the asymptotic expansion:

$$u = u^0(\mathbf{x}) + \varepsilon u^1(\mathbf{y}) + \dots \tag{1.38}$$
$$\nabla u = \mathbf{e}(u) = \mathbf{e}^0(u) + \varepsilon\, \mathbf{e}^1(u) + \dots \tag{1.39}$$
$$\mathbf{q} = \mathbf{q}^0 + \varepsilon \mathbf{q}^1 + \dots \tag{1.40}$$
$$\mathbf{q} = \Lambda(\, \mathbf{e}^0(u) + \varepsilon\, \mathbf{e}^1(u) + \dots\,) \tag{1.41}$$

As we develop:

$$\begin{aligned}\nabla u &= (\nabla_x + \frac{1}{\varepsilon}\nabla_y)(u^0 + \varepsilon u^1 + \varepsilon^2 u^2 + \dots) \\ &= \frac{1}{\varepsilon}\nabla_y u^0 + (\nabla_x u^0 + \nabla_y u^1) + \varepsilon(\nabla_x u^1 + \nabla_y u^2) + \dots\end{aligned}$$

we obtain by identification:

$$\begin{aligned}\mathbf{e}^0(u) &= \nabla_x u^0 + \nabla_y u^1 \\ \mathbf{e}^1(u) &= \nabla_x u^1 + \nabla_y u^2 \\ \mathbf{q}^0 &= \Lambda(\nabla_x u^0 + \nabla_y u^1)\end{aligned}$$

Writing asymptotic expansion of the heat flow $\mathbf{q}$ in the equilibrium equation (1.37) gives:

$$(div_x + \frac{1}{\varepsilon} div_y)(\Lambda \nabla u) + f = 0$$

$$(div_x + \frac{1}{\varepsilon} div_y)(\Lambda(\frac{1}{\varepsilon}\nabla_y u^0 + \mathbf{e}^0(u) + \varepsilon\, \mathbf{e}^1(u) + ...)) + f = 0$$

$$\begin{aligned}\frac{1}{\varepsilon^2} div_y(\Lambda \nabla_y u^0) + \frac{1}{\varepsilon} div_x(\Lambda \nabla_y u^0) + \frac{1}{\varepsilon} div_y(\Lambda\, \mathbf{e}^0(u)) \\ + div_x(\Lambda\, \mathbf{e}^0(u)) + div_y(\Lambda\, \mathbf{e}^1(u) + f = 0\end{aligned}$$

By identification according to the order of ε, we obtain:

$$(\varepsilon^{-2}): \quad div_y(\Lambda \nabla_y u^0) = 0 \tag{1.42}$$
$$(\varepsilon^{-1}): \quad div_x(\Lambda \nabla_y u^0) + div_y(\Lambda\, \mathbf{e}^0(u)) = 0 \tag{1.43}$$
$$(\varepsilon^{0}) \ : \quad div_x(\Lambda\, \mathbf{e}^0(u)) + div_y(\Lambda\, \mathbf{e}^1(u)) + f = 0 \tag{1.44}$$

As it follows that u^0 depends only on $\mathbf{x}$ (1.42), the simplification of the equation (1.43) gives a local equation:

$$div_y(\mathbf{q}^0) = 0 \quad \text{in } P \tag{1.45}$$

Applying the average operator $\left(\langle\bullet\rangle_P = \frac{1}{|P|}\int_P \bullet dy\right)$ to the equation (1.44) gives:

$$div_x\langle\Lambda\,\mathbf{e}^0(u)\rangle_P + \ div_y\langle\Lambda\,\mathbf{e}^1(u)\rangle_P + \langle f\rangle_P \ = 0 \tag{1.46}$$

As u^1 must be P-periodic, the second term of the equation (1.46) vanishes by using the divergence theorem and the anti-symmetric heat flux. Thus, we obtain a macroscopic equation:

$$div_x\langle\mathbf{q}^0\rangle_P + \langle f\rangle_P \ = 0 \tag{1.47}$$

In order to obtain the homogenized coefficients, we write the local equation (1.45) in a weak or variational form :

$$\int_P \mathbf{q}^0.\nabla_y(u^*) = 0 \quad \forall u^* \in H^1_{periodic}(P) \tag{1.48}$$

Where $H^1_{periodic}(P)$ is the P-periodic Sobolev space H^1 .
Let $\mathbf{E}^0 = \nabla_x u^0$, then

$$\mathbf{q}^0 = \Lambda(\mathbf{E}^0 + \nabla_y u^1)$$

Averaging $\mathbf{q}^0$ on the RVE P, we then have :

$$\begin{aligned}\langle\mathbf{q}^0\rangle_P &= \frac{1}{|P|}\int_P \Lambda(\mathbf{E}^0 + \nabla_y u^1)\\ &= \Lambda^{periodic}\nabla u^0\end{aligned} \tag{1.49}$$

$\Lambda^{periodic}$ denotes the homogenized conductivity tensor.
Furthermore, with (1.48), $\forall \mathbf{E}^* \in \mathbb{R}^3$ and $\forall u^* \in H^1_{periodic}(P)$:

$$\begin{aligned}\frac{1}{|P|}\int_P \mathbf{q}^0.(\mathbf{E}^* + \nabla_y u^*) &= \frac{1}{|P|}\int_P \mathbf{q}^0.\mathbf{E}^* + \frac{1}{|P|}\int_P \mathbf{q}^0.\nabla_y u^*\\ &= \langle\mathbf{q}^0\rangle_P.\mathbf{E}^*\\ &= (\Lambda^{periodic}\nabla u^0).\mathbf{E}^*\end{aligned}$$

In other words, we obtain the variational problems:

$$\begin{cases}\forall u^* \in H^1_{periodic}(P), \forall \mathbf{E}^* \in \mathbb{R}^3,\\ \dfrac{1}{|P|}\displaystyle\int_P \Lambda(\mathbf{E}^0 + \nabla_y u^1).(\mathbf{E}^* + \nabla_y u^*) = (\Lambda^{periodic}\mathbf{E}^0).\mathbf{E}^*\end{cases} \tag{1.50}$$

Solving the three problems (1.50) as $\Lambda^{periodic}\mathbf{E}^0$ span $\mathbb{R}^3$, gives the homogenized conductivity tensor $\Lambda^{periodic}$. The variational problems (1.50) are well-posed [95] and their solutions can be approximated by the finite element method [24].

Linear elasticity problem

With the external forces $\mathbf{f}$, the elasticity problem writes:

$$\begin{cases} div(\overline{\sigma}^{\varepsilon}) + \mathbf{f} = \mathbf{0} & \text{in } P \\ \overline{\sigma}^{\varepsilon} = \mathbb{C}^{\varepsilon}\, \overline{e}(\mathbf{u}^{\varepsilon}) & \text{in } P \\ \text{Boundary conditions} & \text{on } \partial P \end{cases} \tag{1.51}$$

$$\text{with } \mathbb{C}^{\varepsilon}(\mathbf{x}) = \mathbb{C}\left(\frac{\mathbf{x}}{\varepsilon}\right) = \mathbb{C}(\mathbf{y}) \text{ for all } \mathbf{x} \text{ in } P,\ \mathbf{y} \text{ in } \varepsilon P$$

We set the asymptotic expansion:

$$\mathbf{u}^{\varepsilon}(\mathbf{x}) = \mathbf{u}^0(\mathbf{x}) + \varepsilon \mathbf{u}^1(\mathbf{x}, \mathbf{y}) + \varepsilon^2 \mathbf{u}^2(\mathbf{x}, \mathbf{y}) + o(\varepsilon^2) \tag{1.52}$$

$$\overline{e}(\mathbf{u}^{\varepsilon}) = \overline{e}^0(\mathbf{x}, \mathbf{y}) + \varepsilon \overline{e}^1(\mathbf{x}, \mathbf{y}) + o(\varepsilon) \tag{1.53}$$

$$\overline{\sigma}(\mathbf{u}^{\varepsilon}) = \overline{\sigma}^0(\mathbf{x}, \mathbf{y}) + \varepsilon \overline{\sigma}^1(\mathbf{x}, \mathbf{y}) + o(\varepsilon) \tag{1.54}$$

where $\mathbf{u}^1$ and $\mathbf{u}^2$ are P-periodic on $\mathbf{y}$.

The strain tensor $\overline{e}$ expands as follow:

$$\overline{e}(\mathbf{u}^{\varepsilon}) = \overline{e}_x(\mathbf{u}^{\varepsilon}) + \frac{1}{\varepsilon}\overline{e}_y(\mathbf{u}^{\varepsilon}) \tag{1.55}$$

$$e_{ij}(\mathbf{u}^{\varepsilon}) = e_{ijx}(\mathbf{u}^{\varepsilon}) + \frac{1}{\varepsilon} e_{ijy}(\mathbf{u}^{\varepsilon}) \tag{1.56}$$

with:

$$\begin{cases} e_{ijx} = \dfrac{1}{2}\left(\dfrac{\partial u_i}{\partial x_j} + \dfrac{\partial u_j}{\partial x_i}\right) \\ e_{ijy} = \dfrac{1}{2}\left(\dfrac{\partial u_i}{\partial y_j} + \dfrac{\partial u_j}{\partial y_i}\right) \end{cases} \tag{1.57}$$

Replacing the expansion of $\mathbf{u}^{\varepsilon}$ (1.52) in the expression of $\overline{e}$ (1.55) (or (1.56) with index notation), we obtain the term of degree 0 on ε by identification:

$$\overline{e}^0(\mathbf{x}, \mathbf{y}) = \overline{e}_x(\mathbf{u}^0) + \overline{e}_y(\mathbf{u}^1) \tag{1.58}$$

$$\overline{\sigma}^0(\mathbf{x}, \mathbf{y}) = \mathbb{C}(\mathbf{y})\, \overline{e}^0(\mathbf{x}, \mathbf{y}) = \mathbb{C}(\mathbf{y})\left(\overline{e}_x(\mathbf{u}^0) + \overline{e}_y(\mathbf{u}^1)\right) \tag{1.59}$$

On the other hand, replacing the expression of $\overline{\sigma}$ (1.54) in the local problem (1.51) and identifying in the degree order of ε, we obtain the equations:

$$(\varepsilon^{-1}): \quad div_y \overline{\sigma}^0 = 0 \tag{1.60}$$

$$(\varepsilon^0) \quad : \quad div_x \overline{\sigma}^0 + div_y \overline{\sigma}^1 + \mathbf{f} = 0 \tag{1.61}$$

Applying the average operator to the equation (1.61), and using the divergence theorem with the periodicity of $\overline{\sigma}^1$ in relation to $\mathbf{y}$, we obtain the macroscopic equation:

$$div_x\langle\overline{\sigma}^0\rangle_P + \langle\mathbf{f}\rangle_P = 0 \tag{1.62}$$

To obtain the effective coefficients, we use the microscopic equation (1.60), in which we replace the expression of $\overline{\sigma}^0$ in (1.59) by defining the macroscopic deformation: $\overline{E} \overset{\text{def}}{=} \overline{e}_x(\mathbf{u}^0)$

$$\overline{\sigma}^0 = \mathbb{C}(\mathbf{y})\left(\overline{E} + \overline{e}_y(\mathbf{u}^1)\right) \tag{1.63}$$

$$div_y\left[\mathbb{C}(\mathbf{y})\left(\overline{E} + \overline{e}_y(\mathbf{u}^1)\right)\right] = 0 \tag{1.64}$$

We assume that $\mathbf{u}^1$ is depending on $\mathbf{x}$ and $\mathbf{y}$:

$$\mathbf{u}^1(\mathbf{x},\mathbf{y}) = \overline{e}_x(\mathbf{u}^0(\mathbf{x}))\mathbf{w}(\mathbf{y}) \tag{1.65}$$

with the functions $\mathbf{w}$ depend on $\mathbf{y}$ and P-periodic.

Once the $\mathbf{w}$ functions are known, we deduce in Appendix A.5, the expression of the homogenized coefficients:

$$\mathbb{C}^{periodic} = \underbrace{\frac{1}{|P|}\int_P \mathbb{C}(\mathbf{y})}_{\text{average coefficient}} + \underbrace{\frac{1}{|P|}\int_P \mathbb{C}(\mathbf{y})\,\overline{e}_y(\mathbf{w}(\mathbf{y}))}_{\text{corrective term}} \tag{1.66}$$

Using weak formulation technique and periodicity assumption, the expression of the homogenized tensor $\mathbb{C}^{periodic}$ is thus determined. However, the expression obtained in (1.66) gives an expression of $\mathbb{C}^{periodic}$ as a function of $\mathbf{w}$ which have to be determined beforehand. When the problem is unidirectional, it is possible to determine $\mathbb{C}^{periodic}$ analytically. Therefore in three dimensional problem or complex microstructure, we need other techniques to solve the problem.

In order to estimate the coefficients $\mathbb{C}^{periodic}$ without calculating $\mathbf{w}^{pq}$, we use the method proposed by Débordès [24]. We reconsider the weak formulation of the microscopic equation (1.64). By using an integration by parts and the periodicity on P, it writes:

$$\begin{cases} \forall \mathbf{u}^* \in H^1_{periodic}(P), \\ \displaystyle\int_P C_{ijkl}(E_{kl} + e_{kly}(\mathbf{u}^1))(e_{ijy}(\mathbf{u}^*)) = 0 \end{cases}$$

so we have:

$$\begin{cases} \forall (\overline{E}^*, \mathbf{u}^*) \in \mathbb{R}^{3\times3}_{sym} \times H^1_{periodic}(P), \\ \displaystyle\int_P C_{ijkl}(E_{kl} + e_{kly}(\mathbf{u}^1))(E^*_{ij} + e_{ijy}(\mathbf{u}^*) - E^*_{ij}) = 0 \end{cases}$$

Rewriting the previous equality, we obtain:

$$\int_P C_{ijkl}(E_{kl} + e_{kly}(\mathbf{u}^1))(E^*_{ij} + e_{ijy}(\mathbf{u}^*)) = \int_P C_{ijkl}(E_{kl} + e_{kly}(\mathbf{u}^1))E^*_{ij} \quad (1.67)$$

The second part of the equation (1.67) can be rewrited by using the independence of $\overline{E}^*$ versus y:

$$\begin{aligned}\int_P C_{ijkl}(E_{kl} + e_{kly}(\mathbf{u}^1))(E^*_{ij}) &= \left(\int_P C_{ijkl}(E_{kl} + e_{kly}(\mathbf{u}^1))\right) E^*_{ij} \\ &= \left(\int_P \sigma^0_{ij}\right) E^*_{ij} \\ &= |P|\langle\overline{\sigma}^0\rangle_P : \overline{E}^* \\ &= |P|\ (\mathbb{C}^{periodic}\overline{E}) : \overline{E}^* \end{aligned} \quad (1.68)$$

where ' : ' symbolize the double dot product of two matrices :

$$\overline{A} : \overline{B} = \sum_{i=1}^{3}\sum_{j=1}^{3} A_{ij}B_{ij}$$

From the equations (1.67) and (1.68), we obtain:

$$\begin{cases} \forall(\overline{E}^*, \mathbf{u}^*) \in \mathbb{R}^{3\times3}_{sym} \times H^1_{periodic}(P), \\ \dfrac{1}{|P|}\displaystyle\int_P \left[\mathbb{C}(\overline{E} + \overline{e}_y(\mathbf{u}^1))\right] : (\overline{E}^* + \overline{e}_y(\mathbf{u}^*)) = (\mathbb{C}^{periodic}\overline{E}) : \overline{E}^* = \langle\overline{\sigma}^0\rangle_P : \overline{E}^* \end{cases} \quad (1.69)$$

Solving the six problems of (1.69) for $\langle\overline{\sigma}^0\rangle_P$ in $\mathbb{R}^{3\times3}_{sym}$ allow us to obtain $(\mathbb{C}^{periodic})^{-1}$ by using finite element method.

This method is efficient for elementary microstructures but it becomes prohibitive in memory capacity and computation time for complex microstructures with a requirement of very fine mesh.

1.3.4 Fast Fourier transform method and Lippmann-Schwinger equation

This method does not use mesh as in finite elements but a voxelization of the RVE, which is close to the grid approximation mesh methods. In each voxel, we associate a phase with its specific properties. More precisely, the method consists in solving the Lippman-Schwinger equations in the Fourier space. This approach is described in the Moulinec and Suquet's work [78, 79].

Inspired by the asymptotic development, the local problem of elastic deformation is given by:

$$\begin{cases} \overline{\sigma}(\mathbf{x}) = \mathbb{C}_0(\overline{e}(\mathbf{u})) + \overline{\tau}(\mathbf{x}) & \text{in } P \\ div(\overline{\sigma}(\mathbf{x})) = 0 & \text{in } P \\ \mathbf{u} \text{ periodic} \end{cases} \quad (1.70)$$

where $\mathbb{C}_0$ designates the stiffness tensor for the reference material, $\overline{\sigma}$ the stress tensor, $\overline{e}$ the strain tensor, and $\overline{\tau}$ denotes the polarization tensor defined by:

$$\overline{\tau}(\mathbf{x}) = \delta\mathbb{C}(\mathbf{x})\overline{e}(\mathbf{x}) + \mathbb{C}_0\overline{E} \text{ , with } \delta\mathbb{C}(\mathbf{x}) = \mathbb{C}(\mathbf{x}) - \mathbb{C}_0 \tag{1.71}$$

Introducing the periodic Green's function[1] $\mathbb{G}_0$ associated to $\mathbb{C}_0$, we have:

$$\overline{e}(\mathbf{u})(\mathbf{x}) = -\mathbb{G}_0\,\overline{\tau}(\mathbf{x}), \text{ for all } \mathbf{x} \text{ in } P \tag{1.72}$$

In the Fourier space, the equation (1.72) becomes:

$$\begin{cases} \widehat{\overline{e}(\mathbf{u})}(\boldsymbol{\xi}) = -\widehat{\mathbb{G}}_0\widehat{\overline{\tau}}(\boldsymbol{\xi}), \text{ for all } \boldsymbol{\xi} \neq \mathbf{0} \\ \widehat{\overline{e}(\mathbf{u})}(\mathbf{0}) = 0 \\ \mathbf{u} \text{ periodic} \end{cases} \tag{1.73}$$

Using the expression (1.71), the equation (1.72) becomes:

$$\overline{e}(\mathbf{u}(\mathbf{x})) = -\mathbb{G}_0(\delta\,\mathbb{C}(\mathbf{x})\,\overline{e}(\mathbf{u}(\mathbf{x}))) + \overline{E}, \text{ for all } \mathbf{x} \text{ in } P \tag{1.74}$$

Putting (1.74) in the Fourier space, we obtain:

$$\begin{cases} \widehat{\overline{e}(\mathbf{u})}(\boldsymbol{\xi}) = -\widehat{\mathbb{G}}_0(\delta\,\widehat{\mathbb{C}\,\overline{e}(\mathbf{u})})(\boldsymbol{\xi}), \text{ for all } \boldsymbol{\xi} \neq \mathbf{0} \\ \widehat{\overline{e}(\mathbf{u})}(\mathbf{0}) = \overline{E} \\ \mathbf{u} \text{ periodic} \end{cases} \tag{1.75}$$

The equations (1.74) and (1.75) form the periodic equation of Lippmann-Schwinger [56, 80] respectively in the real space and in the Fourier space. The equation (1.75) can be solved iteratively by a fixed point method [68–70, 74, 75, 78–80].

For an isotropic reference material, the stiffness tensor $\mathbb{C}_0$ and the periodic Green's function $\mathbb{G}_0$ is given by Mura [83] in the Fourier space:

$$\begin{aligned} C_{ijkh} &= \lambda^0\delta_{ij}\delta_{kh} + \mu^0(\delta_{ik}\delta_{jh} + \delta_{ih}\delta_{jk}) \\ G_{ijkh}(\boldsymbol{\xi}) &= \frac{1}{4\mu^0|\boldsymbol{\xi}|^2}(\delta_{ki}\boldsymbol{\xi_h}\boldsymbol{\xi_j} + \delta_{hi}\boldsymbol{\xi_k}\boldsymbol{\xi_j} + \delta_{kj}\boldsymbol{\xi_h}\boldsymbol{\xi_i} + \delta_{hj}\boldsymbol{\xi_k}\boldsymbol{\xi_i}) \\ &\quad - \frac{\lambda^0 + \mu^0}{\mu^0(\lambda^0 + 2\mu^0)}\frac{\boldsymbol{\xi_i}\boldsymbol{\xi_j}\boldsymbol{\xi_k}\boldsymbol{\xi_h}}{|\boldsymbol{\xi}|^4} \end{aligned}$$

where λ^0, μ^0 denote the Lamé parameters δ the Kronecker's delta, and $\boldsymbol{\xi}$ is the Fourier space variable.

The contribution of the Fourier space is directly related to the convolution between the Green's operator and the stress tensor. An example of the resolution algorithm is given in [35]. The limitation of this methodology is that it does not work with very strong contrasts. However, it is possible to set up an increased Lagrangian type scheme to study very heterogeneous composites with complex geometry [70].

[1] $\mathbb{C}_0\overline{e}(\mathbb{G}_0)_{im} = \delta_{im}\delta_0(\mathbf{x})$, [83]

1.3.5 Other methods

XFEM method

With the Finite Element Method (FEM), the modeling of a domain containing interfaces requires a mesh conforming with all internal surfaces. This operation is costly for complex three-dimensional geometries, for example in case of the phase evolution [101]. The eXtended Finite Element Method (XFEM) [33,65, 82,100] is an extension of the finite element method that was developed in order to overcome some limitations of the finite elements. It has been proposed for modeling and computing the overall properties of complex microstructures [81]. The principle of the method is to enrich the finite element approximation with additional shape functions in order to specify the interfaces which is independent of the background mesh.

Consider a domain $\Omega \subset \mathbb{R}^D$ (with D the dimension of the domain), the X-FEM displacement approximation can be expressed by :

$$\hat{u}^{XFEM}(\mathbf{x}) = \underbrace{\sum_{i \in I} \Phi_i(\mathbf{x}) u_i}_{\text{Classical}} + \underbrace{\sum_{j \in I^e} \Phi_j(\mathbf{x}) \psi(\mathbf{x}) u_j}_{\text{Enriched}} \tag{1.76}$$

where I (resp. I^e) stands for a set of nodes (resp. enriched nodes) in the mesh, Φ_i (resp. Φ_j) denotes the finite element shape functions for classical nodes (resp. the enriched nodes). The function $\psi(\mathbf{x})$ is an enrichment function with the desirable discontinuous properties. The second term in equation (1.76) allow us to model discontinuities or weak continuities which is independent of the classical finite element mesh.

In order to improve the finite element approximation, the choice of the enrichment function $\psi(\mathbf{x})$ is crucial. In the case of matrix/inclusion type composite, Sukumar et al. [100] were the first ones to combine the XFEM with a level-set method to construct the enrichment function related to interfaces. The interfaces implying weak continuities of the field are considered, i.e. the enrichment function is continuous while its derivative is discontinuous. In [100], the absolute value of the level-set function $L(\mathbf{x})$ is considered as an enrichment:

$$\psi(\mathbf{x}) = |L(\mathbf{x})| \tag{1.77}$$

$L(\mathbf{x})$ is called level-set function, which is a representation of a curve Γ (in 2D) or a surface (in 3D) described by the iso-zero contour (in 2D) or surface (in 3D) of an implicit scalar function:

$$\Gamma = \{\mathbf{x} | \psi(\mathbf{x}) = 0\} \tag{1.78}$$

This level-set function is usually chosen as the signed distance to the curve (resp. surface). The shape of the curve (resp. surface) Γ can be modified based on the evolution of $\psi(\mathbf{x})$, following a transport equation.

As the level-set is interpolated on the computational mesh, the density of computational mesh directly affects the accuracy of the XFEM solution. Despite XFEM allows the use of uniform meshes, the mesh should be fine enough to represent the geometrical information.

FCM method

Proposed by Parvizian *et al.* [87], the Finite Cell Method (FCM) is an extension to the classcial finite element method. The FCM can be interpreted as a combination of a fictitious domain concept with higher-order finite elements, adaptive integration, and weak enforcement of boundary conditions. The core idea of the method is to use a simple structured mesh of higher-order basis functions for the approximation of the solution fields.

In the FCM, the principle is to embed the physical domain Ω into a domain Ω_e of simpler shape. Therefore the integration of the weak form of equilibrium has to be extended over Ω_e.

Applying the FCM simplifies the meshing process, since a simple Cartesian mesh is used. The geometry of the micro-structure and the different material properties are treated during the integration of the stiffness matrices of the cells. In this way, the effort is shifted from mesh generation towards the numerical integration, which can be performed adaptively in a fully automatic way.

Moreover, the existing algorithms and solution methods can be used because of the similarity between the FCM and the FEM [25].

Conclusions

In the first chapter, we have presented the state of the art of the mean field methods and full field method which can be used to compute the effective properties for a composite material.

In the case of periodic composite, the material period is identified as the Representative Volume Element. As the RVE becomes more complex, especially in the cases with very thin or tiny inclusions or inclusions coated with a thin pellicle, some difficulties arise : to accurately model such RVEs, we need a huge number of meshes (especially in 3D) or a high resolution image. Although some numerical advances allow the study of very high resolution 3D images, the need to efficiently compute the effective properties of more and more complex RVE subsists.

In the case of finite element methods, one difficulty, due to the heterogeneity, is to accurately approximate integrals defining the energy bi-linear form

involved in the weak formulation of the homogenization modeling see [7,24,95]. It usually requires a conforming mesh but the building such a conforming and periodic mesh with complex geometries is not trivial, see for instance [96].

To circumvent the meshing difficulty, several approaches have been considered, such as eXtended Finite Element Method (XFEM) [100], or Finite Cell Methods (FCM) [25]. The XFEM is combined with the Level Set Method to define the inclusions and enriched shape functions [106]. The FCM considers only one structured mesh the elements of which are then called cells. The FCM uses cell subdivisions to ensure a better approximation of the integrals, see [25, 62].

We propose a new approach, based on the finite element method, to efficiently compute the effective properties of composite by remedying the meshing difficulty of existing numerical methods. This is the main objective of this Ph.D work and the next chapter is fully dedicated to introduce this new approach called phantom domain finite element method.

Chapter 2

A Phantom domain Finite Element Method

Contents

Introduction

The PFEM method is inspired by the Fictitious Domain Method (FDM), a technique used to solve elliptic boundary value problems in domain with complex boundaries or interfaces for which the meshing or the repetition of the meshing can induces difficulties, see [38]. To remedy this, distinct meshes are considered, one main structured mesh and independent meshes of the interfaces or inclusions. The fictitious domain method is then equivalent to a constrained quadratic optimization problem : the relations between the meshes or the interface or boundary conditions are taken in account with the help of Lagrange multipliers, see [38].

While the distinct independent meshes is also the basis for the PFEM, it differs from the standard Fictitious Domain Method since we shall not introduce Lagrange multipliers: it does not solve a constrained or coupled problem. It is also different from other variants of the Fictitious Domain Method such as the Finite Cell Method [25] as we employ a true (conformal) mesh of the inclusion instead of refining the computation within the element (or cell) that are being cut by the boundary of an inclusion see [25, 62].

Actually, the use of isoparametric element on a structured mesh of the RVE allows us to substitute the inclusion's mesh for the matrix's mesh in a very simple way by the mean of the definition of a Substitution Matrix. Our method can be directly applied to inclusions of any kind of shape or geometry, as long as a mesh is available. The inclusions meshes appear then as phantom meshes.

Even though, our method has been developed mainly to perform numerical homogenization, for the sake of simplicity, we shall first present our method in detail for a thermal conductivity equilibrium problem. Afterwards, the PFEM method is extended to the linear elasticity problem. Numerical experiments are given in the following in order to verify the PFEM method in both one inclusion cases and several inclusions cases.

2.1 Thermal conductivity problem

Let Ω represents a domain constituted by a heterogeneous material. Under the action of external heat source f, imposed temperature u_0 on Γ_D and imposed heat flux F on Γ_N, the thermal boundary value problem writes:

$$\begin{cases} div\ \mathbf{q} + f = 0 & \text{in } \Omega \\ u = u_0 & \text{on } \Gamma_D \\ \mathbf{q}.\mathbf{n} = F & \text{on } \Gamma_N \end{cases} \tag{2.1}$$

with $\Gamma_D \cup \Gamma_N = \partial\Omega$, u denotes the temperature and $\mathbf{q}$ is the heat flux. The domain Ω is shown in the Figure 2.1.

In theory, Ω can be of arbitrary shape but in the sequel we shall only consider domain such as $\Omega = [0,1]^d$ with $d = 2, 3$ since we want to use a structured mesh.

Λ is a thermal conductivity second order tensor :

$$\mathbf{q} = \Lambda \nabla u \tag{2.2}$$

For the sake of simplicity, let us consider a material domain Ω to be constituted by two homogeneous and isotropic media : the matrix $\Omega \setminus \Omega_{inc}$ and

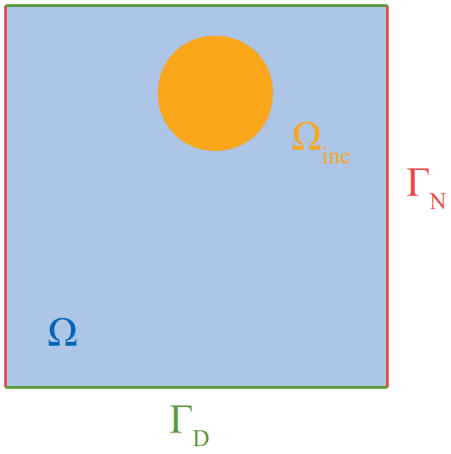

Figure 2.1: A domain Ω with inclusions Ω_{inc} under the imposed temperature u_0 on Γ_D and imposed heat flux F on Γ_N.

inclusions Ω_{inc}. The conductivity matrix writes:

$$\Lambda = \begin{cases} \Lambda_{mat} & in\ \Omega \backslash \Omega_{inc} \\ \Lambda_{inc} & in\ \Omega_{inc} \end{cases}$$

In other words, Λ_{mat} and Λ_{inc} are respectively the constant thermal conductivity tensors of the matrix and the inclusion.

The equation (2.1) is equivalent to the variational formulation:

$$\begin{cases} \text{Find } u \in V_{adm} = \{u \in H^1(\Omega)/u|_{\Gamma_D} = u_0\} \\ \int_\Omega (\Lambda \nabla u).\nabla u^* = \int_\Omega f u^* + \int_{\Gamma_N} F u^*,\ \forall u^* \in V_0 \end{cases} \tag{2.3}$$

with V_0 a vector subspace associated to the affine admissible space V_{adm}:

$$V_0 = \{u \in H^1(\Omega)/u|_{\Gamma_D} = 0\}$$

Classically, the problem (2.3) is a well posed problem from the Lax-Milgram framework [90]. The unique solution of the problem (2.3) also minimize the energy functional $J(u)$ in V_{adm}:

$$J(u) = \frac{1}{2} \int_\Omega (\Lambda \nabla u).\nabla u - \int_\Omega f u \tag{2.4}$$

In a composite material, Λ is not constant but can be piece-wise constant. For instance, If the mesh element belongs to the matrix, Λ takes the value of Λ_{mat} whereas if the mesh element belongs to the inclusion, Λ takes the value of Λ_{inc}.

With a conformal Finite Element Method, we define an interpolation space V^h of dimension n such that any $u^h \in V^h$ can be represented by $\hat{u} \in \mathbb{R}^n$. With the help of a stiffness matrix K and a vector L, we have:

$$J(u^h) = \frac{1}{2}\int_\Omega (\Lambda \nabla u^h).\nabla u^h - \int_\Omega f u^h \tag{2.5}$$

$$J(u^h) = \left[\hat{u}\right]^\top K \left[\hat{u}\right] - \left[\hat{u}\right]^\top L \tag{2.6}$$

With inclusions in complex geometries, it can be costly to build an conforming mesh in order to accurately compute the functional integral by the conventional Finite Element Method.

Split of the Energy form

As the material is composed of two constituent, we split the energy functional in (2.4) into the corresponding parts :

$$J(u) = \frac{1}{2}\int_{\Omega\setminus\Omega_{inc}} (\Lambda_{mat}\nabla u).\nabla u + \frac{1}{2}\int_{\Omega_{inc}} (\Lambda_{inc}\nabla u).\nabla u - \int_\Omega f u \tag{2.7}$$

The main idea of the PFEM consists in using two distinct and *a priori* incompatible and independent meshes representing the whole domain Ω and inclusions Ω_{inc} instead of a unique conformal mesh matching the geometry of the inclusion, see Figure 2.2 for an illustration in the case of one disk inclusion in $\Omega = [0,1]^2$.

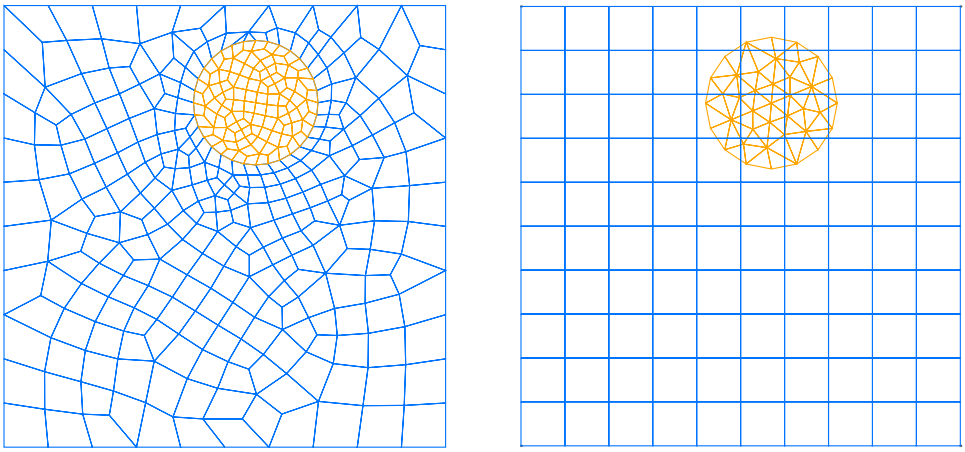

Figure 2.2: A conforming mesh (left) and independent meshes (right) for one disk inclusion in domain $\Omega = [0,1]^2$

From (2.7), we can rewrite the energy functional:

$$J(u) = \underbrace{\frac{1}{2}\int_{\Omega}(\Lambda_{mat}\nabla u).\nabla u}_{J_{mat}} + \underbrace{\frac{1}{2}\int_{\Omega_{inc}}\left((\Lambda_{inc}-\Lambda_{mat})\nabla u\right).\nabla u}_{J_{inc}} - \int_{\Omega} fu \tag{2.8}$$

The two split integrals J_{mat} and J_{inc} are respectively defined on the whole domain Ω and the inclusion Ω_{inc}.

The consideration of distinct meshes allow independent numerical computations of J_{mat} and J_{inc}. The functional J_{mat} can then be calculated in V^h with the help of a $n \times n$ matrix K_{mat} :

$$J_{mat}(u^h) = \frac{1}{2}\int_{\Omega}(\Lambda_{mat}\nabla u^h).\nabla u^h = \left[\hat{u}\right]^{\top} K_{mat}\left[\hat{u}\right] \tag{2.9}$$

On another hand, let us consider a conforming mesh of the inclusion Ω_{inc} independent of the mesh defining Ω. We define the interpolation space W^l of finite dimension p, associated to the inclusion's mesh so that any $v^l \in W^l$ can be represented by a vector $\hat{v} \in \mathbb{R}^p$. In order to simplify the presentation, the meshes will be denoted respectively as Ω and Ω_{inc}.

The functional J_{inc} can be defined in W^l with a $p \times p$ matrix K_{inc}:

$$J_{inc}(v^l) = \frac{1}{2}\int_{\Omega_{inc}}\left((\Lambda_{inc}-\Lambda_{mat})\nabla v^l\right).\nabla v^l = \left[\hat{v}\right]^{\top} K_{inc}\left[\hat{v}\right]. \tag{2.10}$$

Both the matrices K_{mat} and K_{inc} can be computed using standard finite element procedures.

A Substitution Matrix

We defined the matrices K_{mat} and K_{inc}, allowing to separately compute the energy functionals J_{mat} and J_{inc}. The objective is to relate $\hat{v}$, the Degrees of Freedom (DOFs) of the inclusion Ω_{inc} to $\hat{u}$, the DOFs of the structured mesh Ω.

With isoparametric elements and a structured mesh, it can easily be achieved : For each component v_i of $\hat{v}$, we have $v_i = v(N_i)$ where N_i is a node of Ω_{inc}. Let E_l, be an element of Ω in which the node N_i is included, see the Figure 2.3 for an illustration in a two dimensional case.

Let $\hat{x}$, $\hat{y}$, $\hat{z}$ be the coordinates of the nodes constituting the element E_l. With an isoparametric element, we usually define a reference element and its corresponding shape functions $\widehat{\Phi}$. Let (x_i, y_i, z_i) be the coordinates of the node N_i, and let (r_i, s_i, t_i) be its coordinates in the reference element associated to E_l. By definition, we have :

$$\begin{aligned} x_i &= \widehat{\Phi}(r_i, s_i, t_i)^{\top}\hat{x} \\ y_i &= \widehat{\Phi}(r_i, s_i, t_i)^{\top}\hat{y} \\ z_i &= \widehat{\Phi}(r_i, s_i, t_i)^{\top}\hat{z} \end{aligned}$$

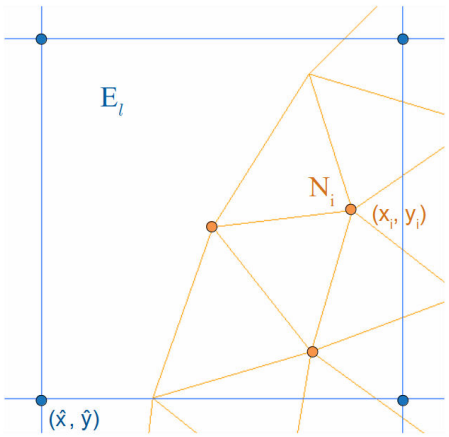

Figure 2.3: A node N_i from a triangular mesh of an inclusion in the quadrangular element E_l of the mesh Ω. Note that the nature of the inclusion's mesh (tri3) can be different from the structured mesh's (qua4).

Let v_i be the value of $\hat{v}$ at node N_i :

$$v_i = v(x_i, y_i, z_i) \tag{2.11}$$

As we work with isoparametric element, we also have :

$$v(x_i, y_i, z_i) = \widehat{\Phi}(r_i, s_i, t_i)^\top \hat{u}, \tag{2.12}$$

In other words, we have the relation of the value v_i at a node of the inclusion's mesh from the values $\hat{u}$ on the mesh of the element E_l :

$$v_i = \widehat{\Phi}(r_i, s_i, t_i)^\top \hat{u}. \tag{2.13}$$

We fill up (completing with zeros) the relation (2.13) to all the values of $\hat{u}$ at the other nodes of the mesh Ω. Let us denote S_i the $1 \times n$ line matrix, with n the total number of DOFs of the structured mesh Ω, we have :

$$v_i = v(x_i, y_i, z_i) = \widehat{\Phi}(r_i, s_i, t_i)^\top \hat{u} = S_i \hat{u},$$

($\hat{u}$ abusively represents the nodal values of u in an element E_l but also in the whole domain Ω).

To make it clear, we give an example for the two dimensional case which can be similarly extended to three dimensional case, to illustrate the construction of the substitution matrix S. Let's consider a structured mesh of Ω with resolution 3 (3×3 elements and 4×4 nodes) and a mesh of triangle inclusion Ω_{inc} with 1 element and 3 nodes, shown in Figure 2.4. It can be observed that, the node N_1 of Ω_{inc} is included in one element E_l of Ω with nodes $5, 6, 9, 10$. In

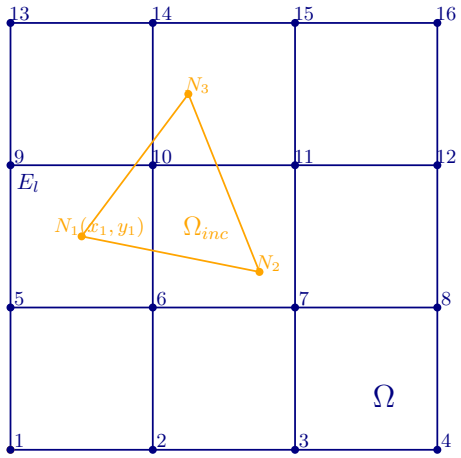

Figure 2.4: A triangular mesh of an inclusion in the structured mesh Ω with mesh resolution equal to 3.

the general case of a structured mesh Ω, if we know the coordinates (x_i, y_i) of the node N_i, it is easy to calculate in which element of Ω the node N_i belongs.

In this example, as Ω is a quadrilateral mesh, the shape function $\widehat{\Phi}$ of the reference element associated to E_l writes:

$$\begin{cases} \Phi_1(r,s) = (1-r)(1-s) \\ \Phi_2(r,s) = r(1-s) \\ \Phi_3(r,s) = r\,s \\ \Phi_4(r,s) = (1-r)s \end{cases}$$

We denote (r_1, s_1) as the coordinates of the node N_1 in the reference element associated to E_l.

Within the isoparametric element E_l, we have the value v_1 at node N_1:

$$v_1 = v(x_1, y_1) = \widehat{\Phi}(r_1, s_1)^\top \hat{u}$$

The first line of the substitution matrix S_1, which correspond to the node N_1 of the inclusion's mesh Ω_{inc}, is defined as:

$$\begin{bmatrix} v_1 \end{bmatrix} = \underbrace{\begin{bmatrix} 0 & \cdots & \Phi_1 & \Phi_2 & 0 & 0 & \Phi_4 & \Phi_3 & \cdots & 0 \end{bmatrix}}_{S_1} \begin{bmatrix} \vdots \\ u_5 \\ u_6 \\ \vdots \\ u_9 \\ u_{10} \\ \vdots \end{bmatrix}$$

Considering every nodes of Ω_{inc}, we finally obtain the substitution matrix S constructed line by line, which substitutes $\hat{v}$, the DOFs associated to the inclusion's mesh Ω_{inc}, for $\hat{u}$, the DOFs associated to the mesh Ω :

$$\hat{v} = S\hat{u} \tag{2.14}$$

We emphasize on the fact that the construction of the substitution matrix S is completely formulated. Neither sorting nor testing is required in the procedure. Consequently, the construction of the substitution matrix S is computationally costless.

We are then able to rewrite the energy quadratic form computed on the inclusion J_{inc} :

$$\begin{aligned} J_{inc} &= \left[\hat{v}\right]^\top K_{inc} \left[\hat{v}\right] \\ &= \left[S\hat{u}\right]^\top K_{inc} \left[S\hat{u}\right] \\ &= \left[\hat{u}\right]^\top \left(S^\top K_{inc} S\right) \left[\hat{u}\right] \end{aligned}$$

Finally, we obtain the main energy quadratic form defined only on $\hat{u}$:

$$\begin{aligned} J(u) &= J_{mat}(u) + J_{inc}(u) - \left[\hat{u}\right]^\top L \\ &= \left[\hat{u}\right]^\top K_{mat} \left[\hat{u}\right] + \left[\hat{u}\right]^\top \left(S^\top K_{inc} S\right) \left[\hat{u}\right] - \left[\hat{u}\right]^\top L \\ &= \left[\hat{u}\right]^\top \left(K_{mat} + S^\top K_{inc} S\right) \left[\hat{u}\right] - \left[\hat{u}\right]^\top L \end{aligned} \tag{2.15}$$

In other word with the matrix defined in (2.15), we are applying a finite element method with the interpolation space defined on the structured mesh of the domain Ω.

Multiple inclusions treatment

The PFEM computation in case of multiple inclusions is quiet the same as in the simple inclusion case. We show an illustration of FEM and PFEM mesh in Figure 2.5 for RVE with one disk inclusion and one square inclusion.

The PFEM computation procedure is repeated independently for each inclusion; all computations can be performed in parallel. The principle is very general and flexible, the inclusion's meshes do not have to be of identical types, we can mix different types of mesh.

It should emphasized that, contrary to usual Fictitious Domain Methods, the PFEM, is not a constrained or a coupled problem, there is no Lagrange multiplier nor additional DOFs. The substitution matrix allows to substitute the DOFs associated to the inclusions meshes; the problems are thus solely solved on the DOFs associated to the structured mesh of the domain Ω.

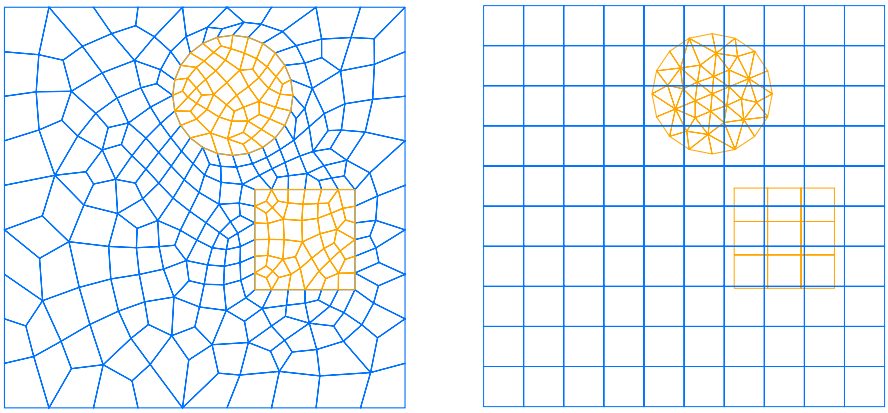

Figure 2.5: A conforming mesh (left) and independent meshes (right) for one disk inclusion and one square inclusion in domain $\Omega = [0,1]^2$

Pixelization and fine enough inclusions mesh

In the presentation of the method, no assumptions have been made on the independent meshes. However, in order to obtain an accurate approximation of the integrals form (2.8), the mesh of the inclusion must be fine enough compared to the structured mesh Ω; this is also a standard requirement in Fictitious Domain Methods see [38, 88].

As an illustration, let us consider a triangle inclusion in a domain $\Omega = [0,1]^2$ of structured meshes by two resolutions. The inclusion mesh remains the same with one element and three nodes. In Figure 2.6 we have drawn in pink the elements of Ω which are the substitution of the inclusion's mesh, we can see them as the pixels (or voxels in 3D) resulting from the mesh of the inclusion. On the 3×3 mesh (left), we can see that the elements in pink recover entirely the inclusion while they do not on the 6×6 mesh (right) : the one-element inclusion mesh is fine enough for the 3×3 mesh, but not for the 6×6 mesh. In other words, the finer the structured mesh Ω is, the finer the inclusion's mesh Ω_{inc} must be. The substitution of each node of Ω_{inc} for an element of Ω defines a pixelization of the inclusion.

In the rest of this paper, we shall only consider fine enough mesh for the inclusion in order that the resulting pixelization recovers the inclusions entirely, see Section 2.3.2 for a more detailed analysis.

Convergence

In the general case with non matching meshes, PFEM can be seen a better approximation than a conforming Finite Element Method applied to an ap-

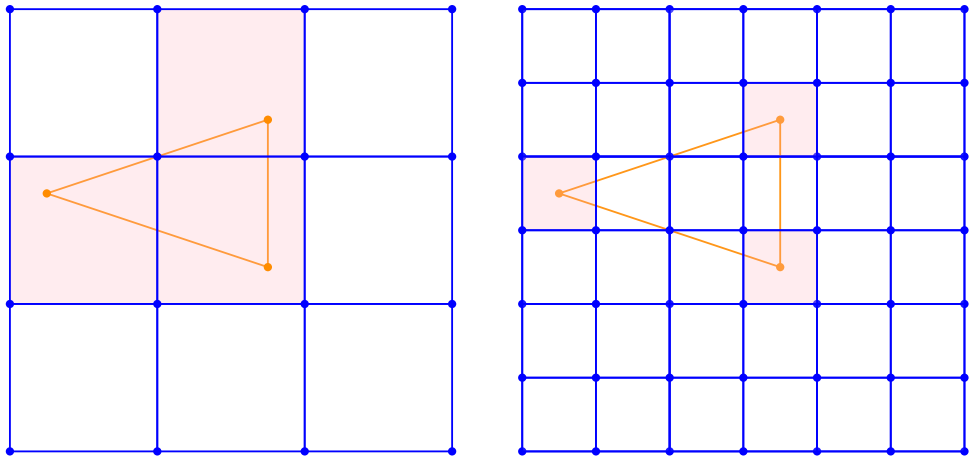

Figure 2.6: A one-element mesh of a triangle inclusion with 3×3 (left) and 6×6 (right) structured meshes of $\Omega = [0,1]^2$. The pink elements define the pixels resulting form the inclusion's mesh.

proximation of the inclusion geometry by a pixelization procedure, which is convergent.

Since a finer mesh of Ω induces a finer pixelization and thus a better approximation of the inclusion, we deduce that the PFEM is a convergent method as long as the inclusion's mesh is fine enough to define a correct pixelization. In other words, if there is a gap in the pixelization, see the right side of Figure 2.6, the convergence of the PFEM is not ensured.

Error approximation

Since the material is heterogeneous, the discontinuity of the "constitutive law" implies that the PFEM solution does not possess, in general, the correct weak continuity at the interfaces between the matrix phase and the inclusion phase.

2.2 Linear elasticity problem

The extension of the PFEM to linear elasticity problems is straightforward. Under the action of external volume force $\mathbf{f}$, imposed displacement $\mathbf{u}_d$ on Γ_D and imposed force $\mathbf{F}_n$ on Γ_N , the linear elasticity equilibrium problem writes:

$$\begin{cases} div(\overline{\sigma}) + \mathbf{f} = \mathbf{0} & \text{in } \Omega \\ \overline{\sigma} = \mathbb{C}\,\overline{e}(\mathbf{u}) & \text{in } \Omega \\ \mathbf{u} = \mathbf{u}_d & \text{on } \Gamma_D \\ \overline{\sigma}\,\mathbf{n} = \mathbf{F}_n & \text{on } \Gamma_N \end{cases} \tag{2.16}$$

where $\Gamma_D \cup \Gamma_N = \partial\Omega$ the boundary of the domain Ω and $\overline{e}(\mathbf{u})$ is the linearized deformation tensor associated to the displacement $\mathbf{u}$, defined as:

$$\overline{e}(\mathbf{u}) = \frac{1}{2}(\nabla\mathbf{u} + \nabla\mathbf{u}^\top)$$

The variational formulation equivalent to the elastic problem (2.16) writes:

$$\begin{cases} \text{Find } \mathbf{u} \in V_{adm} = \{\mathbf{u} \in H^1(\Omega)/\mathbf{u}|_{\Gamma_D} = \mathbf{u}_d\} \\ \displaystyle\int_\Omega (\mathbb{C}\,\overline{e}(\mathbf{u})) : \overline{e}(\mathbf{u}^*) = \int_\Omega \mathbf{f}\mathbf{u}^* + \int_{\Gamma_N} \mathbf{F}_n\mathbf{u}^*, \ \forall u^* \in V_0 \\ V_0 = \{\mathbf{u} \in H^1(\Omega)/\mathbf{u}|_{\Gamma_D} = 0\} \end{cases} \tag{2.17}$$

The problem (2.17) involves a quadratic deformation energy form : for any displacement $\mathbf{u}$,

$$J(\mathbf{u}) = \int_\Omega (\mathbb{C}\,\overline{e}(\mathbf{u})) : \overline{e}(\mathbf{u}) \tag{2.18}$$

The second order elasticity tensor $\mathbb{C}$ defining the constitutive law of the material :

$$\mathbb{C} = \begin{cases} \mathbb{C}_{mat} & in\ \Omega\backslash\Omega_{inc} \\ \mathbb{C}_{inc} & in\ \Omega_{inc} \end{cases}$$

We then just split the energy form as in the thermal case :

$$J(\mathbf{u}) = \int_\Omega (\mathbb{C}_{mat}\,\overline{e}(\mathbf{u})) : \overline{e}(\mathbf{u}) + \int_{\Omega_{inc}} ((\mathbb{C}_{inc} - \mathbb{C}_{mat})\,\overline{e}(\mathbf{u})) : \overline{e}(\mathbf{u}) \tag{2.19}$$

Associated to the structured mesh of the entire domain Ω, let us define an interpolation space $\mathbf{V}^h$ of finite dimension n such that any displacement $\mathbf{u} \in \mathbf{V}^h$ can be represented by $\hat{u} \in \mathbb{R}^n$. On another hand, let us define the interpolation space $\mathbf{W}^l$ of finite dimension p, associated to the inclusion's mesh so that any displacement $\mathbf{v} \in \mathbf{W}^l$ can be represented by a vector $\hat{v} \in \mathbb{R}^p$. We define the $n \times n$ and $p \times p$ matrices K_{mat} and K_{inc}:

$$\int_\Omega (\mathbb{C}_{mat}\,\overline{e}(\mathbf{u})) : \overline{e}(\mathbf{u}) = \left[\hat{u}\right]^\top K_{mat} \left[\hat{u}\right], \quad \forall \mathbf{u} \in \mathbf{V}^h \tag{2.20}$$

$$\int_{\Omega_{inc}} ((\mathbb{C}_{inc} - \mathbb{C}_{mat})\,\overline{e}(\mathbf{v})) : \overline{e}(\mathbf{v}) = \left[\hat{v}\right]^\top K_{inc} \left[\hat{v}\right], \quad \forall \mathbf{v} \in \mathbf{W}^l \tag{2.21}$$

We define a substitution matrix S, similarly to the thermal case but for all the components of the displacement. For example, in three-dimensional elastic case, we have 3 DOFs for each node N_i of the inclusion's mesh Ω_{inc}, instead of 1 DOF in the thermal case. For each component v_j of $\hat{v}$, we have:

$$v_j = v(N_i), \text{ for } j = 3i, 3i+1, 3i+2$$

Let (x_i, y_i, z_i) be the coordinates of the node N_i, let (r_i, s_i, t_i) be its coordinates in the reference element associated to E_l and let $\widehat{\Phi}$ be its corresponding shape function, we have the line matrix S_j writes:

$$v_j = v(x_i, y_i, z_i) = \widehat{\Phi}(r_i, s_i, t_i)^\top \hat{u} = S_j \hat{u}, \text{ for } j = 3i, 3i+1, 3i+2$$

By this way, we can bind the DOFs $\hat{v}$ defined on the inclusion Ω_{inc} to the DOFs $\hat{u}$ defined on the structured mesh Ω as:

$$\hat{v} = S\hat{u}$$

The dimension of the substitution matrix S becomes larger with respect to the increase of DOFs in the elastic case. We can then rewrite the deformation energy form :

$$J(\mathbf{u}) = \left[\hat{u}\right]^\top \left[K_{mat} + S^\top K_{inc} S\right] \left[\hat{u}\right] \quad \forall \mathbf{u} \in \mathbf{V}^h \tag{2.22}$$

2.3 Numerical Experiments

In this section, we present some numerical experiments of the thermal boundary value problem 2.1 and the elastic boundary value problem 2.16. For the sake of simplicity, we consider isotropic constitutive laws for both linear problems.

2.3.1 Specifications of numerical experiments

Boundary conditions

- In thermal Pure Dirichlet boundary value problem, we impose a uniform gradient of temperature at the boundary of Ω, which reads:

$$u = \mathbf{g}.\mathbf{x}, \quad \forall \mathbf{x} \in \partial\Omega \tag{2.23}$$

  with $\mathbf{g} = [1, 0]$ an imposed vector in two dimensional case, $\mathbf{x}$ denote the coordinate of the nodes.

- In thermal Pure Neumann boundary value problem, we impose a uniform heat flux at the boundary of Ω, that reads:

$$\mathbf{q}.\mathbf{n} = \mathbf{Q}.\mathbf{n}, \quad \forall \mathbf{x} \in \partial\Omega \tag{2.24}$$

  with $\mathbf{Q} = [0, 1]$ an imposed vector, $\mathbf{n}$ denotes outward pointing unit normal at each point on the boundary $\partial\Omega$.

- In elastic Dirichlet boundary value problem, we impose a displacement at point $\mathbf{x}$ belonging to the boundary $\partial\Omega$:

$$\mathbf{u} = \overline{E}\,\mathbf{x}, \quad \forall \mathbf{x} \in \partial\Omega \tag{2.25}$$

with $\overline{E} = \begin{bmatrix} 1 & 0 \\ 0 & 0 \end{bmatrix}$, an imposed 2×2 tensor in two dimensional case.

- In elastic Neumann boundary value problem, we prescribe a traction vector at the boundary, reads:

$$\overline{\sigma}\,\mathbf{n} = \overline{\Sigma}\,\mathbf{n}, \quad \forall \mathbf{x} \in \partial\Omega \tag{2.26}$$

with $\overline{\Sigma} = \begin{bmatrix} 0 & 0 \\ 0 & 1 \end{bmatrix}$ an imposed 2×2 traction tensor.

The corresponding Dirichlet and Neumann boundary value problems are respectively in relation with the Kinematic Uniform Boundary Conditions (KUBC) and the Static Uniform Boundary Condition (SUBC) used for numerical homogenization in the section 1.3.2 and will be studied in the next chapter.

Inclusion types

In two dimensional cases, we consider the domain Ω defined with inclusions of elementary geometry such as disk and square, of course any kind of geometry can be considered.

- A disk is defined by the coordinates of its center and its diameter d, see Figure 2.7.

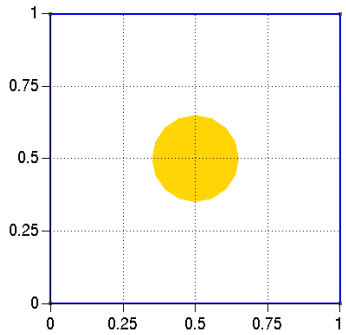

Figure 2.7: One disk inclusion of diameter $d = 0.3$ in domain Ω, volume fraction $\rho = 0.0707$

- A square is defined by the coordinates of its center and its side l. For example, if the square inclusion is centered with side $l = 0.3$, the volume fraction is thus $\rho = 0.09$, see Figure 2.8.

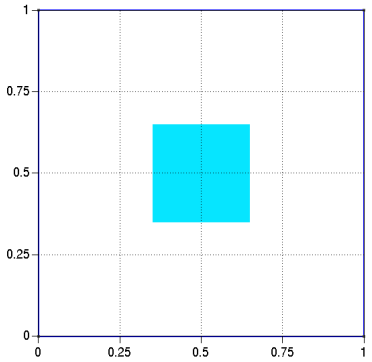

Figure 2.8: One square inclusion of side $l = 0.3$ in domain Ω, volume fraction $\rho = 0.09$

Contrast parameter of the constitutive law

We define a contrast parameter as the ratio between the characteristic coefficient of inclusions and that of matrix :

- In the thermal case :

$$c_{thermal} = \frac{\lambda_{inc}}{\lambda_{mat}}$$

- In the linear elasticity case :

$$c_{elastic} = \frac{E_{inc}}{E_{mat}}$$

$$\nu_{inc} = \nu_{mat}$$

where λ_{inc}, E_{inc} and ν_{inc} (resp. λ_{mat}, E_{mat} and ν_{mat}) are the conductivity, the Young's modulus and the Poisson's ratio of the inclusion (resp. the matrix). For isotropic linear elastic materials, we introduce the bulk modulus k, defined as:

$$k = \frac{E}{3(1-2\nu)}$$

As we set that the Poisson's ratio ν for both inclusion and matrix are the same, the contrast parameter can also be expressed by the bulk modulus k:

$$c_{elastic} = \frac{k_{inc}}{k_{mat}}$$

In all cases presented in this section, to fix the idea, we chose to set the contrasts $c_{thermal}$ and $c_{elastic}$ to 100.

Computing resources

The computations are performed by a finite element library code, named PFEM, developed by the authors, in Python/Fortran. We use the PETSc [1] library to solve the linear systems. The meshes are generated with the Gmsh software [34].

In some cases, as the RVE resolution may involves millions of DOFs, we used Myria, a HPC cluster located in CRIANN [2]. However, all of the computations presented in this dissertation can be performed on personal computer (We used a hp laptop with Intel Core i5 processor and 16 GB memory).

2.3.2 Meshes of PFEM

The PFEM meshes are consist of one structured mesh of the domain Ω and independent meshes of each inclusion Ω_{inc}, as shown in Figure 2.5.

Structured mesh of the domain Ω

Let us consider a d dimensional domain $\Omega \in [0,1]^d, d = 2,3$ representing a medium of a heterogeneous material embedding one or several inclusions. The structured mesh of the domain Ω is characterized by its resolution. If $d = 3$, a resolution n corresponds to a $n \times n \times n$ subdivision in all three space dimension, see for instance Table 2.1 with a Ω mesh resolution $n = 10$ in two dimensional and three dimensional case.

Dimension	Resolution	Structured mesh of the domain Ω	
$d = 2$	$n = 10$	10^2 4-nodes quadratic element	121 nodes
$d = 3$	$n = 10$	10^3 8-nodes hexaedric element	1331 nodes

Table 2.1: Structured mesh elements of the domain Ω in two dimensional and three dimensional case.

In periodic homogenization, the domain Ω can be seen as a Representative Volume Element (RVE) of the material. In order to put in coherent with the periodic homogenization part, in the following, we note the mesh resolution as N_{rve}. Associated to the resolution, we define the parameter $h_{rve} = 1/N_{rve}$, representing the characteristic length of an element of the mesh.

[1] Portable Extensible Toolkit for Scientific computation: https://www.mcs.anl.gov/petsc

[2] Regional Computer Center and Digital Applications of Normandy: https://www.criann.fr

Independent meshes of the inclusions Ω_{inc}

As we presented in the section 2.1, the pixels of the domain Ω, which are resulting from the inclusion's mesh Ω_{inc}, should recover entirely the inclusion in order to obtain an accurate approximation of the integrals. As a result, the inclusion's mesh needs to be sufficiently fine depending on the structured mesh.

Besides the resolution N_{rve}, we define another parameter N_{inc} to set the element size of the mesh of the inclusions. The relation between N_{rve} and N_{inc} would have an effect on the precision of PFEM method. So that, we set h_{rve} and h_{inc} respectively the characteristic length of the mesh of the RVE and the inclusion, and we define the ratio η as :

$$\eta = \frac{h_{rve}}{h_{inc}} \tag{2.27}$$

A value of η larger than 1 means a finer mesh of the inclusion than the matrix's, in other words, a pixelization of the inclusion. In order to illustrate the influence of η on the inclusion's mesh, in Figure 2.9, we have drawn in blue the mesh elements of Ω, and in yellow the the inclusion's mesh for $\eta = 0.5, 1, 2$.

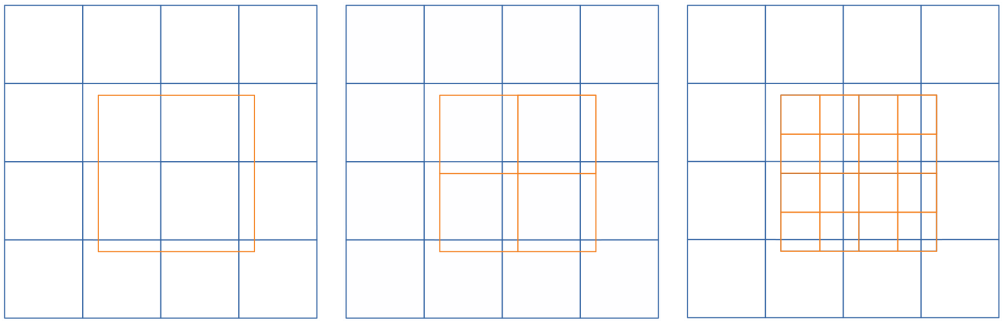

(a) $\eta = 0.5$ (b) $\eta = 1$ (c) $\eta = 2$

Figure 2.9: Meshes of a square inclusion (yellow) in a 4×4 structured mesh of $\Omega = [0, 1]^2$ (blue) for $\eta = 0.5, 1, 2$.

Numerical experiments of the thermal Dirichlet boundary value problem (2.1) have been performed to evaluate the influence of η. The mesh resolution N_{rve} is set to 60, which relates to 3600 4-nodes quadratic elements. The value of $\eta = 0.5, 1.0, 2.0$ relate to a inclusion's mesh with $405, 1620, 6480$ elements respectively.

In Figure 2.10 and Figure 2.11, we present the relative error of H^1 semi-norm of the computed temperature against the value of η, respectively in the case of one disk inclusion and one square inclusion.

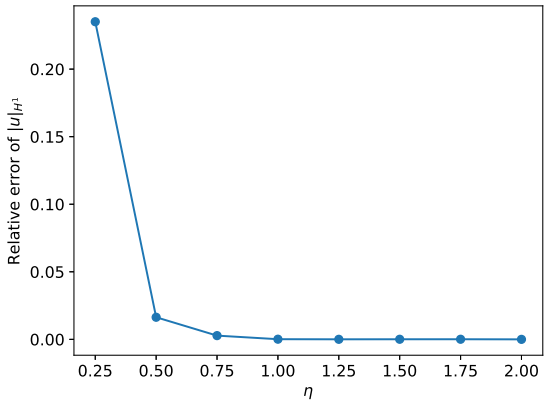

Figure 2.10: Case of one disk inclusion with diameter $d = 0.3$. Relative error of H^1 semi-norm of the temperature against the value of η with $N_{rve} = 150$.

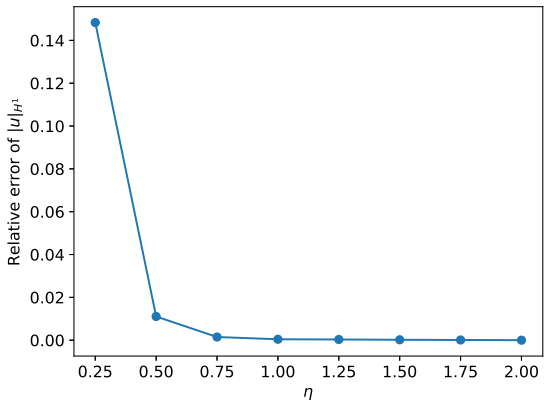

Figure 2.11: Case of one square inclusion with side $l = 0.3$. Relative error of H^1 semi-norm of the temperature against the value of η with $N_{rve} = 150$.

We have found that, as we increase the value of η, the norm value is decreasing. However, the evolution of the value becomes less important from the point $\eta = 1$. In the following study, we set η to 1, with this condition, we consider that the inclusion's mesh is fine enough to make the pixelization recovers the inclusion entirely.

2.3.3 Convergence study

In order to present the numerical results, we compute L^2 norm and H^1 semi-norm of the temperature and displacement respectively for thermal conductivity problem and linear elasticity problem. In the $L^2(\Omega)$ space, the correspond-

ing L^2 norm is defined as:

$$\|u\|_{L^2(\Omega)} = \left(\int_\Omega u^2\right)^{\frac{1}{2}} \tag{2.28}$$

In the Hilbert space $H^1(\Omega)$, we note the corresponding H^1 semi-norm:

$$|u|_{H^1(\Omega)} = \left(\int_\Omega (\nabla u)^2\right)^{\frac{1}{2}} \tag{2.29}$$

In practice, L^2 norm and H^1 semi-norm are computed with the help of the mass matrix M and the rigidity matrix K.

A conformal fine mesh of FEM (with a resolution $N_{rve} = 150$) is used as the reference solution. The contrast between matrix and inclusion is set to 100. In order to study the convergence of PFEM in static problems, we compute the relative error of L^2 norm and H^1 semi-norm of the temperature and displacement respectively for thermal conductivity problem and linear elasticity problem, which reads:

$$\text{Relative error}(\|u\|_{L^2}) = \frac{|\ \|u\|_{L^2}^{pfem} - \|u\|_{L^2}^{fem}\ |}{\|u\|_{L^2}^{fem}} \tag{2.30}$$

$$\text{Relative error}(|u|_{H^1}) = \frac{|\ |u|_{H^1}^{pfem} - |u|_{H^1}^{fem}\ |}{|u|_{H^1}^{fem}} \tag{2.31}$$

with $|x|$ denotes the absolute value of x.

In Figure 2.12, the relative error are plotted for a static thermal conductivity problem with Dirichlet boundary conditions 2.23 and Neumann boundary conditions 2.24 in the domain Ω with one disk inclusion $d = 0.3$. The linear elasticity case is shown in Figure 2.13.

We notice that, the behavior of the norms in thermal conductivity problem is similar to that in linear elasticity problem. In both cases, a linear convergence with respect to the number of resolution is observed for L^2 norm. The convergence of H^1 semi-norm is lightly deviated to the linear rate. Compared to the reference FEM solution, the relative error of L^2 norm with Dirichlet boundary condition is in order of magnitude 10^{-3} with a resolution of $N_{rve} = 140$, which is smaller than that with Neumann boundary condition.

In Figure 2.14, we draw the relative error of L^2 norm and H^1 semi-norm for a static thermal Dirichlet boundary value problem and Neumann boundary value problem in the domain Ω with one square inclusion $l = 0.3$ against the resolution N_{rve}.

The convergence study of PFEM for a domain Ω with one square inclusion $l = 0.3$ in linear elasticity case is presented in Figure 2.15.

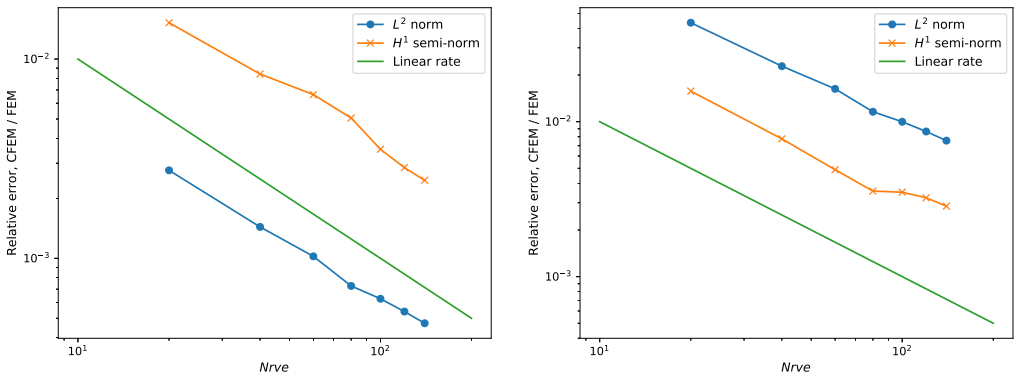

(a) Relative error for Dirichlet boundary value problem

(b) Relative error for Neumann boundary value problem

Figure 2.12: Case of one disk inclusion $d = 0.3$. Relative error of L^2 norm and H^1 semi-norm for a static thermal Dirichlet boundary value problem and Neumann boundary value problem in the domain Ω.

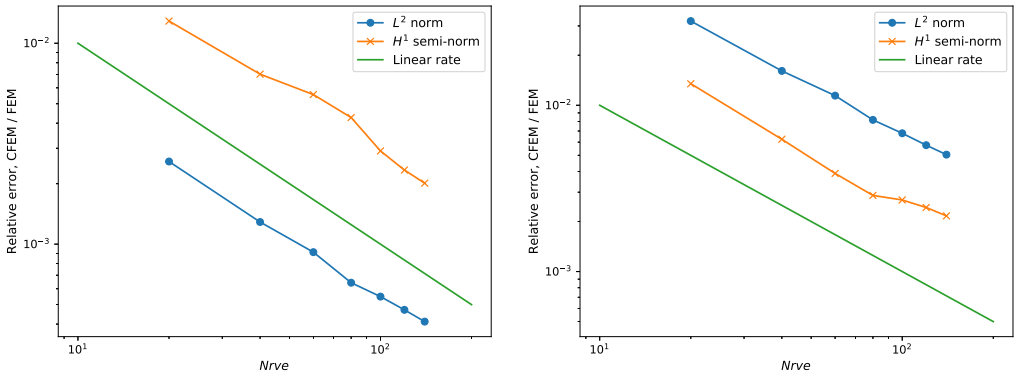

(a) Relative error for Dirichlet boundary value problem

(b) Relative error for Neumann boundary value problem

Figure 2.13: Case of one disk inclusion $d = 0.3$. Relative error of L^2 norm and H^1 semi-norm for a static elastic Dirichlet boundary value problem and Neumann boundary value problem in the domain Ω.

We notice a linear convergence of L^2 norm and H^1 semi-norm for both thermal conductivity and linear elasticity problem. This study shows the convergence of the method against the resolution N_{rve}.

In the case of square inclusions, we distinguish a special case that the mesh of domain Ω and the mesh of inclusion Ω_{inc} are matching. For example, let's consider a centered square inclusion of side $l = 0.5$. If the resolution N_{rve} is in multiple of 4, geometrically, the mesh of Ω will match with the mesh of the square inclusion, see for instance in Figure 2.16, where the inclusion's mesh Ω_{inc} is colored in orange and the mesh of domain Ω in blue.

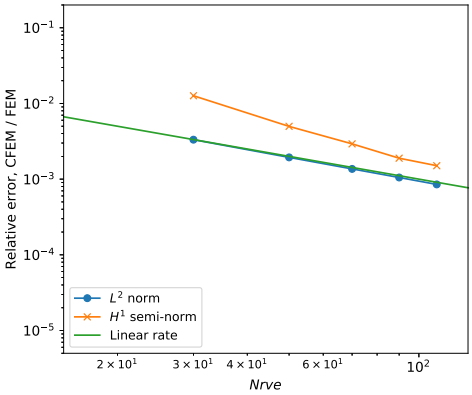

(a) Relative error for Dirichlet boundary value problem

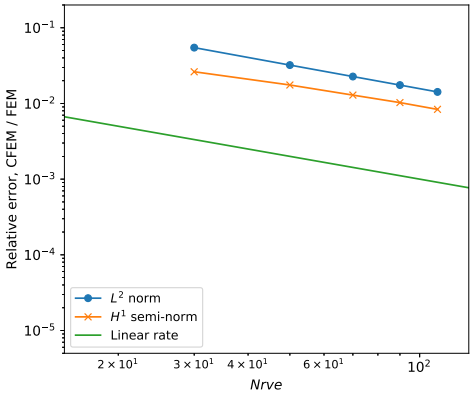

(b) Relative error for Neumann boundary value problem

Figure 2.14: Case of one square inclusion $l = 0.3$. Relative error of L^2 norm and H^1 semi-norm for a static thermal Dirichlet boundary value problem and Neumann boundary value problem in the domain Ω.

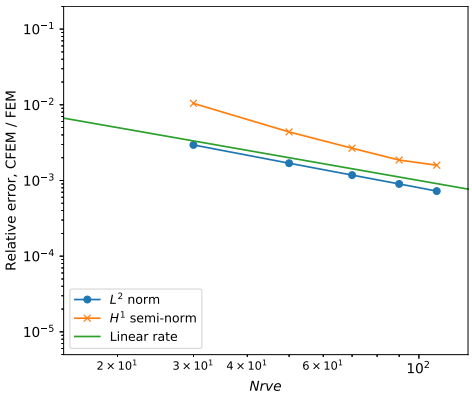

(a) Relative error for Dirichlet boundary value problem

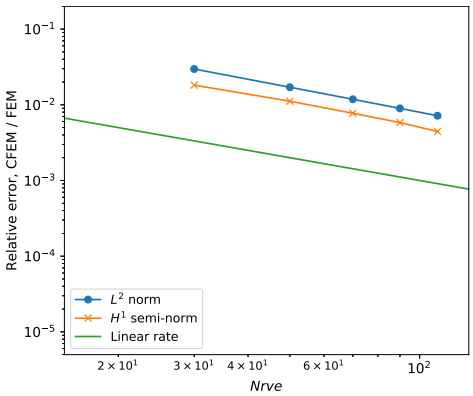

(b) Relative error for Neumann boundary value problem

Figure 2.15: Case of one square inclusion $l = 0.3$. Relative error of L^2 norm and H^1 semi-norm for a static elastic Dirichlet boundary value problem and Neumann boundary value problem in the domain Ω.

In the case of matching meshes, the PFEM will coincide with a standard Finite Element Method with conforming and compatible mesh for the inclusion. The comparison between matching and non-matching meshes allows us to measure the error made by the PFEM with a specific way that we proposed in the following:

In a fixed mesh of the domain Ω, from a matching position of two meshes, we move the square inclusion slightly in different directions (following x axis, y axis and the diagonal direction of these two axis, see Figure 2.16), until another matching position.

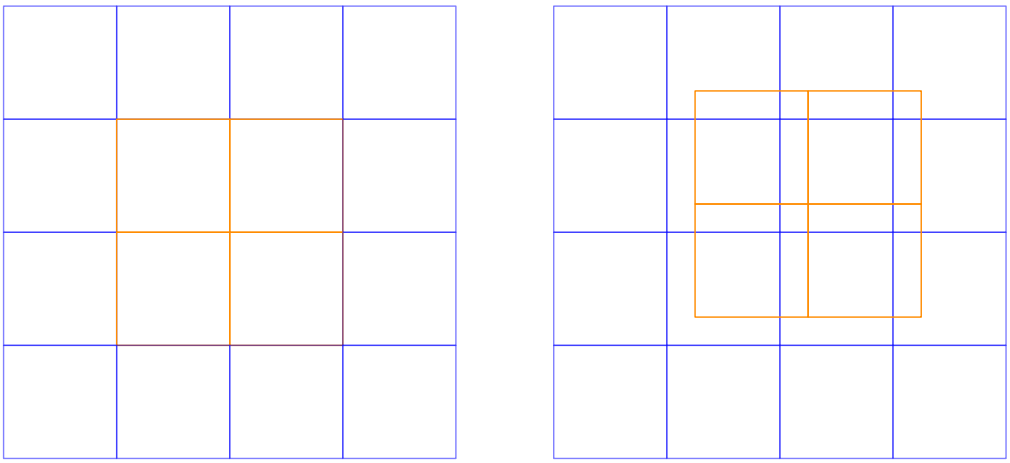

Figure 2.16: A square inclusion in a structured mesh Ω of $N_{rve} = 4$ with matching meshes (left) and non-matching meshes (right).

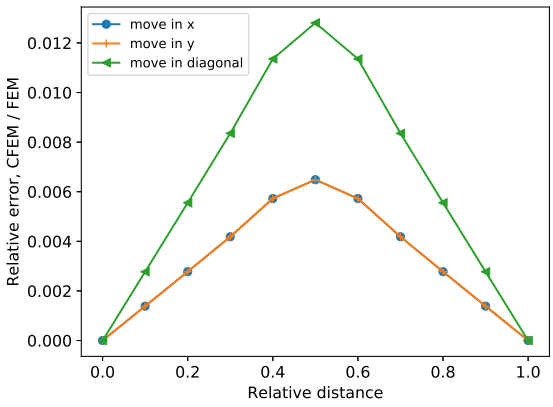

Figure 2.17: Case of one square inclusion $l = 0.3$. PFEM/FEM comparison between matching and non-matching meshes with $N_{rve} = 100$. Relative error of L^2 norm for a thermal Dirichlet boundary value problem.

In Figure 2.17, we plot the relative error of the PFEM referenced to the FEM for L^2 norm relative error in a thermal Dirichlet boundary value problem versus relative distance, which is the ratio between the moved distance and h_{rve}, the characteristic length of the mesh of the RVE. Compared to the FEM, the error made by our method is null in the matching position, and reach its maximum with a relative distance equal to 0.5. For a resolution $N_{rve} = 100$, we note that the error of the method might be significant about 1.3%.

With $N_{rve} = 20, 40, 60, 80, 100$ (Resolution multiple of 4), we are immersed in the matching meshes case. The relative error of L^2 norm and H^1 semi-norm for a thermal Dirichlet boundary value problem in such resolutions is shown

in Figure 2.18.

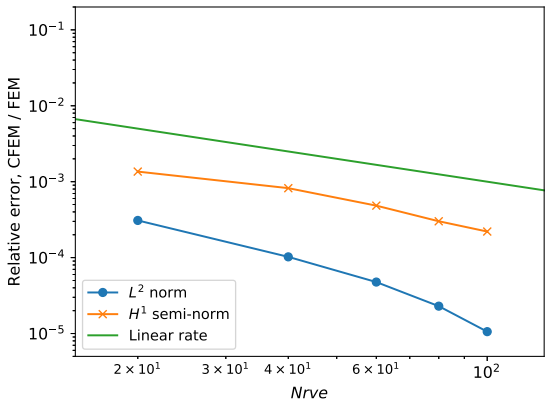

Figure 2.18: Case of one square inclusion $l = 0.3$. Relative error of L^2 norm and H^1 semi-norm for a thermal Dirichlet boundary value problem in the domain Ω with matching meshes.

Compared to the reference FEM solution, the relative error L^2 norm of temperature is in order of magnitude 10^{-5} with a resolution of $N_{rve} = 100$. Besides the convergence, we observe a noticeable difference in the order of magnitude for the relative errors between the non-matching meshes case and matching meshes case. This difference corresponds to the error made by the PFEM compared to a conformal finite element calculation.

But generally in PFEM computation, as the mesh of domain Ω and the mesh of inclusion Ω_{inc} are independent, they will not matching each other.

2.3.4 PFEM/FEM comparison

In this section, for a static thermal conductivity problem 2.1, we compare the distribution of temperature u computed by FEM and PFEM in corresponding meshes. In order to project the solution of PFEM u^{pfem} in the mesh of FEM, we construct a substitution matrix S the similar way as in PFEM approach (2.14).

For each component u_i^{fem} of $\hat{u}^{fem}$, we have $u_i^{fem} = u^{fem}(N_i)$ where N_i is a node of the FEM mesh. Let E_l, be an element of PFEM mesh in which the node N_i is included.

We define a reference element and its corresponding shape functions $\widehat{\Phi}$ for the isoparametric element E_l. Let (x_i, y_i, z_i) be the coordinates of the node N_i, and let (r_i, s_i, t_i) be its coordinates in the reference element associated to E_l. We denote S_i the $1 \times n$ line matrix (n is the total number of DOFs in PFEM

mesh) such that:

$$u_i^{fem} = u^{fem}(x_i, y_i, z_i) = \widehat{\Phi}(r_i, s_i, t_i)^\top \hat{u}^{pfem} = S_i \hat{u}^{pfem} \tag{2.32}$$

Considering every nodes of the FEM mesh, we finally obtain a substitution matrix S constructed line by line, which substitutes $\hat{u}^{fem}$, the DOFs associated to the mesh of FEM, for $\hat{u}^{pfem}$, the DOFs associated to the mesh of PFEM:

$$\hat{u}^{fem} = S\hat{u}^{pfem} \tag{2.33}$$

And then, we can calculate the relative difference of the solution between two methods in the same mesh:

$$\text{Relative difference} = \frac{|u^{fem} - Su^{pfem}|}{max(|u^{fem}|)} \tag{2.34}$$

Let's consider a domain Ω with one disk inclusion of diameter $d = 0.3$. The structured mesh of the PFEM with a resolution $N_{rve} = 60$ relates to 3721 nodes and 3600 quadratic elements. The mesh of the referenced FEM is generate by Gmsh [3], with 3692 nodes and 3631 quadratic elements.

We draw the temperature u, which is the solution of the thermal Dirichlet boundary value problem (2.1), in each nodes of the corresponding mesh for PFEM in Figure 2.19a and for FEM in Figure 2.19b. The relative difference between these two methods is plotted in Figure 2.19c. The numerical results with Neumann boundary conditions (2.24) is shown in Figure 2.20.

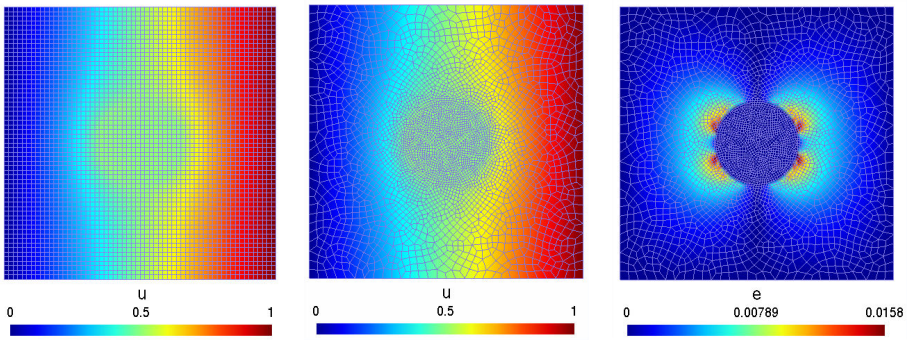

(a) PFEM solution (b) FEM solution (c) Relative difference

Figure 2.19: Case of one disk inclusion of diameter $d = 0.3$. Temperature computed by PFEM, FEM and the relative difference between them for thermal Dirichlet boundary value problem.

[3]Gmsh is a finite element mesh generator developed by Christophe Geuzaine and Jean-François Remacle. https://gmsh.info

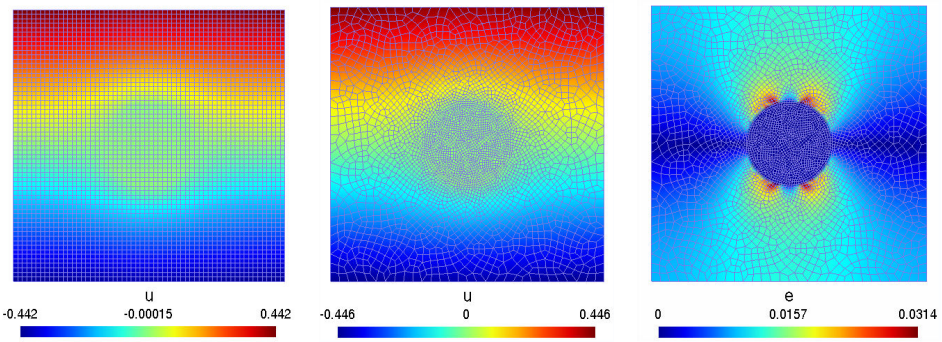

(a) PFEM solution (b) FEM solution (c) Relative difference

Figure 2.20: Case of one disk inclusion of diameter $d = 0.3$. Temperature computed by PFEM, FEM and the relative difference between them for thermal Neumann boundary value problem.

In both cases, we observe that the maximum value of the relative difference, which is in order of magnitude 10^{-2}, is located around the boundary of the inclusion. This study help us to estimate the location and the quantity of the PFEM's error referenced to the FEM.

To deal with the static linear elasticity problem 2.16, we compare the displacement, strain and Von Mises stress computed by FEM and PFEM in corresponding meshes. We keep the same meshes for FEM and PFEM as in the thermal conductivity problem. The numerical results of Dirichlet boundary value problem is presented in Figure 2.21. In Figure 2.22, we illustrate the results of Neumann boundary value problem.

We notice that, the maximum value of relative differences is always located around the interface between the matrix phase and the inclusion phase, as in the thermal cases. This is due to the fact that the weak continuity is not respected at the interface of the matrix and the inclusion.

The maximum relative difference of displacement is in order of magnitude 10^{-2}, but the maximum relative difference of strain and stress reach to $\simeq 0.5$. The Von Mises stress arise on the boundary of inclusions in PFEM computation, which is not the case in the FEM solution, see Figure 2.21g and Figure 2.22g. In other words, in strain and stress calculation, the error produced by PFEM is more significant.

Let's consider a domain Ω with one square inclusion of side length $l = 0.3$. The mesh of the PFEM is structured with a resolution $N_{rve} = 58$ which relates to 3481 nodes and 3364 quadratic elements. We note that the structured mesh is not matching with the inclusion's mesh, which is a general case for the PFEM resolution. The mesh of the referenced FEM is generate by Gmsh with 3415 nodes and 3314 quadratic elements.

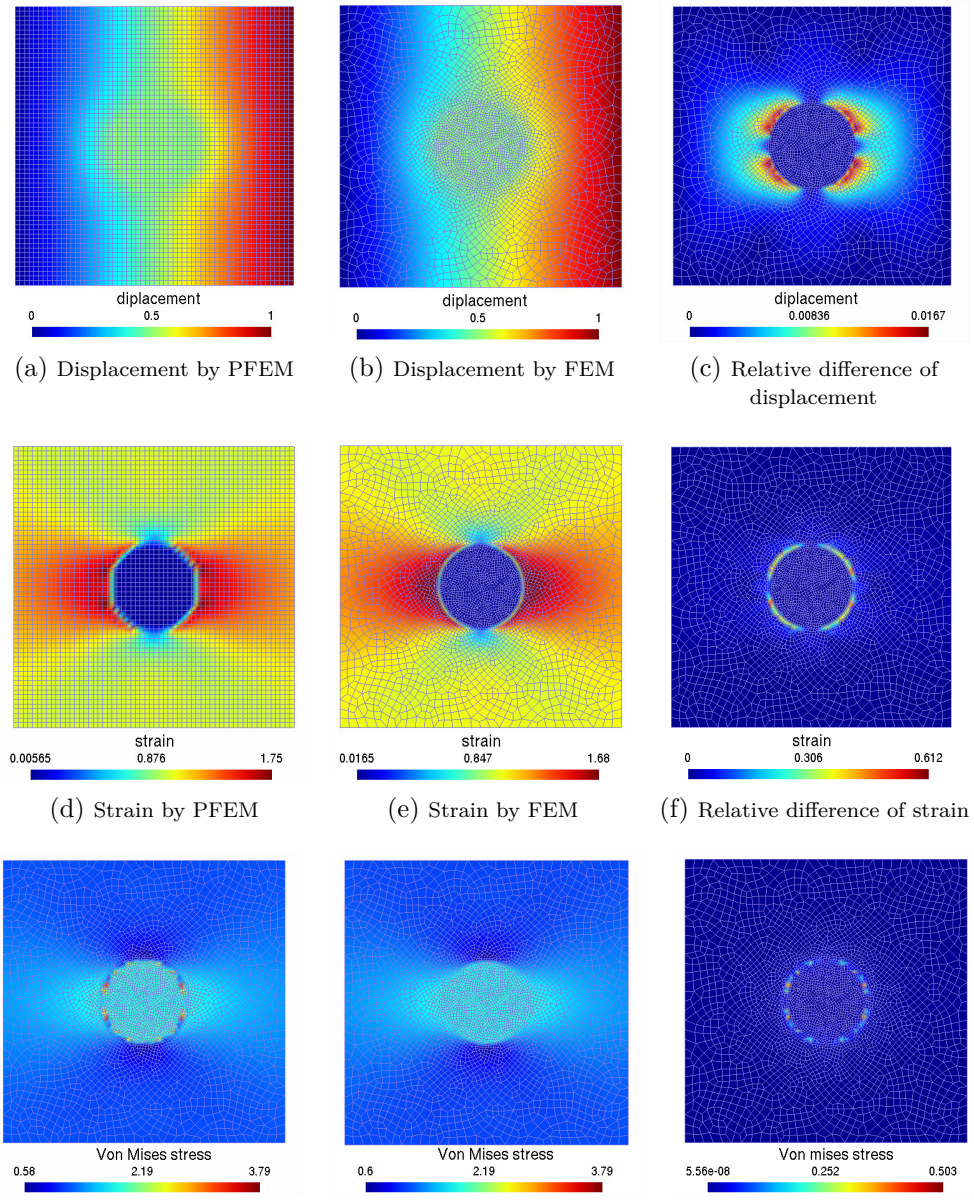

(a) Displacement by PFEM (b) Displacement by FEM (c) Relative difference of displacement

(d) Strain by PFEM (e) Strain by FEM (f) Relative difference of strain

(g) Von Mises stress by PFEM (h) Von Mises stress by FEM (i) Relative difference of Von Mises stress

Figure 2.21: Case of one disk inclusion of diameter $d = 0.3$. Displacement, strain and Von Mises stress computed by PFEM, FEM and the relative difference between them for elastic Dirichlet boundary value problem.

We have done the same studies as in the disk inclusion case. We plot the temperature computed by PFEM, FEM and the relative difference between them for thermal Dirichlet boundary value problem in Figure 2.23, for thermal Neumann boundary value problem in Figure 2.24. The displacement, strain and Von Mises stress computed by PFEM, FEM and the relative difference

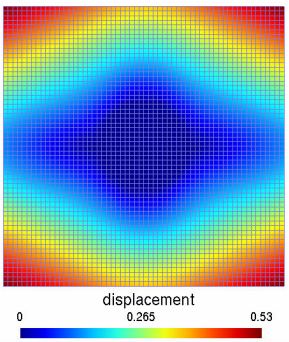

(a) Displacement by PFEM

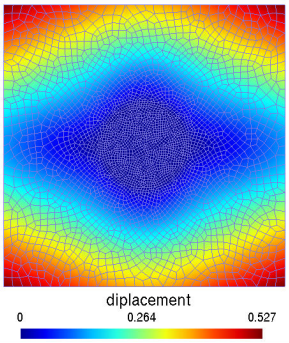

(b) Displacement by FEM

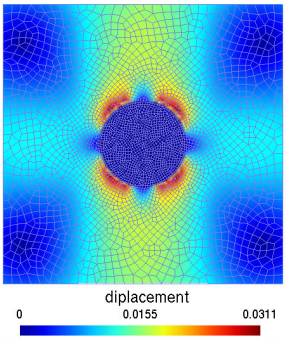

(c) Relative difference of displacement

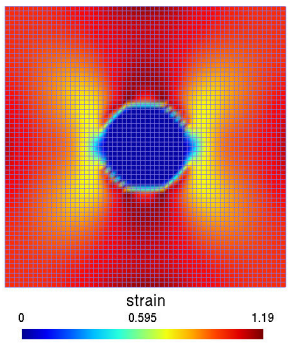

(d) Strain by PFEM

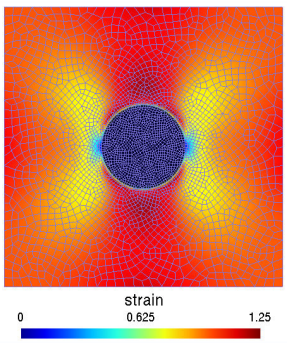

(e) Strain by FEM

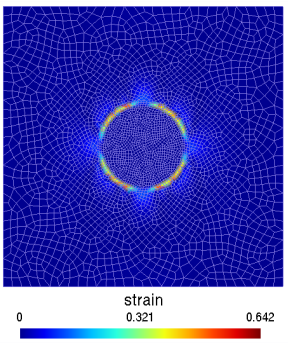

(f) Relative difference of strain

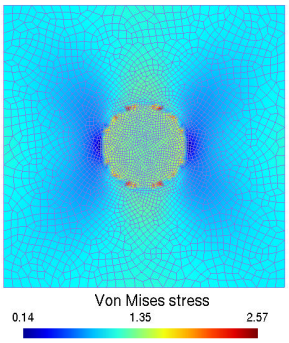

(g) Von Mises stress by PFEM

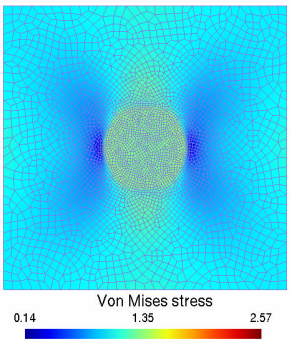

(h) Von Mises stress by FEM

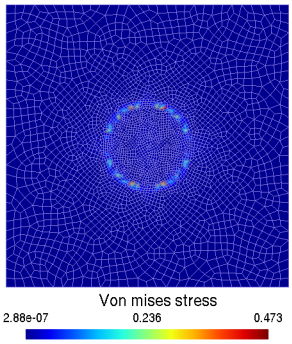

(i) Relative difference of Von Mises stress

Figure 2.22: Case of one disk inclusion of diameter $d = 0.3$. Displacement, strain and Von Mises stress computed by PFEM, FEM and the relative difference between them for elastic Neumann boundary value problem.

between them for elastic Dirichlet boundary value problem is drawn in Figure 2.25, for elastic Neumann boundary value problem is drawn in Figure 2.26.

We notice that, in case of Ω with one square inclusion, the temperature, displacement, strain and Von Mises stress solutions computed by the PFEM and the FEM are visually similar, as in the disk inclusion case. The peak value

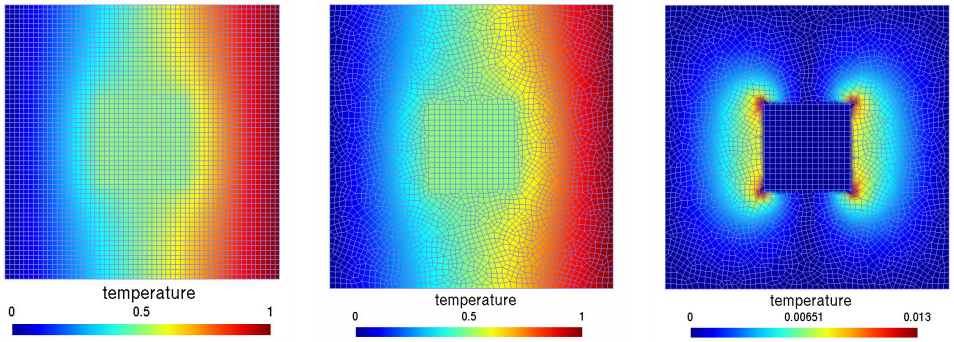

(a) PFEM solution (b) FEM solution (c) Relative difference

Figure 2.23: Case of one square inclusion of side length $l = 0.3$. Temperature computed by PFEM, FEM and the relative difference between them for thermal Dirichlet boundary value problem.

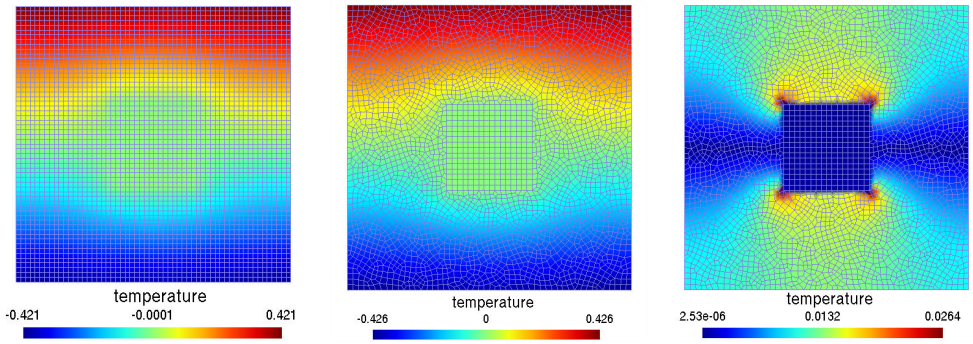

(a) PFEM solution (b) FEM solution (c) Relative difference

Figure 2.24: Case of one square inclusion of side length $l = 0.3$. Temperature computed by PFEM, FEM and the relative difference between them for thermal Neumann boundary value problem.

of relative difference is located around the four corners of the square inclusion, which could reach to $\simeq 0.02$ for the temperature and displacement; and reach to $\simeq 0.2$ for the strain and Von Mises stress. With this study, we are able to locate the error made by PFEM for a square inclusion.

In order to evaluate the PFEM solution for several inclusions case, let's consider two disk inclusions with diameter $d = 0.3$. We draw in Figure 2.27, the temperature computed by PFEM, FEM and the relative difference between them for thermal Dirichlet boundary value problem. While the displacement and strain computed these two methods for elastic Dirichlet boundary value problem are plotted in Figure 2.28. The referenced FEM solution is computed by a conformal mesh with 3658 nodes and 3607 quadratic elements. The contrast remains fixed at $c_{elastic} = 100$.

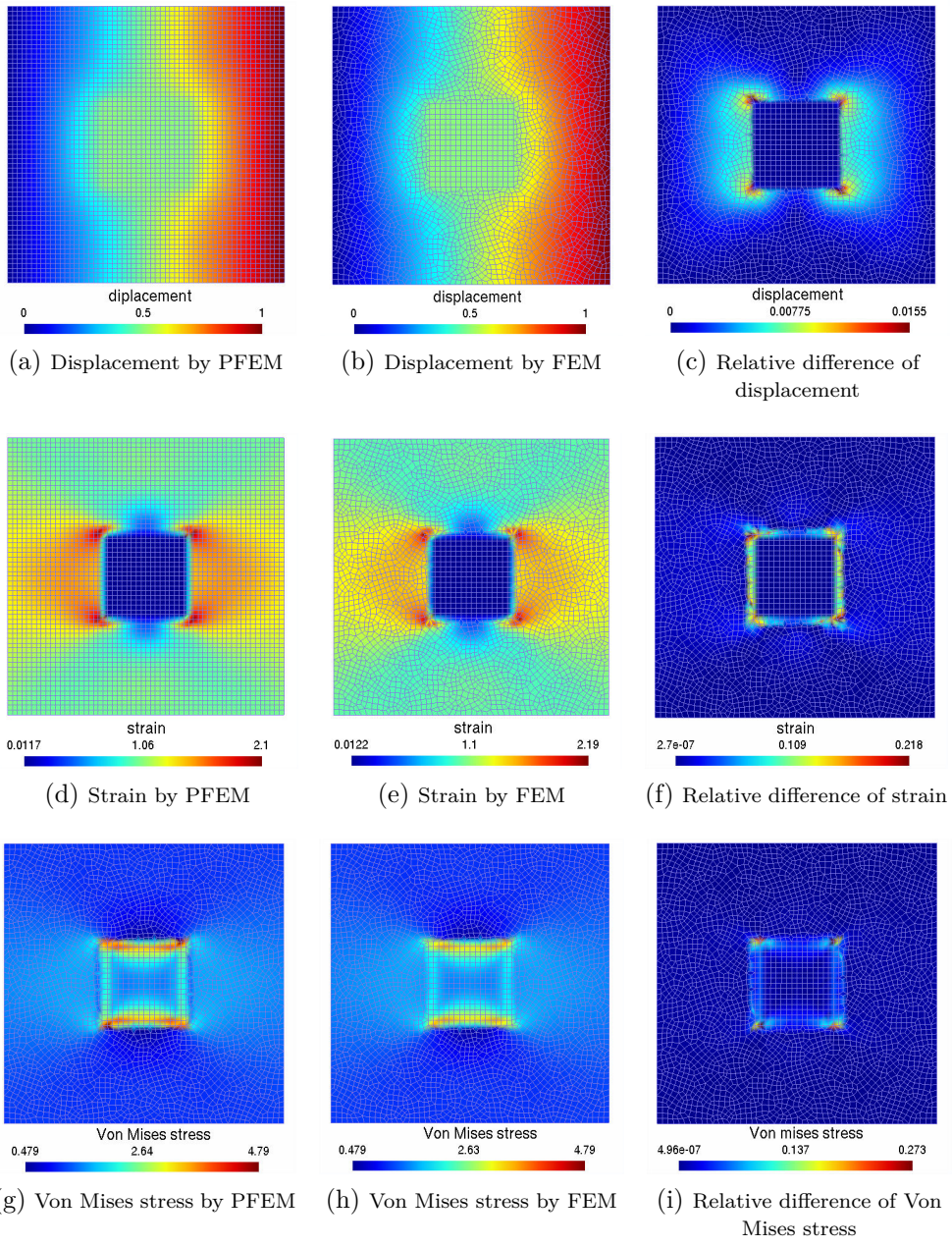

(a) Displacement by PFEM (b) Displacement by FEM (c) Relative difference of displacement

(d) Strain by PFEM (e) Strain by FEM (f) Relative difference of strain

(g) Von Mises stress by PFEM (h) Von Mises stress by FEM (i) Relative difference of Von Mises stress

Figure 2.25: Case of one square inclusion of side length $l = 0.3$. Displacement, strain and Von Mises stress computed by PFEM, FEM and the relative difference between them for elastic Dirichlet boundary value problem.

The same behavior has been observed as in the one inclusion case. The error produced by PFEM is always located in the interface between matrix phase and inclusion phase. Compared to the referenced FEM solutions, the maximum value of the relative difference of temperature and displacement are in order of magnitude 10^{-2}. However, the relative difference of strain reach to

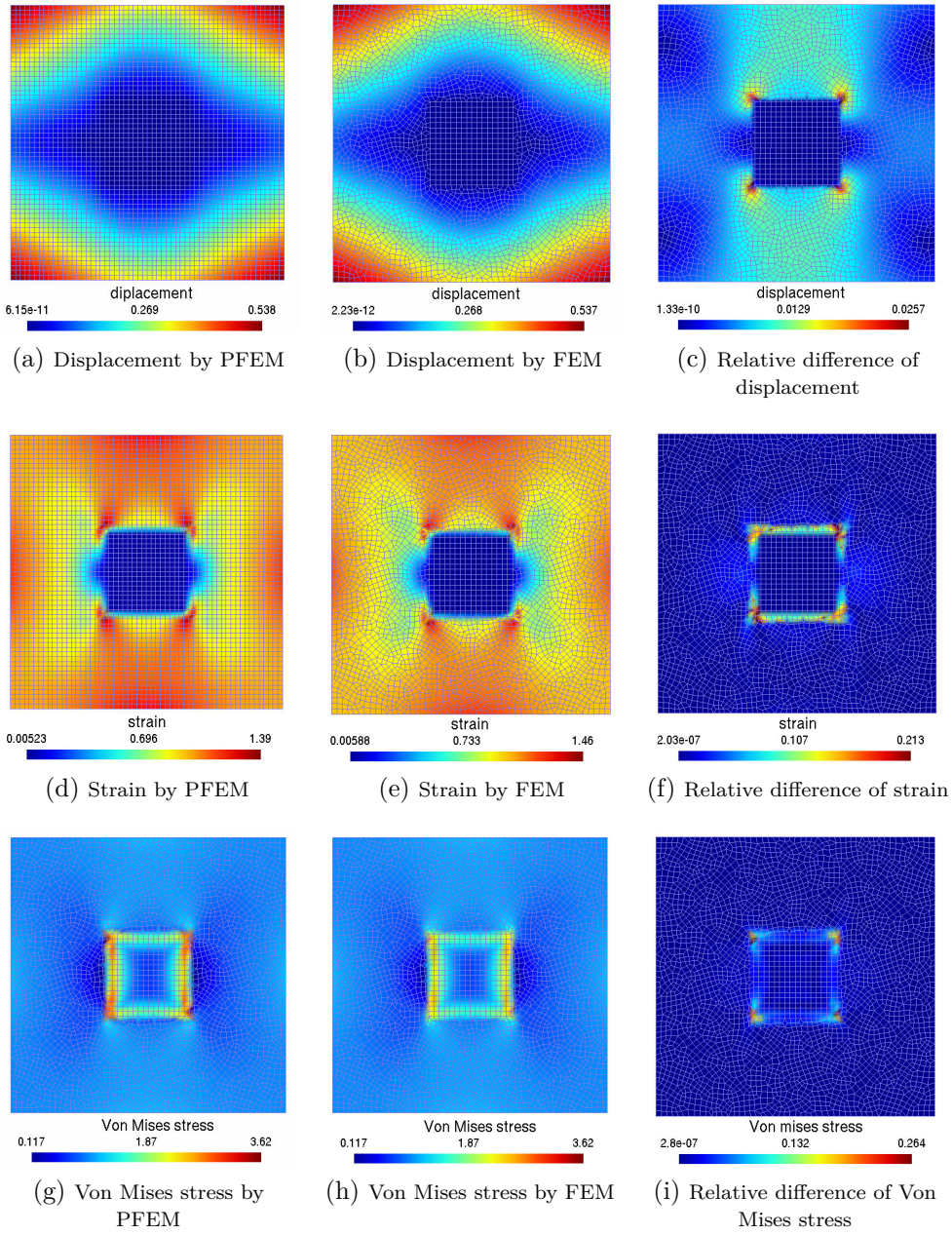

(a) Displacement by PFEM (b) Displacement by FEM (c) Relative difference of displacement

(d) Strain by PFEM (e) Strain by FEM (f) Relative difference of strain

(g) Von Mises stress by PFEM (h) Von Mises stress by FEM (i) Relative difference of Von Mises stress

Figure 2.26: Case of one square inclusion of side length $l = 0.3$. Displacement, strain and Von Mises stress computed by PFEM, FEM and the relative difference between them for elastic Neumann boundary value problem.

$\simeq 0.63$.

In a specific case that inclusions situated very close to each other, the structured mesh may not be fine enough to separate these independent meshes of each inclusion, see Figure 2.29. With $N_{rve} = 80$, the nearest boundary nodes of two disk inclusions are treated by one element of structured mesh Ω. While

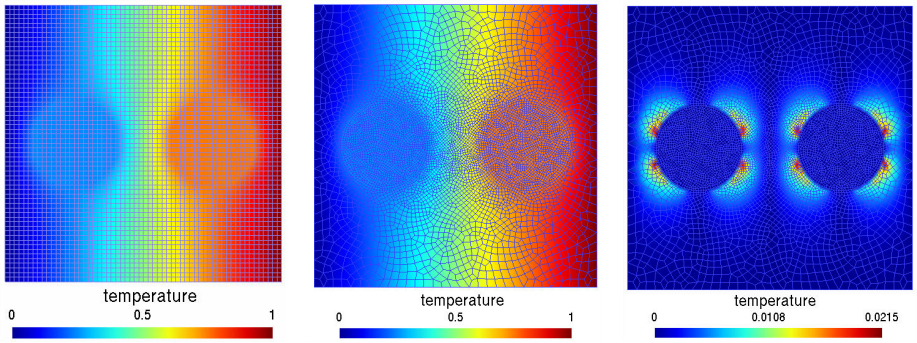

(a) Temperature by PFEM (b) Temperature by FEM (c) Relative difference of temperature

Figure 2.27: Case of two disk inclusions of diameter $d = 0.3$. Temperature computed by PFEM, FEM and the relative difference between them for thermal Dirichlet boundary value problem.

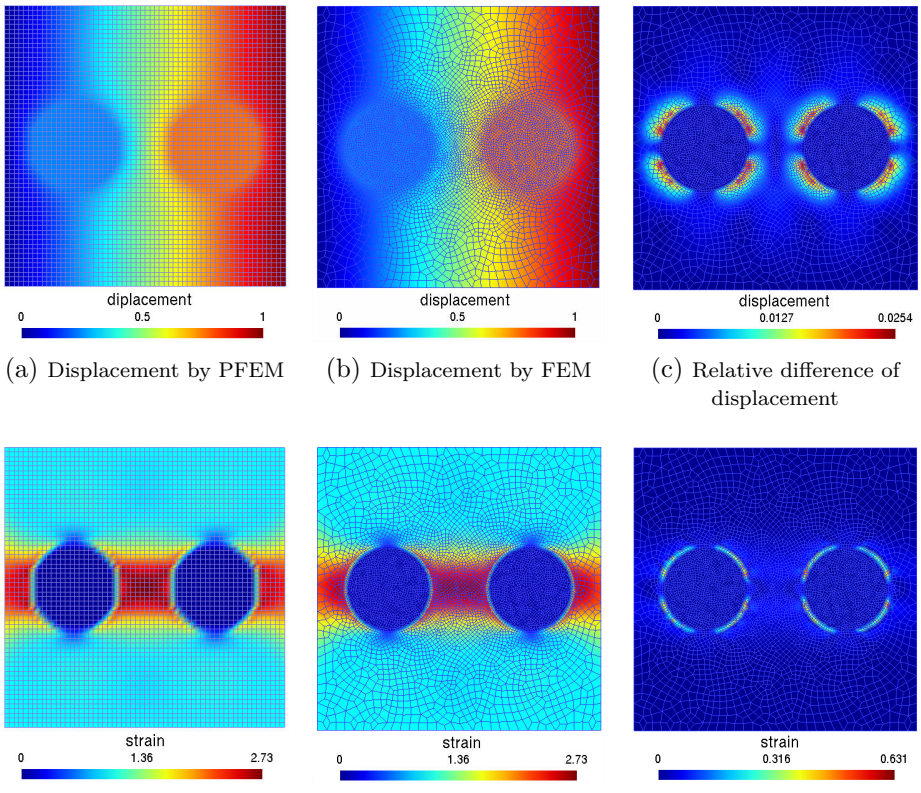

(a) Displacement by PFEM (b) Displacement by FEM (c) Relative difference of displacement

(d) Strain by PFEM (e) Strain by FEM (f) Relative difference of strain

Figure 2.28: Case of two disk inclusions of diameter $d = 0.3$. Displacement and strain computed by PFEM, FEM and the relative difference between them for elastic Dirichlet boundary value problem.

in the case of $N_{rve} = 160$, all the boundary nodes of disk inclusion's meshes could be treated independently.

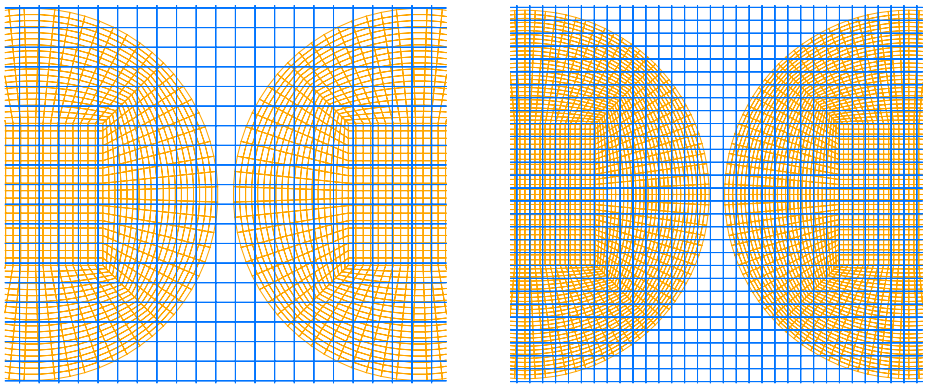

(a) $N_{rve} = 80$ (b) $N_{rve} = 160$

Figure 2.29: Independents meshes of disk inclusions (yellow) in structured mesh of domain Ω (blue) with $N_{rve} = 80, 160$.

We draw, in Figure 2.30, the strain solution computed by PFEM, FEM and the relative difference between them for an elastic Dirichlet boundary value problem with 4 disk inclusions lain in one direction.

We observe that, in FEM solution, the strain in each disk inclusion is rigid, the peak value of strain is situated between each inclusion. The same observation can be found for PFEM solution with $N_{rve} = 240$. While in PFEM solution with $N_{rve} = 80$, we note that the area closest to each inclusion seems to be rigid as well. This is due to the fact that, if the structured mesh Ω is not fine enough to isolate two disk inclusions, a numerical percolation phenomenon appears in the PFEM computation with low resolution. The percolation area is located particularly between each inclusions.

Conclusion

In this chapter, we have presented an original method named Phantom domain Finite Element Method (PFEM) to solve a steady model problem such as thermal boundary value problem and elastic boundary value problem for heterogeneous materials. The principle of PFEM is the same as Fictitious domain method. Using distinct meshes of inclusions Ω_{inc} and the domain Ω, as shown in Figure 2.31, we are able to implement a finite element in the framework of a structured mesh Ω with the help of a substitution matrix.

Numerical experiments, with inclusions of elementary geometry such as disk and square, have shown a linear convergence of relative errors with respect to

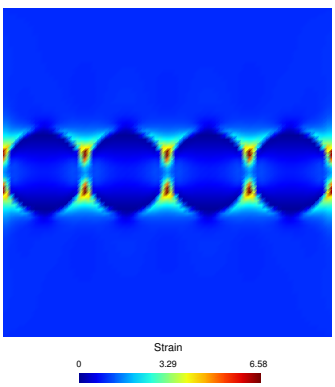

(a) PFEM strain solution with $N_{rve} = 80$

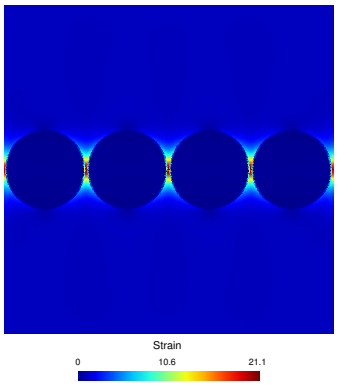

(b) Reference FEM strain solution

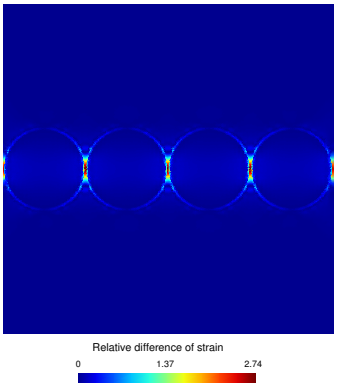

(c) Relative difference of strain PFEM 80 / FEM

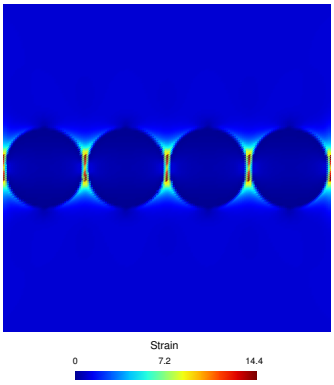

(d) PFEM strain solution with $N_{rve} = 160$

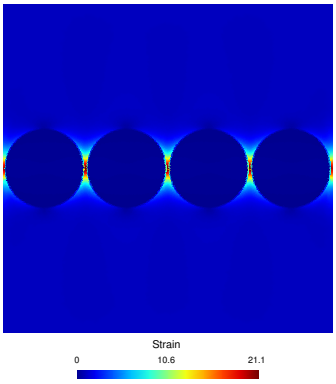

(e) Reference FEM strain solution

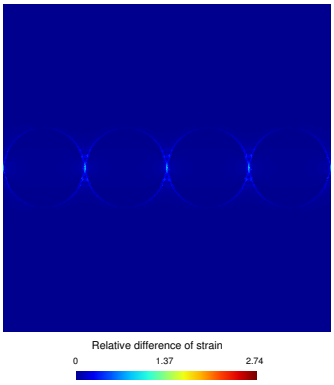

(f) Relative difference of strain PFEM 160 / FEM

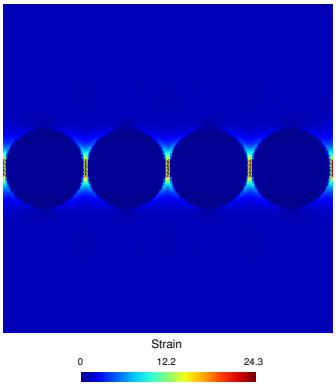

(g) PFEM strain solution with $N_{rve} = 240$

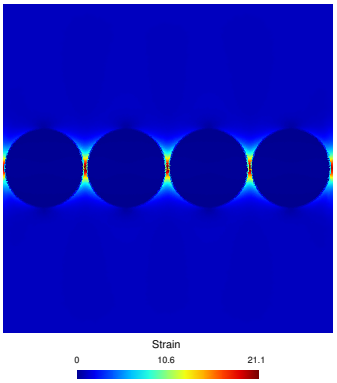

(h) Reference FEM strain solution

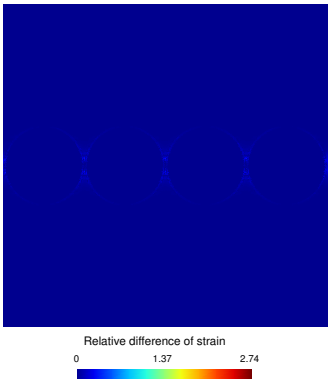

(i) Relative difference of strain PFEM 240 / FEM

Figure 2.30: Case of 4 disk inclusions of diameter $d = 0.24$. Strain computed by PFEM and FEM for elastic Dirichlet boundary problem.

referenced FEM solutions. The convergence rates are observed as expected, regarding the use of linear interpolation. By comparing the solution computed

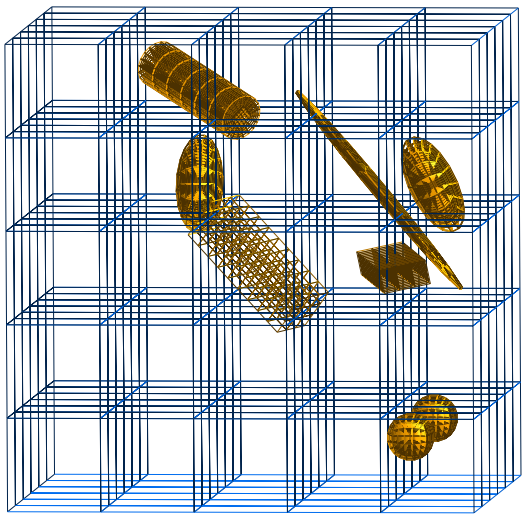

Figure 2.31: PFEM meshes: one structured mesh of the domain Ω in blue and independent meshes of each inclusion Ω_{inc} in yellow.

by PFEM and FEM in the same mesh, we are able to estimate the error produced by PFEM, which is located around the interface between the matrix and the inclusion, due to the fact that the weak continuity is not respected.

Furthermore, a numerical percolation phenomenon is observed in case that inclusions situated very close to each other.

Chapter 3

Phantom Domain Finite Element Method For Numerical Homogenization

Contents

Introduction

In the chapter 2, we have presented the Phantom domain Finite Element Method (PFEM) for a standard boundary value problem. Our first aim was to deal with the homogenization, which means the computation of effective properties of composite materials in cases where the meshing is difficult. We consider both thermal and elasticity cases.

Effective properties are usually calculated on a Representative Volume Element (RVE), as it has been presented in section 1.3.1; for the sake of simplicity, we only consider elementary RVEs such as $\Omega = [0,1]^2$ or $\Omega = [0,1]^3$, for which the definition of a structured mesh is easy and does not need a special algorithm.

We consider three type of boundary conditions, two of them were recalled in section 1.3.2 and section 1.3.3 : pure Dirichlet conditions, pure Neumann conditions, plus periodic conditions. This chapter is devoted to calculate the effective properties of a composite material as a straight application of previous method presented in chapter 2 associated with the corresponding boundary conditions.

3.1 Effective properties determination with Kinematic Uniform Boundary Conditions

- Thermal conductivity problem

In a thermal conductivity problem, the Kinematic Uniform Boundary Conditions (KUBC) is defined as the pure Dirichlet boundary value problem :

$$\begin{cases} div\ \mathbf{q} = 0 & \text{in } \Omega \\ u = \mathbf{g}.\mathbf{x} & \text{on } \partial\Omega \end{cases} \tag{3.1}$$

where $\mathbf{g}$ is a constant vector. In section 1.3.2, it has been established that:

$$\frac{1}{|\Omega|}\int_\Omega \Lambda\nabla u = \Lambda^{kubc}\mathbf{g} \tag{3.2}$$

The vector $\mathbf{g}$ is chosen such a manner it spans the canonical basis of $\mathbb{R}^3$ so that the effective property Λ^{kubc} is obtain, column by column.

To apply the Phantom domain Finite Element Method (PFEM), from the problem (3.2), let us consider the energy functional : for any temperature u,

$$J(u) = \int_\Omega (\Lambda\nabla u).\nabla u \tag{3.3}$$

As before, we suppose the domain Ω to be constituted by two homogeneous and isotropic media : the matrix $\Omega \setminus \Omega_{inc}$ and the inclusion Ω_{inc}. The conductivity matrix writes:

$$\Lambda = \begin{cases} \Lambda_{mat} & in\ \Omega \backslash \Omega_{inc} \\ \Lambda_{inc} & in\ \Omega_{inc} \end{cases}$$

The energy form is split as follows:

$$J(u) = \int_{\Omega \backslash \Omega_{inc}} (\Lambda_{mat} \nabla u).\nabla u + \int_{\Omega_{inc}} (\Lambda_{inc} \nabla u).\nabla u \tag{3.4}$$

A classical Finite Element Method would employ a conforming mesh matching the matrix $\Omega \backslash \Omega_{inc}$ and the inclusion Ω_{inc} to calculate the integral in (3.4) in an interpolation space associated to the mesh.

We emphasize that, PFEM consists in using two distinct and independent meshes representing the whole domain Ω and the inclusion Ω_{inc} instead of a unique conformal mesh matching the geometry of the inclusion.

From (3.4), the energy functional reads :

$$J(u) = \underbrace{\int_{\Omega} (\Lambda_{mat} \nabla u).\nabla u}_{J_{mat}} + \underbrace{\int_{\Omega_{inc}} \left((\Lambda_{inc} - \Lambda_{mat}) \nabla u\right).\nabla u}_{J_{inc}} \tag{3.5}$$

The functional J is then split into two integrals J_{mat} and J_{inc} respectively defined on the whole domain Ω and the inclusion Ω_{inc}.

This allows independent numerical computations of J_{mat} and J_{inc} : Associated to the structured mesh of the entire domain Ω, let us define an interpolation space V^h of finite dimension n such that any $u^h \in V^h$ can be represented by $\hat{u} \in \mathbb{R}^n$. The functional J_{mat} can then be calculated in V^h with the help of a $n \times n$ matrix K_{mat} :

$$J_{mat}(u^h) = \int_{\Omega} (\Lambda_{mat} \nabla u^h).\nabla u^h = \hat{u}^\top K_{mat} \hat{u}, \quad \forall u^h \in V^h \tag{3.6}$$

On another hand, let us consider a conforming mesh of the inclusion Ω_{inc} independent of the mesh defining Ω. We define the interpolation space W^l of finite dimension p, associated to the inclusion mesh so that any $v^l \in W^l$ can be represented by a vector $\hat{v} \in \mathbb{R}^p$. The functional J_{inc} can be defined in W^l with a $p \times p$ matrix K_{inc} :

$$J_{inc}(v^l) = \int_{\Omega_{inc}} \left((\Lambda_{inc} - \Lambda_{mat}) \nabla v^l\right).\nabla v^l = \hat{v}^\top K_{inc} \hat{v}, \quad \forall v^l \in W^l \tag{3.7}$$

Both the matrices K_{mat} and K_{inc} can be computed using standard finite element procedures. By defining these two matrices, we compute separately the energy forms J_{mat} and J_{inc}.

To relate the DOFs $\hat{v}$ defined on the inclusion Ω_{inc} to the DOFs $\hat{u}$ defined on the structured mesh Ω, we define a substitution matrix S, as in the steady model problem case (2.14):

$$\hat{v} = S\hat{u}$$

The energy form computed on the inclusion J_s becomes:

$$\begin{aligned} J_s &= \hat{v}^\top K_{inc} \hat{v} \\ &= (S\hat{u})^\top K_{inc} S\hat{u} \end{aligned} \tag{3.8}$$

Finally, we obtain the main energy form defined only on $\hat{u}$:

$$J(u^h) = \hat{u}^\top \left[K_{mat} + S^\top K_{inc} S \right] \hat{u} \tag{3.9}$$

- Linear elasticity problem

In a linear elasticity problem, the Kinematic Uniform Boundary Conditions (KUBC) is defined as the pure Dirichlet boundary value problem :

$$\begin{cases} div\ \overline{\sigma} = 0 & \text{in } \Omega \\ \mathbf{u} = \overline{E}\,\mathbf{x} & \text{on } \partial\Omega \end{cases} \tag{3.10}$$

where $\overline{E}$ is a symmetrical tensor that does not depend on $\mathbf{x}$. In section 1.3.2, it has been proved that:

$$\frac{1}{|\Omega|} \int_\Omega \mathbb{C}\,\overline{e}(\mathbf{u}) = \mathbb{C}^{kubc}\,\overline{E} \tag{3.11}$$

where $\overline{e}(\mathbf{u})$ is the linearized deformation tensor associated to the displacement $\mathbf{u}$. The tensor $\overline{E}$ is chosen such a manner it spans the six vectors of the basis of Voight to obtain the effective property $\mathbb{C}^{kubc}$, column by column.

The extension of the PFEM to linear elasticity problem is straightforward. The problem (3.11) involves a deformation energy form : for any displacement $\mathbf{u}$,

$$J(\mathbf{u}) = \int_\Omega (\mathbb{C}\,\overline{e}(\mathbf{u})) : \overline{e}(\mathbf{u}) \tag{3.12}$$

where $\mathbb{C}$ is the second order elasticity tensor defining the constitutive law of the material :

$$\mathbb{C} = \begin{cases} \mathbb{C}_{mat} & in\ \Omega \backslash \Omega_{inc} \\ \mathbb{C}_{inc} & in\ \Omega_{inc} \end{cases}$$

As in the thermal case the energy form is devided in two parts as follows :

$$J(\mathbf{u}) = \underbrace{\int_\Omega (\mathbb{C}_{mat}\,\overline{e}(\mathbf{u})) : \overline{e}(\mathbf{u})}_{J_{mat}} + \underbrace{\int_{\Omega_{inc}} ((\mathbb{C}_{inc} - \mathbb{C}_{mat})\,\overline{e}(\mathbf{u})) : \overline{e}(\mathbf{u})}_{J_{inc}} \tag{3.13}$$

Considering two interpolation spaces $\mathbf{u}^h \in \mathbf{V}^h$ and $\mathbf{v}^l \in \mathbf{W}^l$, we define the $n \times n$ and $p \times p$ matrices K_{mat} and K_{inc}:

$$J_{mat}(\mathbf{u}^h) = \int_\Omega \left(\mathbb{C}_{mat}\,\overline{e}(\mathbf{u}^h)\right) : \overline{e}(\mathbf{u}^h) = \hat{\mathbf{u}}^\top K_{mat}\hat{\mathbf{u}}, \quad \forall \mathbf{u}^h \in \mathbf{V}^h \tag{3.14}$$

$$J_{inc}(\mathbf{v}^l) = \int_{\Omega_{inc}} \left((\mathbb{C}_{inc} - \mathbb{C}_{mat})\,\overline{e}(\mathbf{v}^l)\right) : \overline{e}(\mathbf{v}^l) = \hat{\mathbf{v}}^\top K_{inc}\hat{\mathbf{v}}, \quad \forall \mathbf{v}^l \in \mathbf{W}^l \tag{3.15}$$

With the help of a substitution matrix S, which is similar to the thermal case but for all the components of the displacement, the main energy form reads :

$$J(\mathbf{u}^h) = \hat{\mathbf{u}}^\top \left[K_{mat} + S^\top K_{inc} S\right] \hat{\mathbf{u}} \tag{3.16}$$

3.2 Effective properties determination with Static Uniform Boundary Conditions

- Thermal conductivity problem

In a thermal conductivity problem, the Static Uniform Boundary Conditions (SUBC) method is defined as solving the pure Neumann boundary value problem :

$$\begin{cases} div\ \mathbf{q} = 0 & \text{in } \Omega \\ \mathbf{q}.\mathbf{n} = \mathbf{Q}.\mathbf{n} & \text{on } \partial\Omega \end{cases} \tag{3.17}$$

where $\mathbf{Q}$ is a constant vector. From the demonstration presented in section 1.3.2, it has been proved that:

$$\frac{1}{|\Omega|}\Lambda^{subc}\int_\Omega \nabla u = \mathbf{Q} \tag{3.18}$$

The vector $\mathbf{Q}$ is chosen such a manner it spans three vectors of the canonical basis of $\mathbb{R}^3$ to obtain column by column, the inverse of the effective property Λ^{subc}.

To apply the PFEM, from the problem (3.18), let us consider the energy functional : for any temperature u,

$$J(u) = \int_\Omega \nabla u.\nabla u \tag{3.19}$$

As before, we rewrite:

$$J(u) = \underbrace{\int_\Omega \nabla u.\nabla u}_{J_{mat}} + \underbrace{\int_{\Omega_{inc}} \nabla u.\nabla u}_{J_{inc}} \tag{3.20}$$

Considering the same interpolation spaces V^h and W^l as in the KUBC case, we define the $n \times n$ and $p \times p$ matrices K_{mat} and K_{inc}:

$$J_{mat}(u^h) = \int_\Omega \nabla u^h . \nabla u^h = \hat{u}^\top K_{mat} \hat{u}, \quad \forall u^h \in V^h \tag{3.21}$$

$$J_{inc}(v^l) = \int_{\Omega_{inc}} \nabla v^l . \nabla v^l = \hat{v}^\top K_{inc} \hat{v}, \quad \forall v^l \in W^l \tag{3.22}$$

By defining a substitution matrix S (2.14), we have the main energy form:

$$J(u^h) = \hat{u}^\top \left[K_{mat} + S^\top K_{inc} S \right] \hat{u} \tag{3.23}$$

- Linear elasticity problem

In a linear elasticity problem, the Static Uniform Boundary Conditions (SUBC) method is defined as solving the pure Neumann boundary value problem :

$$\begin{cases} div\ \overline{\sigma} = 0 & \text{in } \Omega \\ \overline{\sigma}\,\mathbf{n} = \overline{\Sigma}\,\mathbf{n} & \text{on } \partial\Omega \end{cases} \tag{3.24}$$

where $\mathbf{n}$ denotes outward pointing unit normal to $\partial\Omega$ at $\mathbf{x}$, $\overline{\Sigma}$ is a second-rank tensor independent of $\mathbf{x}$. From the demonstration presented in section 1.3.2, we prove that :

$$\frac{1}{|\Omega|} \mathbb{C}^{subc} \int_\Omega \overline{e}(\mathbf{u}) = \overline{\Sigma} \tag{3.25}$$

The tensor $\overline{\Sigma}$ is chosen such a manner it spans the six vectors of the basis of Voight to obtain the effective property $\mathbb{C}^{subc}$, column by column.

To apply the PFEM, from the problem (3.25), let us consider the energy form : for any displacement $\mathbf{u}$,

$$J(\mathbf{u}) = \int_\Omega \overline{e}(\mathbf{u}) : \overline{e}(\mathbf{u}) \tag{3.26}$$

As before, we rewrite:

$$J(\mathbf{u}) = \underbrace{\int_\Omega \overline{e}(\mathbf{u}) : \overline{e}(\mathbf{u})}_{J_{mat}} + \underbrace{\int_{\Omega_{inc}} \overline{e}(\mathbf{u}) : \overline{e}(\mathbf{u})}_{J_{inc}} \tag{3.27}$$

Considering the same interpolation spaces $\mathbf{V}^h$ and $\mathbf{W}^l$ as in the KUBC case, we define the $n \times n$ and $p \times p$ matrices K_{mat} and K_{inc} :

$$J_{mat}(\mathbf{u}^h) = \int_\Omega \overline{e}(\mathbf{u}^h) : \overline{e}(\mathbf{u}^h) = \hat{\mathbf{u}}^\top K_{mat} \hat{\mathbf{u}}, \quad \forall \mathbf{u}^h \in \mathbf{V}^h \tag{3.28}$$

$$J_{inc}(\mathbf{v}^l) = \int_{\Omega_{inc}} \overline{e}(\mathbf{v}^l) : \overline{e}(\mathbf{v}^l) = \hat{\mathbf{v}}^\top K_{inc} \hat{\mathbf{v}}, \quad \forall \mathbf{v}^l \in \mathbf{W}^l \tag{3.29}$$

Finally, we have the main energy form by defining a substitution matrix S :

$$J(\mathbf{u}^h) = \hat{\mathbf{u}}^\top \left[K_{mat} + S^\top K_{inc} S \right] \hat{\mathbf{u}} \tag{3.30}$$

3.3 Homogenization with Periodic Boundary Conditions

In the case of periodic conditions, we can assume that the considered RVE is the period of the composite material. With this condition, we obtain the homogenized conductivity tensor.

The case of periodic condition is a case for which the meshing procedure can be very complex. It is thus a case of particular interest.

We recalled the periodic homogenization theory and its numerical implementation with the finite element method in section 1.3.3. To summarize, we consider a εP periodic material. P constitutes the Representative Volume Element (RVE), ε denotes the characteristic length of the RVE. The multiscale modeling consider macroscopic space variables $\mathbf{x}$ and local space variables $\mathbf{y}$.

- Thermal conductivity problem

Under the action of external heat source f, the thermal equilibrium writes:

$$div\ \mathbf{q} + f = 0 \quad \text{in } P \tag{3.31}$$

Writing the asymptotic expansion of the heat flow $\mathbf{q}$ in the equilibrium equation, (3.31) gives by identification a local equation, which writes :

$$div_y(\mathbf{q}^0) = 0 \quad \text{in } P \tag{3.32}$$

The weak or variational form of (3.32) leads to:

$$\begin{cases} \forall u^* \in H^1_{per}(P), \\ \displaystyle\int_P \mathbf{q}^0 \nabla_y(u^*) = 0 \end{cases} \tag{3.33}$$

where $H^1_{per}(P)$ is the P-periodic Sobolev space H^1 .

Let $\mathbf{E}^0 = \nabla_x u^0$, averaging $\mathbf{q}^0$ on the RVE P, with (3.33), we have the variational problem:

$$\begin{cases} \forall u^* \in H^1_{per}(P),\ \forall \mathbf{E}^* \in \mathbb{R}^3, \\ \displaystyle\int_P \Lambda(\mathbf{E}^0 + \nabla_y u^1).(\mathbf{E}^* + \nabla_y u^*) = \Lambda^{hom}\mathbf{E}^0.\mathbf{E}^* \end{cases} \tag{3.34}$$

where Λ^{hom} denotes the homogenized conductivity tensor calculated with periodic condition.

The resolution of the three problems (3.34) as $\Lambda^{hom}\mathbf{E}^0$ spans $\mathbb{R}^3$, gives the homogenized conductivity tensor Λ^{hom}.

To apply the PFEM, from the variational problem (3.34), let us consider the quadratic energy functional:

$$J(u, \mathbf{E}) = \int_P \Lambda(\mathbf{E} + \nabla_y u).(\mathbf{E} + \nabla_y u) \tag{3.35}$$

Let the RVE P be constituted by two homogeneous and isotropic media : the matrix $P \setminus P_{inc}$ and one inclusion P_{inc} :

$$J(u, \mathbf{E}) = \int_{P \setminus P_{inc}} \Lambda_{mat}(\mathbf{E} + \nabla_y u).(\mathbf{E} + \nabla_y u) + \int_{P_{inc}} \Lambda_{inc}(\mathbf{E} + \nabla_y u).(\mathbf{E} + \nabla_y u) \tag{3.36}$$

The energy form can be rewritten as follows:

$$J(u, \mathbf{E}) = \underbrace{\int_P \Lambda_{mat}(\mathbf{E} + \nabla_y u).(\mathbf{E} + \nabla_y u)}_{J_{mat}} + \underbrace{\int_{P_{inc}} (\Lambda_{inc} - \Lambda_{mat})(\mathbf{E} + \nabla_y u).(\mathbf{E} + \nabla_y u)}_{J_{inc}} \tag{3.37}$$

Associated to the structured mesh of the entire domain P, let us define an interpolation space V^h of finite dimension n such that any displacement $u^h \in V^h$ can be represented by $\hat{u} \in \mathbb{R}^n$. On another hand, let us define the interpolation space W^l of finite dimension p, associated to the inclusion mesh so that any displacement $v^l \in W^l$ can be represented by a vector $\hat{v} \in \mathbb{R}^p$.

We define the matrix K_{mat} of dimension $(n+2) \times (n+2)$ in 2D, $(n+3) \times (n+3)$ in 3D, and the matrix K_{inc} of dimension $(p+2) \times (p+2)$ in 2D, $(p+3) \times (p+3)$ in 3D :

$$\begin{aligned} J_{mat}(u^h, \mathbf{E}) &= \int_P \Lambda_{mat}(\mathbf{E} + \nabla_y u^h).(\mathbf{E} + \nabla_y u^h) \\ &= \begin{bmatrix} \hat{u} \\ \mathbf{E} \end{bmatrix}^\top K_{mat} \begin{bmatrix} \hat{u} \\ \mathbf{E} \end{bmatrix}, \quad \forall u^h \in V^h \end{aligned} \tag{3.38}$$

$$\begin{aligned} J_{inc}(v^l, \mathbf{E}) &= \int_{P_{inc}} (\Lambda_{inc} - \Lambda_{mat})(\mathbf{E} + \nabla_y v^l).(\mathbf{E} + \nabla_y v^l) \\ &= \begin{bmatrix} \hat{v} \\ \mathbf{E} \end{bmatrix}^\top K_{inc} \begin{bmatrix} \hat{v} \\ \mathbf{E} \end{bmatrix}, \quad \forall v^l \in W^l \end{aligned} \tag{3.39}$$

Considering the same substitution matrix as in (2.14), we have :

$$J_{inc} = \begin{bmatrix} \hat{v} \\ \mathbf{E} \end{bmatrix}^\top K_{inc} \begin{bmatrix} \hat{v} \\ \mathbf{E} \end{bmatrix} = \begin{bmatrix} S\hat{u} \\ \mathbf{E} \end{bmatrix}^\top K_{inc} \begin{bmatrix} S\hat{u} \\ \mathbf{E} \end{bmatrix}, \quad \forall u^h \in V^h \tag{3.40}$$

Finally, we obtain the main energy quadratic form defined only on $\hat{u}$:

$$J(u^h, \mathbf{E}) = \begin{bmatrix} \hat{u} \\ \mathbf{E} \end{bmatrix}^\top \left(K_{mat} + \begin{bmatrix} S & 0 \\ 0 & 1 \end{bmatrix}^\top K_{inc} \begin{bmatrix} S & 0 \\ 0 & 1 \end{bmatrix} \right) \begin{bmatrix} \hat{u} \\ \mathbf{E} \end{bmatrix} \quad \forall u^h \in V^h \tag{3.41}$$

- Linear elasticity problem

Under the action of the external forces $\mathbf{f}$, the elastic equilibrium writes:

$$div\ \overline{\sigma} + \mathbf{f} = 0 \quad \text{in } P \tag{3.42}$$

With the demonstration presented in section 1.3.3, by applying the multiscale method, the variational problems leads to:

$$\begin{cases} \forall \mathbf{u}^* \in H^1_{per}(P),\ \forall \overline{E}^* \in \mathbb{R}^{3\times 3}_{sym}, \\ \displaystyle\int_P \mathbb{C}\left(\overline{E}^0 + \overline{e}_y(\mathbf{u}^1)\right) : \left(\overline{E}^* + \overline{e}_y(\mathbf{u}^*)\right) = (\mathbb{C}^{hom}\overline{E}^0) : \overline{E}^* \end{cases} \tag{3.43}$$

The resolution of the six problems (3.43) as $(\mathbb{C}^{hom}\overline{E}^0)$ spans $\mathbb{R}^{3\times 3}_{sym}$, gives the homogenized elasticity tensor calculated with periodic condition $\mathbb{C}^{hom}$.

To apply the PFEM, from the variational problem (3.43), let us consider the quadratic energy functional:

$$J(\mathbf{u}, \overline{E}) = \int_P \mathbb{C}\left(\overline{E} + \overline{e}_y(\mathbf{u})\right) : \left(\overline{E} + \overline{e}_y(\mathbf{u})\right) \tag{3.44}$$

We split the energy form as in the thermal case :

$$\begin{aligned} J(\mathbf{u}, \overline{E}) = & \underbrace{\int_P \mathbb{C}_{mat}(\overline{E} + \overline{e}_y(\mathbf{u})) : (\overline{E} + \overline{e}_y(\mathbf{u}))}_{J_{mat}} \\ + & \underbrace{\int_{P_{inc}} (\mathbb{C}_{inc} - \mathbb{C}_{mat})(\overline{E} + \overline{e}_y(\mathbf{u})) : (\overline{E} + \overline{e}_y(\mathbf{u}))}_{J_{inc}} \end{aligned} \tag{3.45}$$

Considering two interpolation spaces $\mathbf{u}^h \in \mathbf{V}^h$ and $\mathbf{v}^l \in \mathbf{W}^l$, We define the matrix K_{mat} of dimension $(n+3)\times(n+3)$ in 2D, $(n+6)\times(n+6)$ in 3D, so as the matrix K_{inc} :

$$\begin{aligned} J_{mat}(\mathbf{u}^h, \overline{E}) &= \int_P \mathbb{C}_{mat}(\overline{E} + \overline{e}_y(\mathbf{u})) : (\overline{E} + \overline{e}_y(\mathbf{u})) \\ &= \begin{bmatrix} \hat{\mathbf{u}} \\ \overline{E} \end{bmatrix}^\top K_{mat} \begin{bmatrix} \hat{\mathbf{u}} \\ \overline{E} \end{bmatrix}, \quad \forall \mathbf{u}^h \in \mathbf{V}^h \end{aligned} \tag{3.46}$$

$$\begin{aligned} J_{inc}(\mathbf{v}^l, \overline{E}) &= \int_{P_{inc}} (\mathbb{C}_{inc} - \mathbb{C}_{mat})(\overline{E} + \overline{e}_y(\mathbf{u})) : (\overline{E} + \overline{e}_y(\mathbf{u})) \\ &= \begin{bmatrix} \hat{\mathbf{v}} \\ \overline{E} \end{bmatrix}^\top K_{inc} \begin{bmatrix} \hat{\mathbf{v}} \\ \overline{E} \end{bmatrix}, \quad \forall \mathbf{v}^l \in \mathbf{W}^l \end{aligned} \tag{3.47}$$

A substitution matrix S, similarly to the thermal case but for all the components of the displacement is defined, so that we can substitute the DOFs $\hat{\mathbf{v}}$ defined in the inclusion S for the DOFs $\hat{\mathbf{u}}$ defined on the structured mesh P. The deformation energy form reads :

$$J(\mathbf{u}^h, \overline{E}) = \begin{bmatrix} \hat{\mathbf{u}} \\ \overline{E} \end{bmatrix}^\top \left(K_{mat} + \begin{bmatrix} S & 0 \\ 0 & 1 \end{bmatrix}^\top K_{inc} \begin{bmatrix} S & 0 \\ 0 & 1 \end{bmatrix} \right) \begin{bmatrix} \hat{\mathbf{u}} \\ \overline{E} \end{bmatrix}, \quad \forall \mathbf{u}^h \in \mathbf{V}^h \tag{3.48}$$

3.4 Numerical Experiments

In order to validate and estimate the performance of the Phantom domain Finite Element Method (PFEM) for numerical homogenization, we present here some numerical experiments. We shall study thermal conductivity and linear elasticity for 2D and 3D case.

3.4.1 Inclusion types

Let's consider the RVE defined with inclusions of elementary geometry, such as sphere, cube and ellipsoid in three dimensional case, disk and square in two dimensional case.

- A sphere is defined by the coordinates of its center and its diameter d, see Figure 3.1.

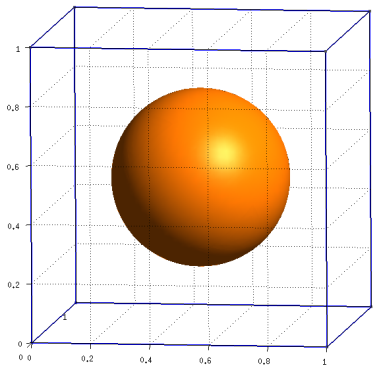

Figure 3.1: RVE with one spherical inclusion of diameter $d = 0.6$, volume fraction $\rho = 0.1131$

- A disk is defined by the coordinates of its center and its diameter d, see Figure 3.2.
- A cube is defined by the coordinates of its center and its side l, see Figure 3.3.
- A square is defined by the coordinates of its center and its side l, see Figure 3.4.
- An ellipsoid is defined by its center coordinates and its principal axis, see Figure 3.5. Or it can be defined as a volume, the boundary of which is defined by a quadric:

$$\frac{x^2}{a^2} + \frac{y^2}{b^2} + \frac{z^2}{c^2} = 1.$$

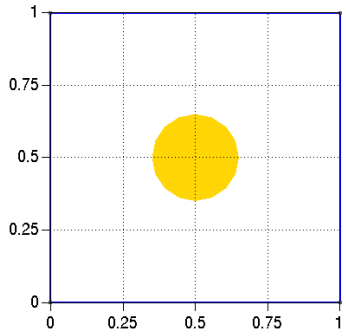

Figure 3.2: RVE with one disk inclusion of diameter $d = 0.3$ in domain Ω, volume fraction $\rho = 0.0707$

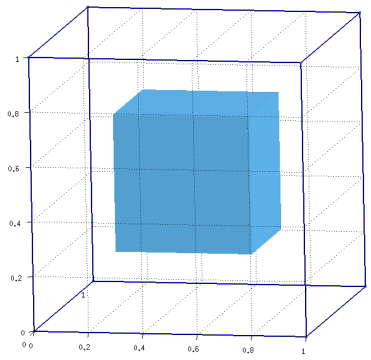

Figure 3.3: RVE with one cubic inclusion of side $l = 0.5$, volume fraction $\rho = 0.125$

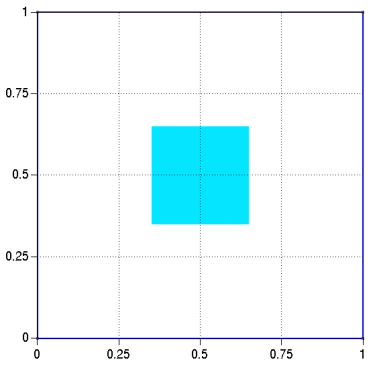

Figure 3.4: RVE with one square inclusion of side $l = 0.3$ in domain Ω, volume fraction $\rho = 0.09$

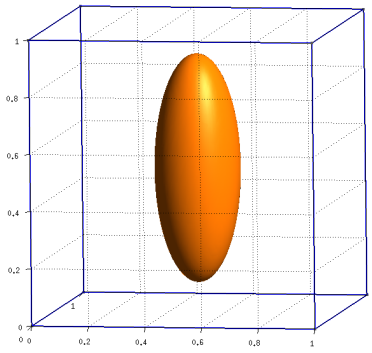

Figure 3.5: RVE with one ellipsoidal inclusion, $a = 0.15, b = 0.15, c = 0.4$, volume fraction $\rho = 0.0377$

3.4.2 Meshes of PFEM

As usual a structured mesh is used for the domain $\Omega = [0,1]^3$ or the RVE $P = [0,1]^3$, which is characterized by its resolution N_{rve}. In the following, to simplify the reading, we use the word 'RVE' to represent the domain Ω in KUBC and SUBC case and the RVE P in periodic case.

As mentioned in the section 2.3.2, the mesh of the inclusion must be sufficiently refined compared to the mesh of the RVE, so that the resulting pixelization recovers the inclusion entirely. But the mesh of the inclusion does not need to be too fine since that does not improve the approximation beyond a certain value. In all of our following numerical studies, the ratio η is set to an optimal value $\eta = 1$.

We have decided to use the 8-nodes hexaedric element (cub8) for both RVE and inclusions. The spherical and cubic inclusions meshed by hexaedric element is shown in Figure 3.6.

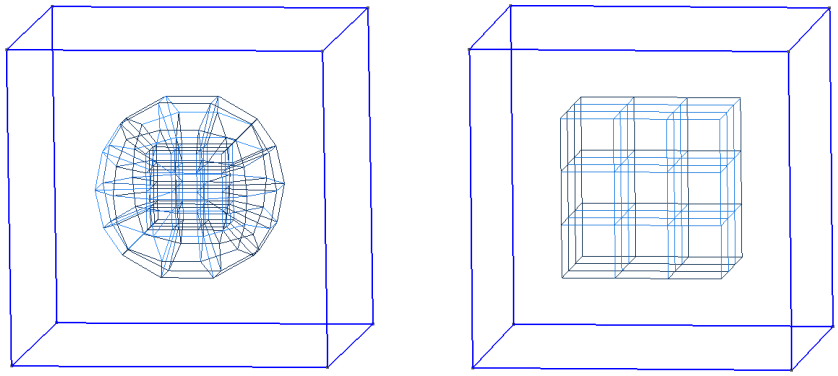

Figure 3.6: Spherical (left) and cubic (right) inclusions in hexaedric mesh

3.4.3 Constitutive law and effective coefficients

Isotropic materials

If the inclusion is in shape of sphere or cube, *a priori*, the composite material is isotropic. we consider isotropic constitutive laws for matrices and inclusions. In a thermal conductivity problem, the respective normalised conductivity tensors are defined as:

$$\begin{cases} \Lambda_0 = \mathbb{I} \\ \Lambda_1 = c_{thermal}\mathbb{I} \end{cases}$$

where $c_{thermal}$ designates the contrast between the matrix and the inclusion. The contrast $c_{thermal}$ is set to 100 for the following experiments.

From the conductivity tensor Λ, we introduce the conductivity coefficient λ defined as:

$$\lambda = \frac{Trace(\Lambda)}{3} = \frac{\Lambda_{11} + \Lambda_{22} + \Lambda_{33}}{3}$$

This conductivity coefficient is used in the following studies to present computed solutions for thermal conductivity problems.

In a linear elasticity problem, we consider isotropic constitutive laws in Voigt notation (see Appendix B), we have:

$$\mathbb{C} = \frac{E}{(1+\nu)(1-2\nu)} \begin{bmatrix} 1-\nu & \nu & \nu & 0 & 0 & 0 \\ \nu & 1-\nu & \nu & 0 & 0 & 0 \\ \nu & \nu & 1-\nu & 0 & 0 & 0 \\ 0 & 0 & 0 & \frac{1-2\nu}{2} & 0 & 0 \\ 0 & 0 & 0 & 0 & \frac{1-2\nu}{2} & 0 \\ 0 & 0 & 0 & 0 & 0 & \frac{1-2\nu}{2} \end{bmatrix}$$

where E denotes the Young's modulus and ν is the Poisson's ratio. The normalised Young's modulus and Poisson's ratio are used to characterise the matrix and the inclusion:

$$\begin{cases} E_0 = 1, \nu_0 = \frac{1}{3} \\ E_1 = c_{elastic}, \nu_1 = \frac{1}{3} \end{cases}$$

The contrast $c_{elastic}$ is set to 100 for the following study.

As the composite material of RVE with a spherical inclusion is isotropic, to present the effective properties, we use the bulk modulus k and the shear modulus μ, defined as:

$$k = \frac{E}{3(1-2\nu)}; \quad \mu = \frac{E}{2(1+\nu)}$$

Numerically, the coefficients k and μ are computed from the tensor $\mathbb{C}$:

$$k = \frac{\mathbb{C}_{1111} + \mathbb{C}_{1122} + \mathbb{C}_{1133} + \mathbb{C}_{2211} + \mathbb{C}_{2222} + \mathbb{C}_{2233} + \mathbb{C}_{3311} + \mathbb{C}_{3322} + \mathbb{C}_{3333}}{9}$$

$$\mu = \frac{\mathbb{C}_{1111} + \mathbb{C}_{2222} + \mathbb{C}_{3333} + 2(\mathbb{C}_{2323} + \mathbb{C}_{3131} + \mathbb{C}_{1212}) - 3k}{10}$$

Transversely isotropic materials

In case of ellipsoidal inclusions, materials constituted with such RVE are not isotropic, especially if the contrast is large. Thus, for the thermal case, we analyze the diagonal terms of the effective conductivity tensor Λ (i.e., Λ_{11}, Λ_{22} and Λ_{33}).

In the linear elasticity case, since we have a transversely isotropic material in the plane ($\mathbf{x}$, $\mathbf{y}$) and in the longitudinal axis ($\mathbf{z}$), the computation of the compliance tensor $\mathbb{S}$ in the Bechterew basis (see Appendix B), makes it possible to identify the Young's modulus E_1, E_3 and the shear modulus G_{31}:

$$\mathbb{S} = \begin{bmatrix} \frac{1}{E_1} & \frac{-\nu_{12}}{E_1} & \frac{-\nu_{31}}{E_3} & 0 & 0 & 0 \\ \frac{-\nu_{12}}{E_1} & \frac{1}{E_1} & \frac{-\nu_{31}}{E_3} & 0 & 0 & 0 \\ \frac{-\nu_{31}}{E_3} & \frac{-\nu_{31}}{E_3} & \frac{1}{E_3} & 0 & 0 & 0 \\ 0 & 0 & 0 & \frac{1}{2G_{31}} & 0 & 0 \\ 0 & 0 & 0 & 0 & \frac{1}{2G_{31}} & 0 \\ 0 & 0 & 0 & 0 & 0 & \frac{1+\nu_{12}}{E_1} \end{bmatrix}$$

with

$$E_1 = \frac{2}{\mathbb{S}_{1111} + \mathbb{S}_{2222}}$$
$$E_3 = \frac{1}{\mathbb{S}_{3333}}$$
$$G_{31} = \frac{1}{\mathbb{S}_{2323} + \mathbb{S}_{3131}}$$

Thus, for non-isotropic material, we analyze the Young's modulus E_1, E_3 and the shear modulus G_{31} instead of k and μ.

To take into account the orientation of the inclusion, we use the Euler angles which allow, by three successive rotations, to pass from the global RVE basis to the local inclusion basis. The change of basis is achieved with the help of a transformation matrix [20].

3.4.4 Reference solutions and relative errors

Mori-Tanaka model

If the volume fraction of spherical or ellipsoidal inclusion ρ is small enough, the analytical Mori-Tanaka model, based on the Eschelby's tensor is used as the reference solution [48], both in thermal conductivity and linear elasticity cases, see [76, 99].

As presented in section 1.2.2, the effective conductivity tensor is determined by Mori-Tanaka model as follows:

$$\Lambda^{MT} = \Lambda_0 + \rho_1(\Lambda_1 - \Lambda_0)\mathbb{T}_1^{MT}\left(\rho_0\mathbb{I} + \rho_1\mathbb{T}_1^{MT}\right)^{-1} \tag{3.49}$$

with

$$\mathbb{T}_1^{MT} = \left[\mathbb{I} + \mathbb{S}_1^E(\Lambda_0)^{-1}(\Lambda_1 - \Lambda_0)\right]^{-1}$$

where Λ_0, Λ_1 denote respectively the conductivity tensor of the matrix and the inclusion; ρ_0, ρ_1 the respective volume fraction; $\mathbb{S}_1^E$ the Eshelby tensor in the thermal conductivity case (the components of the Eshelby tensor for a spherical inclusion or an ellipsoidal inclusion are given in Appendix C).

In linear elasticity case, the effective stiffness tensor is determined by Mori-Tanaka model as:

$$\mathbb{C}^{MT} = \mathbb{C}_0 + \rho_1(\mathbb{C}_1 - \mathbb{C}_0)\mathbb{T}_1^{MT}\left(\rho_0\mathbb{I} + \rho_1\mathbb{T}_1^{MT}\right)^{-1}$$

with

$$\mathbb{T}_1^{MT} = \left[\mathbb{I} + \mathbb{S}_1^E(\mathbb{C}_0)^{-1}(\mathbb{C}_1 - \mathbb{C}_0)\right]^{-1}$$

where $\mathbb{C}_0$, $\mathbb{C}_1$ denote respectively the stiffness tensor of the matrix and the inclusion; $\mathbb{S}_1^E$ is the Eshelby's tensor (the expression of the Eshelby tensor for a spherical inclusion in linear elasticity case is given in Appendix C).

Fast Fourier Transform method

The iterative methods based on the FFT (Fast Fourier Transform) give in several cases an almost exact solution since the geometry is exactly reproduced by the voxelisation, see [78]. For example, if we consider a centered cubic inclusion of side $l = 0.5$, the voxelizations should be made in multiple of 4 subdivisions in order to match the geometry. In such cases, the FFT calculation (with a voxelization resolution 100) is then considered as a reference solution.

For FFT computation, in the case of finite contrast, Moulinec and Silva [77] have shown that the most efficient scheme is the accelerated scheme. This scheme is introduced by Eyre and Milton [29] for the thermal conductivity case, which can also be used for the linear elasticity case [70].

Relative errors

The relative error of the effective conductivity coefficients between PFEM and the reference solution, for example Mori-Tanaka model, is defined as:

$$\text{Relative error}(\lambda^{eff}) = \frac{|\lambda^{eff} - \lambda^{MT}|}{\lambda^{MT}} \tag{3.50}$$

We denote respectively the effective conductivity coefficients computed by PFEM with KUBC, SUBC and periodic homogenization as λ^{kubc}, λ^{subc} and λ^{hom}. In (3.50), we replace λ^{eff} by λ^{kubc}, λ^{subc} and λ^{hom} to calculate the relative error in KUBC, SUBC and periodic cases.

The relative error of the effective elastic coefficients between PFEM and the reference solution is defined in the same way in (3.50). We replace the thermal coefficient λ by the elastic coefficients k and μ to calculate the relative error in linear elasticity case.

3.4.5 Case of RVE with single inclusion

We start the numerical evaluation of the PFEM with cases of RVEs with a single inclusion. We focus on the experiments for elementary geometries for which we can easily define some reference solutions.

One spherical inclusion

In case of one spherical inclusion, we have plotted the relative error of effective conductivity coefficients between the numerical solutions and the reference Mori-Tanaka solution in Figure 3.7. The numerical solutions have been computed by PFEM with KUBC, SUBC and periodic homogenization.

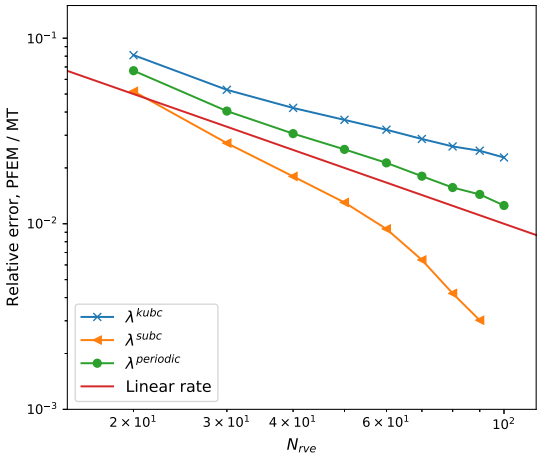

Figure 3.7: Case of one spherical inclusion $d = 0.6$. Relative Error of conductivity coefficient λ computed by PFEM with KUBC, SUBC and periodic homogenization.

In Figure 3.7, linear convergences are observed with respect to the RVE resolution for KUBC and periodic homogenization. With a resolution $N_{rve} = 100$, the relative error of Λ^{hom} is about 1%. The non-linear convergence of the effective conductivity coefficient λ^{subc} is caused by the inaccuracy of the referenced Mori-Tanaka solution. More precisely, with inclusion of volume fraction $\rho = 11.3\%$, the precision of Mori-Tanaka model reaches a certain limit ($\simeq 10^{-2}$). If the PFEM and Mori-Tanak solutions are too close, the behavior of the relative error will be uncertain.

In Figure 3.8, we compare the evolution of the normalised effective conductivity coefficient λ^{eff} in terms of inclusion's volume fraction ρ between the Mori-Tanaka model, the FFT method (in resolution 100) and the PFEM (in resolution $N_{rve} = 100$) computed with KUBC, SUBC and periodic homogenization.

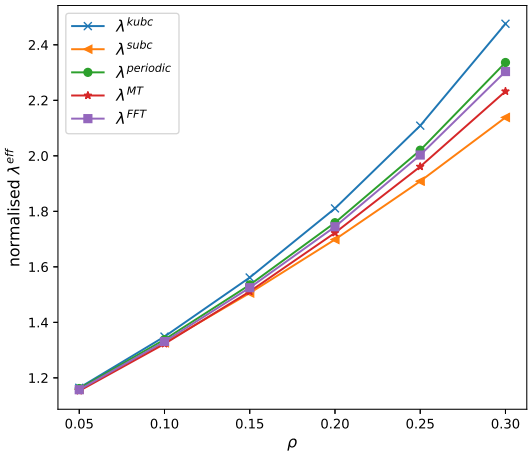

Figure 3.8: Case of one spherical inclusion. The normalised effective conductivity coefficient λ^{eff} computed by Mori-Tanaka model, FFT method and PFEM with KUBC, SUBC and periodic homogenization, versus volume fraction ρ.

The PFEM computation with KUBC, SUBC and periodic boundary condition give different numerical results of effective properties. A favorable match is observed between the PFEM periodic homogenization and other models, especially in low volume fraction. we note that the PFEM computation with KUBC over estimates the effective properties, while the PFEM computation with SUBC under estimates them.

The relative error of the effective elastic coefficients k and μ have been plotted versus the RVE resolution in Figure 3.9. We notice an almost linear convergence with respect to the RVE resolution for the effective bulk modulus, which is similar to the thermal case. We also observe a convergence for the effective shear modulus but with a slower rate. Furthermore, the relative error is more important for the shear modulus with a discrepancy of 10%.

In Figure 3.10, we compare the evolution of the normalised effective elasticity coefficient k and μ in terms of inclusion's volume fraction ρ between the reference solutions and the PFEM solutions (in resolution $N_{rve} = 100$).

From Figure 3.10, we observe a good accordance between the PFEM and other methods for the effective bulk modulus k, especially in low volume fraction. For the effective shear modulus μ, the discrepency between each method is obviously more important.

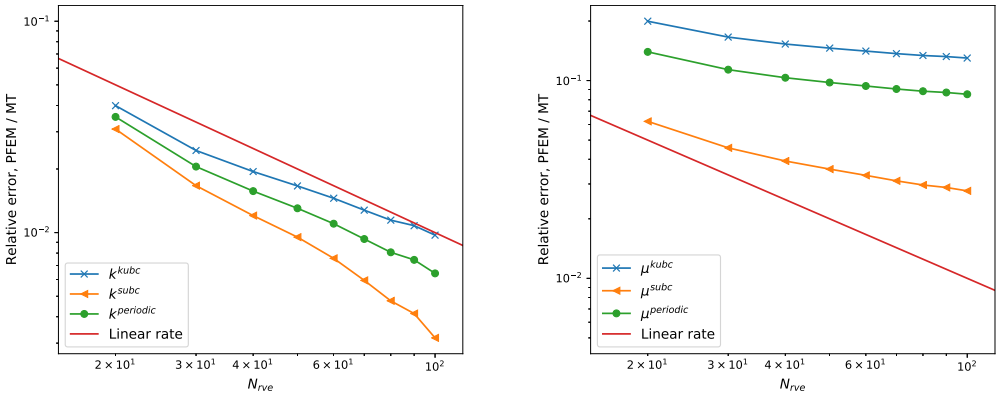

Figure 3.9: Case of one spherical inclusion $d = 0.6$. Relative Error of bulk modulus k and shear modulus μ computed by PFEM with KUBC, SUBC and periodic homogenization.

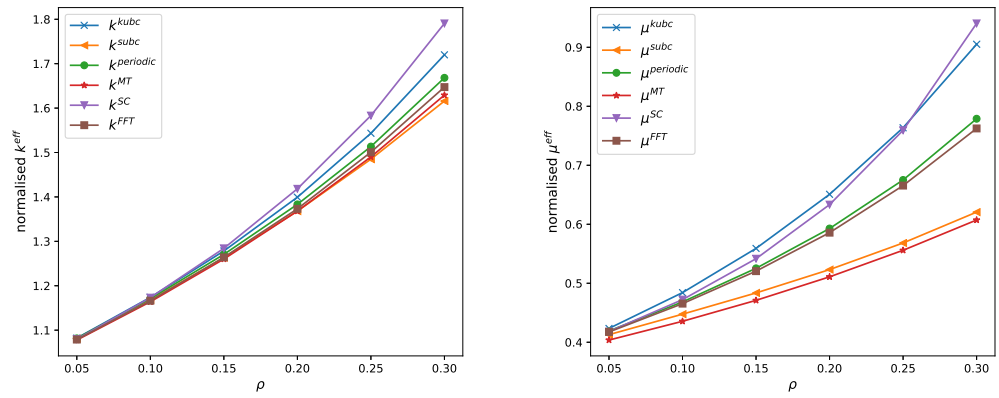

Figure 3.10: Case of one spherical inclusion. The normalised effective bulk modulus k and shear modulus μ computed by Mori-Tanaka model, self-consistent model, the FFT method and PFEM with KUBC, SUBC and periodic homogenization, versus volume fraction ρ.

One disk inclusion

In the case of KUBC or SUBC condition, the effective coefficients are computed by solving respectively pure Dirichlet boundary value problem (3.1) or pure Neumann boundary value problem (3.17) using PFEM. For RVE with one disk inclusion, the numerical solutions of such problems are presented in the previous chapter, see Figure 2.19 and Figure 2.20 for thermal conductivity case, see Figure 2.21 and Figure 2.22 for linear elasticity case.

In Figure 3.11, we have plotted the relative error of the effective thermal coefficient λ computed by such PFEM solutions. The reference solution is given by Mori-Tanaka model. The elastic case is presented in Figure 3.12.

The behaviours of the effective properties in two-dimensional case are similar to that in three-dimensional case. We notice a linear convergence for the

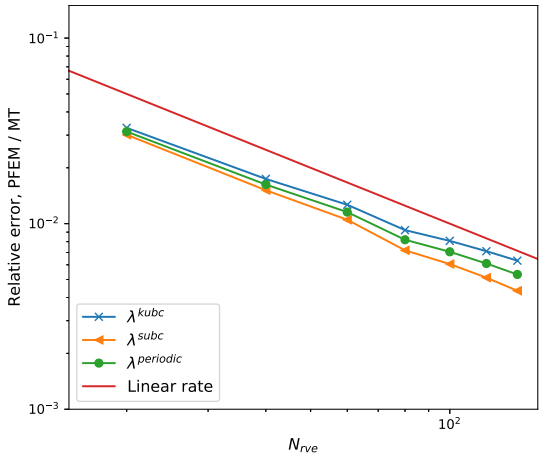

Figure 3.11: Case of one disk inclusion $d = 0.3$. Relative error of the effective thermal coefficient λ computed by PFEM with KUBC, SUBC and periodic homogenization.

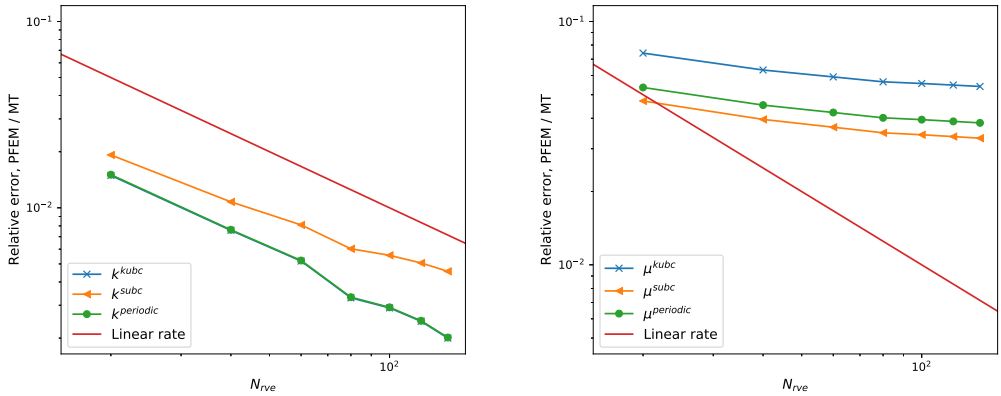

Figure 3.12: Case of one disk inclusion $d = 0.3$. Relative error of the effective elastic coefficients k, μ computed by PFEM with KUBC, SUBC and periodic homogenization.

effective properties λ and k.

One cubic inclusion

In Figure 3.13, we have depicted the relative error of effective conductivity coefficients between the PFEM and the reference FFT solution.

With a contrast $c_{thermal} = 100$, a linear convergence is observed for the effective coefficient λ^{eff} with KUBC, SUBC and periodic homogenization. We have also noticed that the effective coefficient computed with the mentioned three conditions is not the same. With KUBC, the effective coefficient is overestimated than the other two conditions.

In Figure 3.14, the relative error of effective elasticity coefficients k et μ have been depicted versus the RVE resolution. The relative error referenced to FFT solution is calculated analogously as in the thermal conductivity problem.

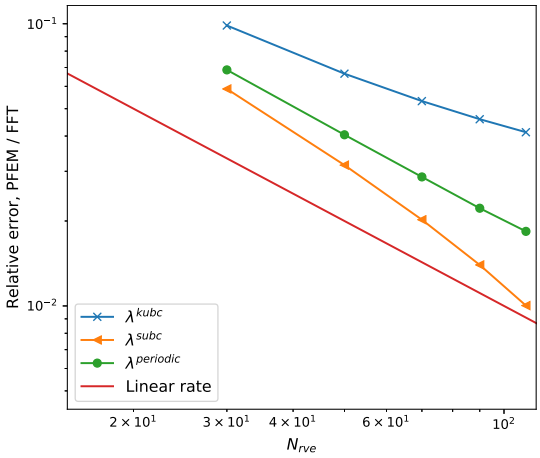

Figure 3.13: Case of one cubic inclusion $l = 0.5$. Relative error of the thermal effective coefficient λ computed by PFEM with KUBC, SUBC and periodic homogenization.

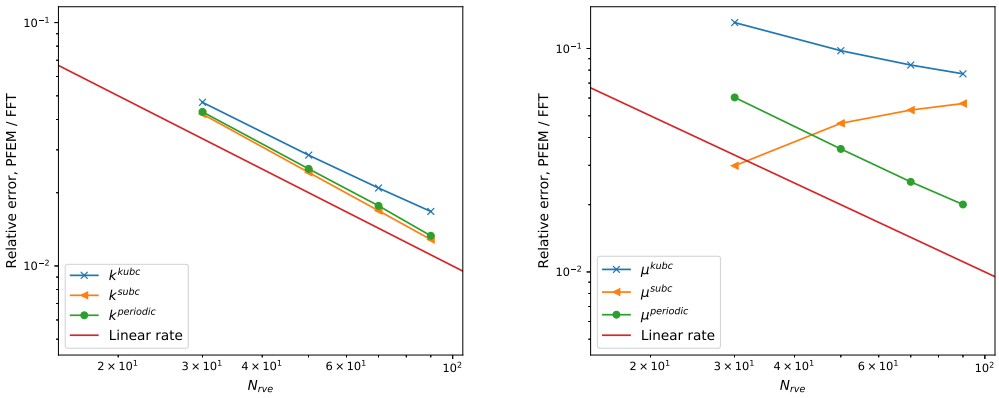

Figure 3.14: Case of one cubic inclusion $l = 0.5$. Relative error of the effective bulk modulus k and shear modulus μ computed by PFEM with KUBC, SUBC and periodic homogenization.

For KUBC, SUBC and periodic homogenization, the same observation has been found as in the thermal case, with a similar linear convergence. However, an abnormal behavior of the effective shear modulus μ^{subc} has been observed for SUBC case. This is due to the fact that the PFEM solution is too tight to the FFT solution. One can notice it by the crossing of convergence curves.

The parametric studies in terms of inclusion's volume fraction ρ is shown in Figure 3.15 and Figure 3.16, for respectively thermal conductivity problem and linear elasticity problem. Thanks to the comparison, we notice a good accordance between the FFT method (in resolution 100) and the PFEM (in resolution $N_{rve} = 100$) computed with KUBC, SUBC and periodic homogenization, especially in low volume fraction for the effective conductivity

coefficient λ^{eff} and the effective bulk modulus k^{eff}.

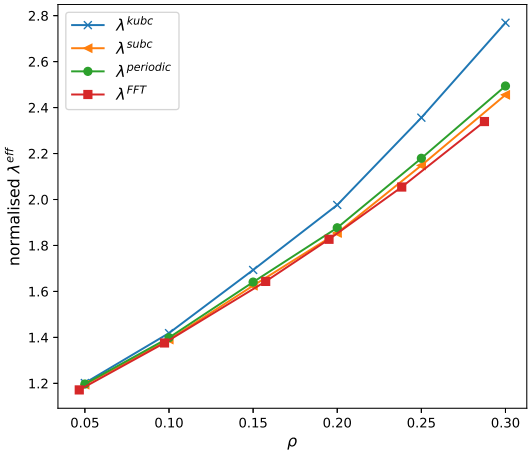

Figure 3.15: Case of one cubic inclusion. The normalised effective conductivity coefficient λ^{eff} computed by FFT method and PFEM with KUBC, SUBC and periodic homogenization, versus volume fraction ρ.

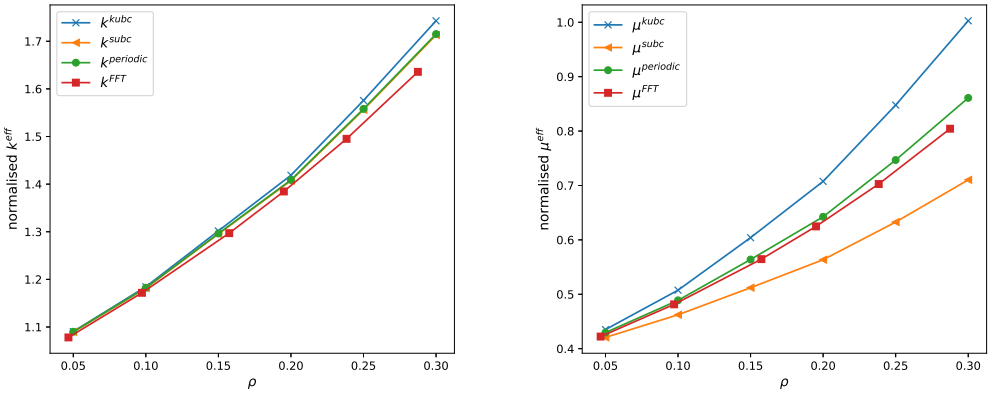

Figure 3.16: Case of one cubic inclusion. The normalised effective bulk modulus k and shear modulus μ computed by FFT method and PFEM with KUBC, SUBC and periodic homogenization, versus volume fraction ρ.

As mentioned in section 2.3.3, for cubic inclusion, a special case can be distinguished: the mesh of the RVE and the mesh of inclusion are matching. We remind that, with matching meshes, the PFEM will coincide with a conformal Finite Element Method (FEM).

In order to illustrate the behavior in the case of matching meshes, we have drawn for example, the relative error of effective bulk modulus k and shear modulus μ between the PFEM and the reference FFT solution in Figure 3.17.

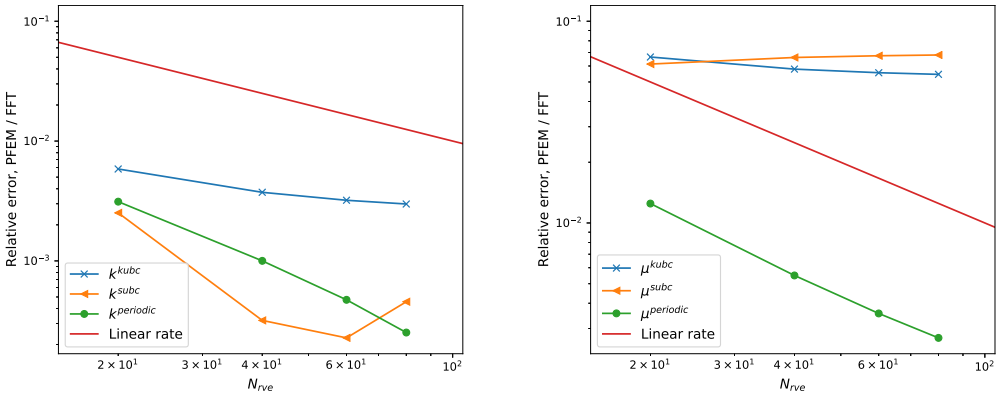

Figure 3.17: Case of one cubic inclusion $l = 0.5$ (matching meshes). Relative error of the effective bulk modulus k and shear modulus μ computed by PFEM with KUBC, SUBC and periodic homogenization.

We notice that, due to the lower value of the illustrated relative errors, the effective properties computed with matching meshes are obviously closer to the reference solution than the general case, especially in computation with periodic boundary condition.

One square inclusion

The numerical solutions of RVE with one square inclusion are presented in the previous chapter, see Figure 2.23 and Figure 2.24 for Pure Dirichlet and Neumann boundary value problems in thermal conductivity case.

In Figure 3.18, we have plotted the relative error of the effective thermal coefficient λ^{eff} computed by PFEM solutions, reference to a high resolution (1000^3) FFT computation.

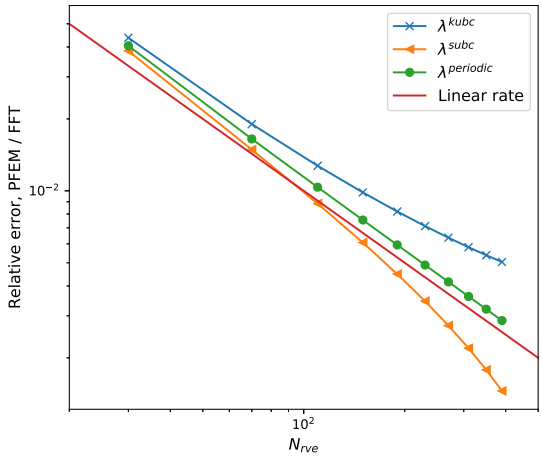

Figure 3.18: Case of one square inclusion $l = 0.3$. Relative error of the effective thermal coefficient λ^{eff} computed by PFEM with KUBC, SUBC and periodic homogenization.

We notice again the linear convergence for the computed thermal coefficient λ^{eff}, especially for the problem with periodic conditions.

One ellipsoidal inclusion

To compare the PFEM numerical solution with the Mori-Tanaka analytical solution, we have plotted, in Figure 3.19, the relative error of the effective conductivity tensor's diagonal terms for KUBC, SUBC and periodic homogenization.

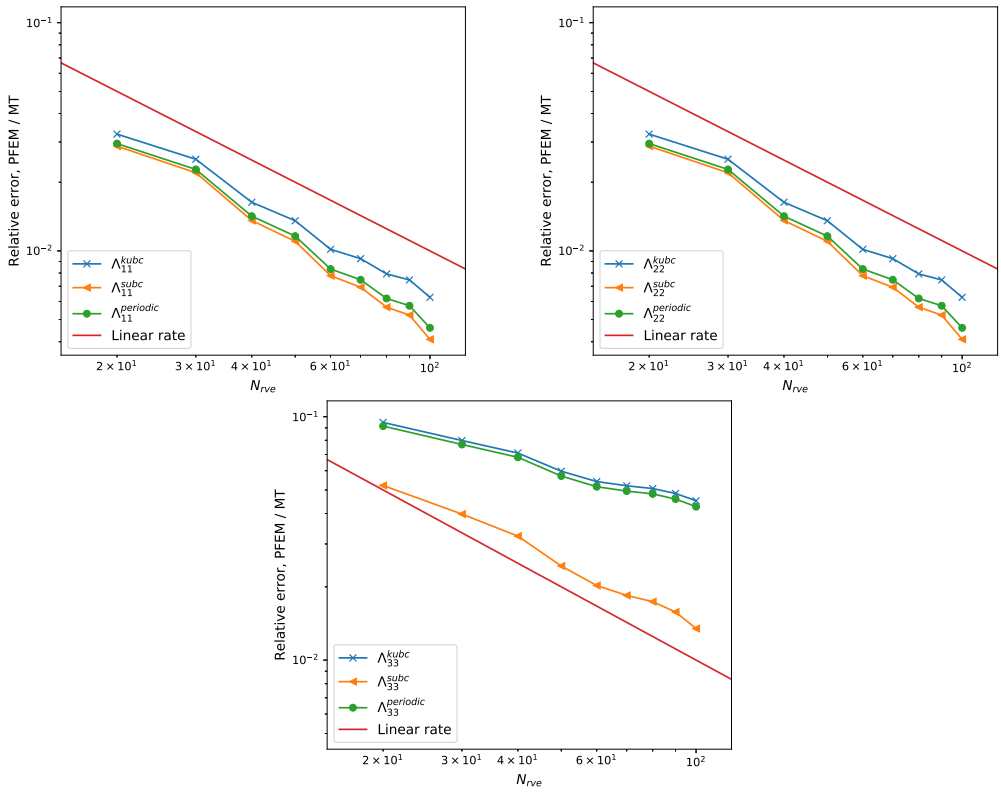

Figure 3.19: Case of one ellipsoidal inclusion $a = 0.15, b = 0.15, c = 0.4$. Relative error of the diagonal terms of the effective conductivity tensor Λ computed by PFEM with KUBC, SUBC and periodic homogenization.

The behavior of Λ_{11} and Λ_{22} are similar, due to the fact that the dimension of the studied ellipsoidal inclusion in the direction $\mathbf{x}$ and $\mathbf{y}$ are the same ($a = b$). Moreover, The linear convergence can be found for the coefficients in the plane ($\mathbf{x}$, $\mathbf{y}$), see Figure 3.19. The unexpected behavior of the coefficient in the longitudinal axis ($\mathbf{z}$) is possibly caused by the inaccuracy of the referenced Mori-Tanaka solution, in the case of which, the inclusion is too elongated in the longitudinal direction compared to the size of RVE. With a RVE resolution of 100^3, the relative error is in order of magnitude 10^{-2}.

The evolution of the normalised effective conductivity tensor Λ^{eff} versus inclusion's volume fraction ρ computed by the Mori-Tanaka model, the self-consistent model, the FFT method (in resolution 100) and the PFEM (in resolution $N_{rve} = 100$) with KUBC, SUBC and periodic homogenization is plotted in Figure 3.20.

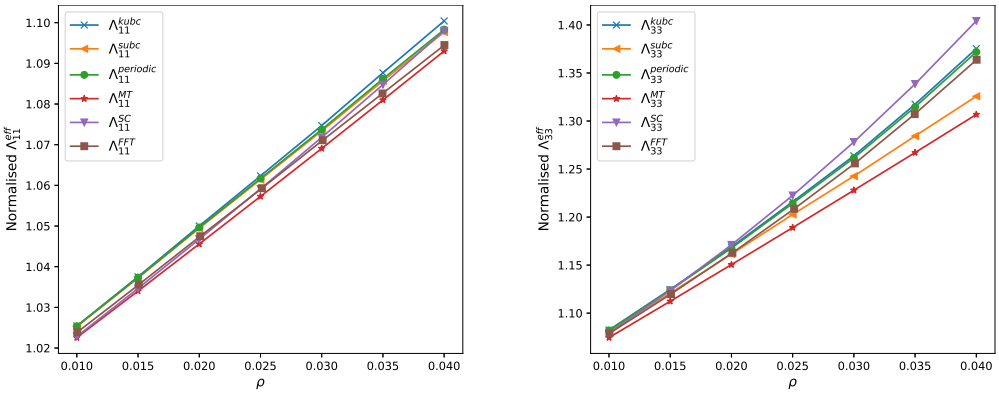

Figure 3.20: Case of one ellipsoidal inclusion. The normalised diagonal terms of the effective conductivity tensor Λ^{eff} computed by Mori-Tanaka model, Self-consistent model, FFT method and PFEM with KUBC, SUBC and periodic homogenization, versus volume fraction ρ.

The present volume fraction parametric study has shown the similarity between the PFEM and the reference solutions, especially for two full field methods: the FFT and the PFEM with periodic condition.

For linear elasticity problem, in Figure 3.21, we observe that, for KUBC and periodic homogenization, the linear convergence can be found for the coefficients in the plane ($\mathbf{x}$, $\mathbf{y}$), as in the thermal case. The weak precision of the coefficients in the longitudinal axis ($\mathbf{z}$) is probably due to the inaccuracy of the referenced Mori-Tanaka solution. For SUBC case, we notice a curve crossing for the Young's modulus E_1 and E_3.

Figure 3.22 shows the volume fraction parametric studies for the PFEM and the reference methods (MT, SC, FFT) in linear elasticity problem. With a volume fraction $\rho = 0.04$, the difference of effective coefficients between each method is significant, particularly for E_3, while a good accordance is always observed for the FFT and the PFEM with periodic condition. The limitation of the Mori-Tanaka method in the case of an elongated inclusion is apparently verified with the effective shear modulus G_{31} in Figure 3.22.

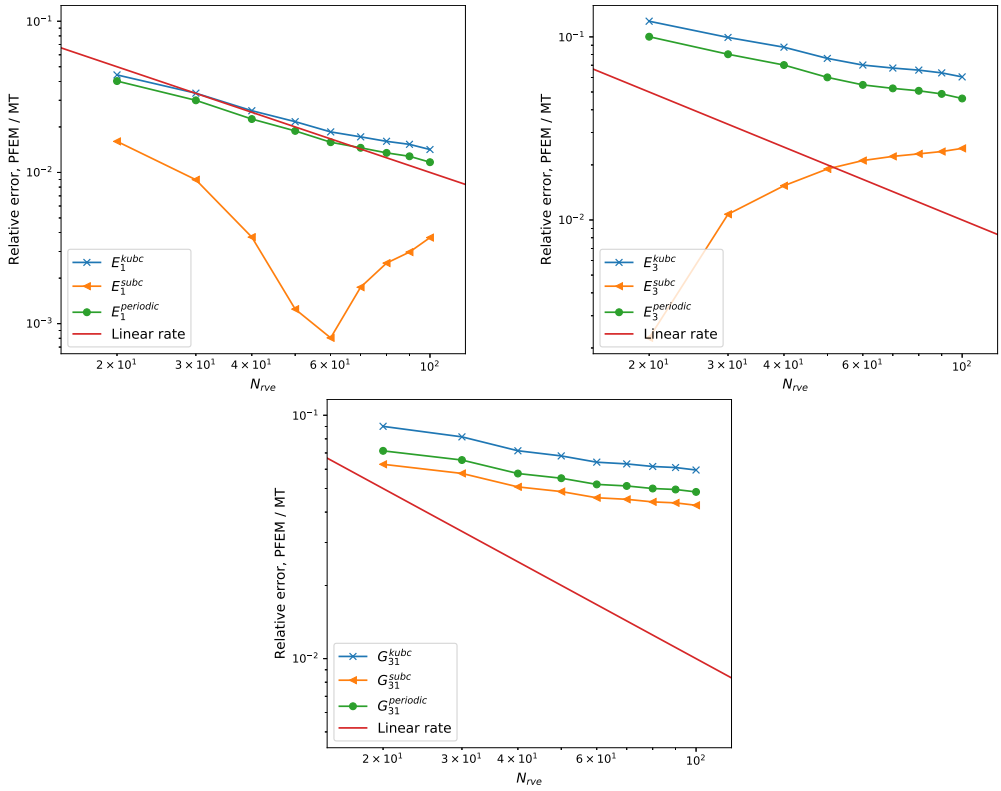

Figure 3.21: Case of one ellipsoidal inclusion $a = 0.15, b = 0.15, c = 0.4$. Relative error of the effective elastic coefficients E_1, E_3 and G_{31} computed by PFEM with KUBC, SUBC and periodic homogenization.

3.4.6 Case of RVE with multiple inclusions

To illustrate a case of multiple inclusions, let us consider eight ellipsoidal inclusions with the same size $a = 0.05, b = 0.05, c = 0.15$, which are randomly distributed and randomly oriented, see Figure 3.23. The volume fraction is $\rho = 0.01257$. We recall that the PFEM procedure is repeated for each inclusion.

As ρ is small enough, we use the Mori-Tanaka model as a reference solution both in thermal conductivity and linear elasticity cases [8]. The effective tensors are calculated as presented in the first chapter (1.19).

In Figure 3.24 and Figure 3.25, we have depicted the relative error of effective thermal coefficients Λ_{11}, Λ_{22}, Λ_{33} and elastic coefficients E_1, E_3, G_{31} between the PFEM and the reference Mori-Tanaka solution. The contrast remains unchanged; $c_{thermal} = c_{elastic} = 100$.

In both thermal and elastic cases, we have noticed a linear convergence for KUBC, SUBC and periodic homogenization, see Figure 3.24 and Figure 3.25. for instance. This observation shows that the PFEM responds properly to the cases with numbers of inclusions. But we notice that, compared to Mori-

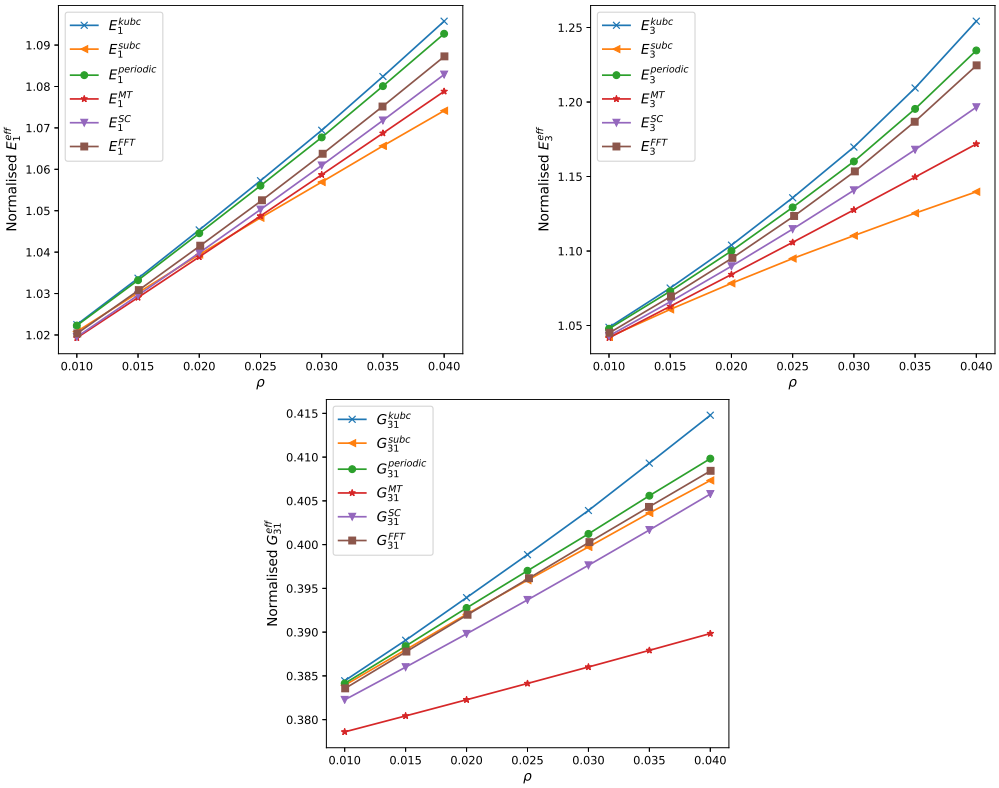

Figure 3.22: Case of one ellipsoidal inclusion. The normalised effective Young's modulus E_1, E_3 and shear modulus G_{31} computed by Mori-Tanaka model, self-consistent model, FFT method and PFEM with KUBC, SUBC and periodic homogenization, versus volume fraction ρ.

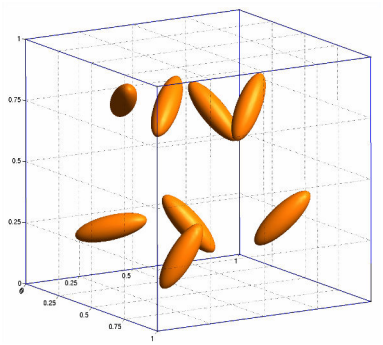

Figure 3.23: RVE with eight ellipsoidal inclusions, $a = 0.05, b = 0.05, c = 0.15$, volume fraction $\rho = 0.01257$

Tanaka model, the PFEM computation of the shear modulus is less precise with a weak convergence rate.

We consider another case of 4 disk inclusions aligned along the x axis, see Figure 3.26. An FFT computation with high resolution 8000^2 is considered as

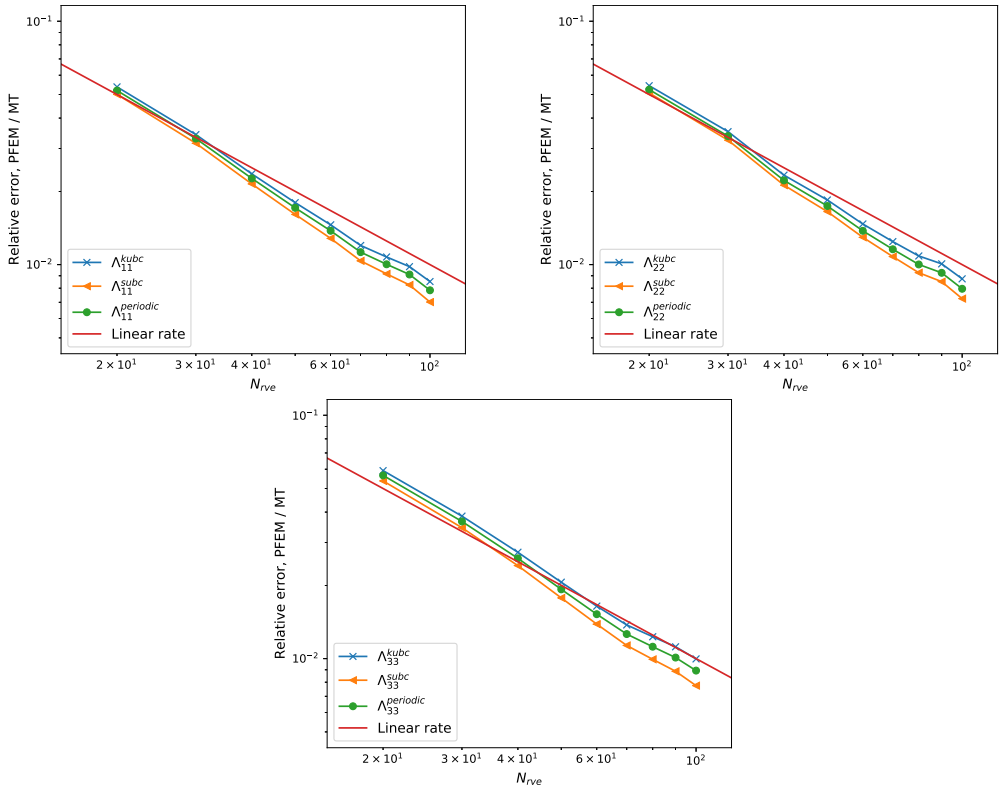

Figure 3.24: Case of eight ellipsoidal inclusions $a = 0.05, b = 0.05, c = 0.15$. Relative error of the effective conductivity tensor's diagonal terms Λ_{11}, Λ_{22}, Λ_{33} computed by PFEM with KUBC, SUBC and periodic homogenization

the reference solution. We have depicted the relative error of the homogenized conductivity tensor computed by PFEM with periodic condition in Figure 3.27.

The example of 4 disks, which are very close to each other but contactless allows us to exhibit the numerical percolation effect. This phenomenon is observed when the RVE's meshes are not fine enough regard to the inclusion's mesh. One can notice that the homogenized conductivity tensor in y axis Λ_{22}^{hom} obtained by the PFEM is in accordance with the reference FFT solution, with a relative error less than 0.1% for a mesh resolution $N_{rve} = 1000$. Whereas we notice an important discrepancy of the homogenized conductivity tensor on x axis Λ_{11}^{hom}, especially when $N_{rve} < 180$. This is cleary the numerical percolation effect.

3.5 Interesting cases of PFEM

In this section, we present some cases which are difficult to mesh by conformal finite element method (FEM), but can be easily treated by PFEM.

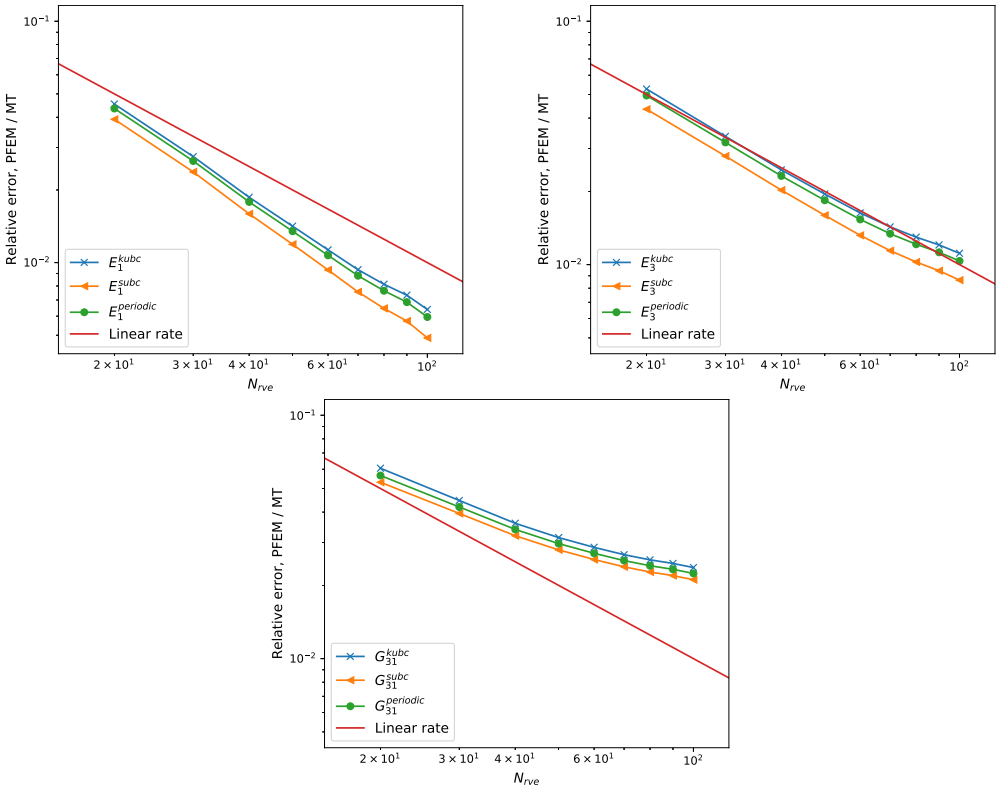

Figure 3.25: Case of eight ellipsoidal inclusions $a = 0.05, b = 0.05, c = 0.15$. Relative error of the effective elastic coefficients E_1, E_3, G_{31} computed by PFEM with KUBC, SUBC and periodic homogenization

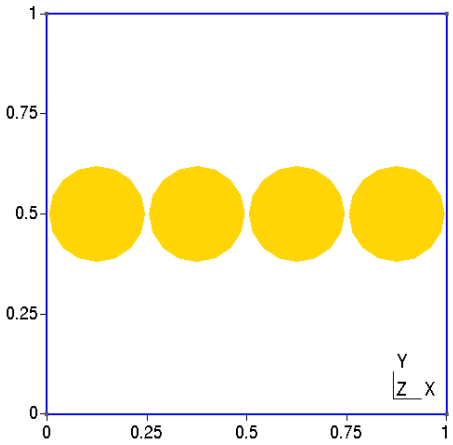

Figure 3.26: RVE with 4 disk inclusions $d = 0.24$, aligned along the x axis, volume fraction $\rho = 0.18096$

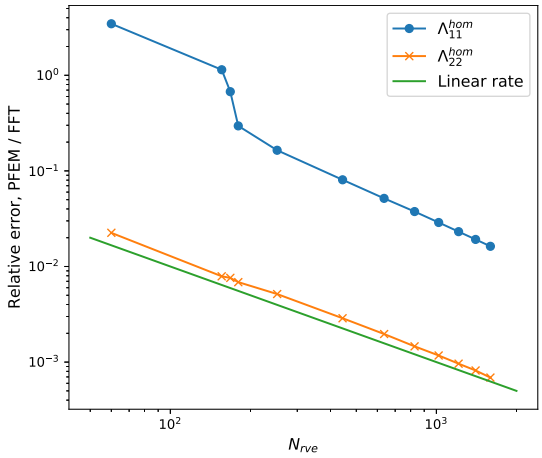

Figure 3.27: Case of 4 disk inclusions aligned along axis x. Relative error of homogenized conductivity tensor's diagonal terms Λ_{11} and Λ_{22} computed by PFEM with periodic condition referenced to FFT solution.

3.5.1 Case of inclusions on the borders of RVE

In periodic homogenization, if the inclusions are on the borders of the RVE, a fine conforming mesh is required at the edges for a standard finite element method. It may cause mesh problems or a long computation time. With PFEM, this drawback can be easily circumvented by moving periodically the nodes and elements of the inclusion mesh, see Figure 3.28.

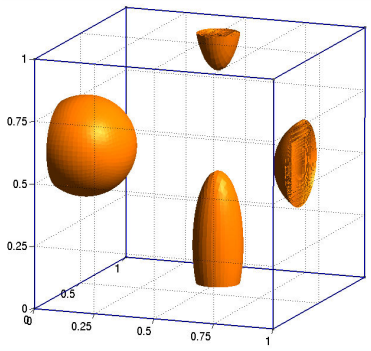

Figure 3.28: RVE with one spherical inclusion $d = 0.4$ and one ellipsoidal inclusion $a = 0.1, b = 0.1, c = 0.3$ on the borders of the RVE.

Let us consider a case of one spherical inclusion $d = 0.4$ and one ellipsoidal inclusion $a = 0.1, b = 0.1, c = 0.3$. Both inclusions touch the edges of the RVE. The volume fraction is $\rho = 0.046$.

The reference solution is given by the analytical Mori-Tanaka Model. In Figure 3.29, we again notice the linear convergences for the effective coefficients in both thermal and elastic case except the shear modulus G_{31}. This numerical

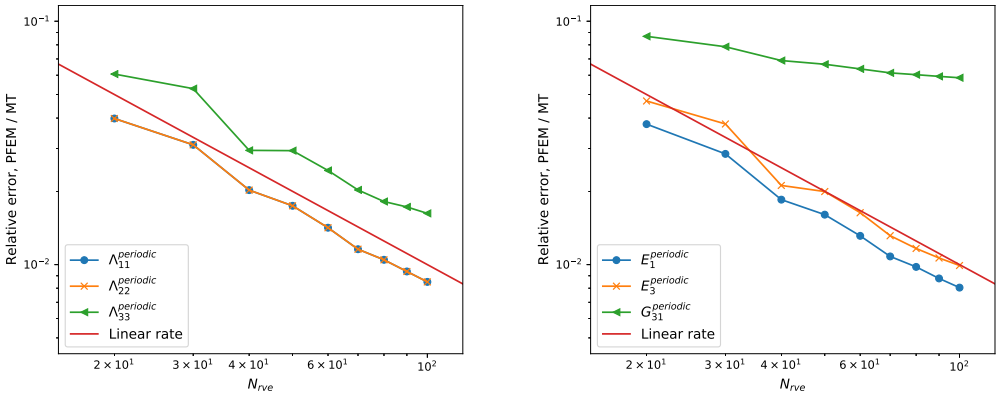

Figure 3.29: Case of one spherical inclusion $d = 0.4$ and one ellipsoidal inclusion $a = 0.1, b = 0.1, c = 0.3$ on the borders of RVE. Relative error of the effective thermal coefficients Λ_{11}, Λ_{22}, Λ_{33} and elastic coefficients E_1, E_3, G_{31} computed by PFEM in periodic homogenization.

experiment helps us to verify that PFEM works well in the case of which the inclusions are on the borders of RVE.

3.5.2 Case of pellicle / hollow sphere inclusion

With conformal finite element method (FEM), a computation of pellicle inclusion encounters significant difficulties as excessively fine meshes are required. Another advantage of the PFEM is that it can deal with the pellicle inclusion efficiently.

The reference solution is given by a three phases Mori-Tanaka model based on the Eshelby inclusions [60]. We consider a sphere of material 1 surrounded by a pellicle of material 2, which is immersed in a domain of material 3. The materials 1 and 3 are low conductive while the material 2, the pellicle, is high conductive, see Figure 3.30. We denote respectively the volume fractions and the conductivity coefficients f_1, λ_1 of the material 1, f_2, λ_2 of the material 2 and f_3, λ_3 of the material 3.

We further define l, the thickness ratio of the pellicle to the radius r of the sphere, so that the pellicle of thickness lr is situated between the spheres of radius $(1-l)r$ and r, see Figure 3.31.

In [60], Le Quang et al. developed the analytical models based on the Eshelby inclusion in the case of composites with high conductive interfaces. In the particular case of a fine spherical pellicle inclusion, with a homogeneous and isotropic inclusion in RVE, the Mori-Tanaka model writes:

$$\lambda^{MT} = \lambda_3 + \frac{3f\lambda_3(\lambda_1 - \lambda_3 + 2\widehat{\lambda}_{inc})}{3\lambda_3 + (1-f)(\lambda_1 - \lambda_3 + 2\widehat{\lambda}_{inc})} \tag{3.51}$$

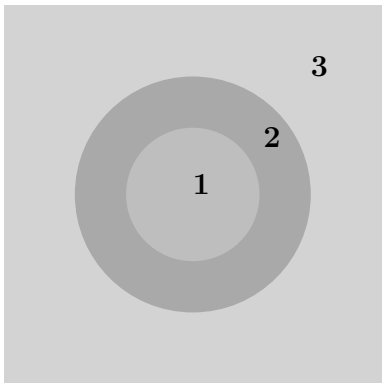

Figure 3.30: One spherical pellicle of heart 1, of pellicle 2 and of domain 3.

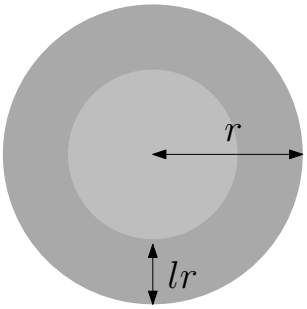

Figure 3.31: One spherical pellicle of radius r, and of thickness $h = lr$.

with $f = f_1 + f_2$ the volume fraction of the inclusion, and $\widehat{\lambda}_{inc}$ the conductivity coefficient of the pellicle defined as follows:

$$\widehat{\lambda}_{inc} = \frac{h\lambda_2}{r} = l\lambda_2 \tag{3.52}$$

Let us consider a coated spherical inclusion, centered with $d = 0.6$ depicted in Figure 3.32. Numerical experiments are performed with different thickness ratio, from a extremely thin pellicle with $l = 0.001$ to a thick case with $l = 0.5$.

In Figure 3.33, we have plotted the normalised effective conductivity coefficients λ^{eff} computed by MT method, FFT method (with resolution 100) and PFEM periodic homogenization ($N_{rve} = 100$), versus the thickness ratio. We notice that the results computed by the PFEM and the MT method are similar for all the thickness ratio value. However, the FFT method encounters its limitation when the pellicle become so thin like $l < 0.05$. In such case, the FFT pixelization requires a very high resolution to correctly describe the geometry of thin pellicle inclusion. In the PFEM, this difficulty is circumvented as the inclusion mesh is independent.

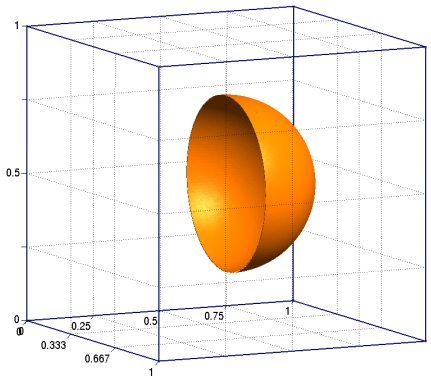

Figure 3.32: RVE with one pellicle spherical inclusion (clipping) with $d = 0.6$, thickness ratio $l = 0.01$

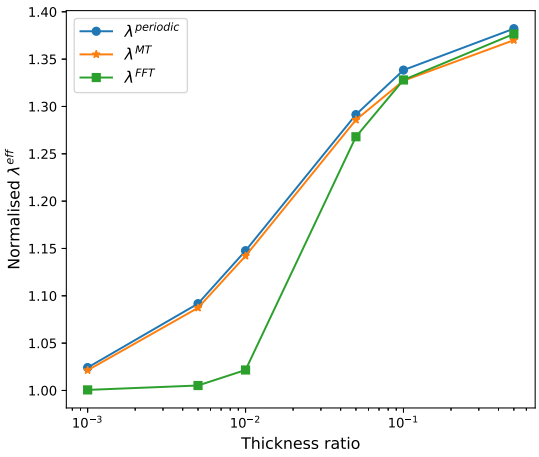

Figure 3.33: Case of one coated spherical inclusion. The effective conductivity coefficient λ^{eff} computed by FFT method, MT method and PFEM with periodic condition, versus the thickness ratio of the pellicle.

We conclude that the PFEM can be used to compute efficiently the effective properties of composite material with very thin pellicle inclusions. We also note that, a two dimensional model can be used to mesh the inclusion. This ability to consider very thin inclusions is an interesting advantage of the PFEM over other numerical homogenization methods.

Conclusion

In this chapter, we have presented Phantom domain Finite Element Method (PFEM) applied to KUBC, SUBC and periodic homogenization for thermal conductivity problem and linear elasticity problem.

In order to validate the PFEM method, numerical experiments with inclusions of elementary geometry such as sphere, cube and ellipsoid have been performed. Linear convergences of relative errors referenced to the Mori-Tanaka model or FFT solutions, for the considered effective coefficients have been shown, such as the conductivity coefficient λ, the bulk modulus k etc. On the other hand, the PFEM computation of the shear modulus is less precise with a weak convergence rate.

The numerical results of effective properties obtained by the KUBC, SUBC and periodic homogenization are different. The results of the periodic homogenization are more close to the reference solutions, especially in case of low volume fraction. we note that the KUBC homogenization overestimates the effective properties, while the SUBC homogenization underestimates them.

We also show that PFEM responds properly to the cases with multiple inclusions, coated inclusions and thin inclusions. In other words, an important feature of PFEM is that it is able to deal with the homogenization of composite materials in cases where the meshing is difficult for a conformal finite element method.

Conclusion and perspective

This thesis aimed to bring out a reliable and efficient tool able to calculate the effective properties of composite materials for thermal conductivity and linear elasticity problems. In the case of complex structure composite, the existing FEM based method and FFT based methods require a huge mesh resolution to accurately model such composites, which is computational costly. To circumvent this difficulty, we proposed in this thesis, an original alternative method named Phantom domain Finite Element Method (PFEM), using a fictitious domain principle.

In the PFEM, we split the energy functional from the equilibrium variational problem, into two parts: the RVE part and the inclusion part, which are represented by two distinct and independent meshes, instead of one conformal mesh in the standard FEM. In this way, the effort is shifted from mesh generation towards combination of the numerical integration in two parts. With isoparametric elements and a structured mesh of RVE, a substitution matrix can be constructed via developed formulae, to substitute the DOFs of inclusion mesh for the DOFs of the RVE mesh. Consequently, we are able to implement a finite element in the framework of a structured mesh of the RVE.

The PFEM is not only capable of calculating effective properties in homogenization technique with KUBC, SUBC and periodic condition, but also can be used in all the problems which can be solved by the FEM, such as the linear static thermal or elastic problems defined as Dirichlet or Neumann boundary value problems in the case of composites materials.

A library code, based on PFEM, have been developed in Python/Fortran. With the help of this code, numerical experiments in two or three dimensional cases, with inclusions of elementary geometry such as disk, square, sphere, cube and ellipsoid, have been performed to validate the PFEM method. Linear convergences of relative errors with respect to reference solutions such as the Mori-Tanaka model, the self-consistent model and the FFT method are shown for thermal and elastic effective properties. The convergence rates are observed as expected in both boundary value problems and homogenization problems with one or multiple inclusions in elementary geometry, regarding the use of linear interpolation. However, in the case of 4 disk inclusions aligned closely, we

find that, if the structured mesh is not fine enough to separate the independent meshes of each inclusion, a numerical percolation phenomenon will appear in the PFEM computation.

From the volume fraction parametric studies, we notice a gap of effective properties between the KUBC, SUBC and periodic homogenization. A favorable match is observed between the periodic homogenization and other reference models, while the KUBC homogenization over estimate the effective properties, and the SUBC homogenization under estimate them.

One interesting feature of the PFEM presented in this paper is the total flexibility concerning the inclusions meshes. Complex geometries of any kind can be considered, as long as a mesh is available. We have shown an example with very thin pellicle sphere, in case of that it is difficult to mesh by conformal finite element method or FFT method, but can be treated by PFEM. However, as the substitution procedure can be seen as a pixelization of the inclusion in the structured mesh, the 'pixels' resulting form the inclusion mesh should recover entirely the inclusion, in order to obtain an accurate approximation of the integral forms. In other words, the inclusion mesh should be fine enough compared to the structured mesh.

The performance of the PFEM has still to be improved. In convergence studies, we illustrate that the relative error of the effective properties computed by PFEM compared to reference solution is in order of magnitude $\simeq 10^{-2}$ for a computation of resolution $N_{rve} = 100$. With a cubic inclusion test, we have been able to give an estimation for the error produced by the PFEM compared to a classical finite element method with a mesh conforming to the inclusions geometry. By plotting the difference between PFEM and FEM solution, we also find that, no matter the shape of the inclusion, the peak value of errors is always located on the interface between the matrix phase and the inclusion phase. These substantial errors indicates that improvement of the accuracy of the method is needed.

In outlooks, we are particularly investigating how to introduce some kind of improvement to the accuracy of the PFEM. As we have illustrated the peak error of the PFEM is situated at interfaces, we propose to modify the shape functions involved in the finite elements situated on the boundary of the inclusion phase in order to better conform the weak continuities at interfaces.

We can imagine a case of a very high resolution three-dimensional image of a composite material sample, obtained through imagery techniques, such as tomography. We can obtain the (fine) meshes of the inclusions by segmentation techniques and then consider a coarser mesh of the sample, making the computation possible.

Numerical experiments in thermal and elastic case are performed with ma-

terials in linear constitutive law. We could extend PFEM to consider materials with nonlinear behavior. Higher-order shape functions could be implemented to evaluate the accuracy of the PFEM.

Other perspectives concern the treatment of RVE with inclusions with waviness or tortuosity, which would help us to better understand the phenomena involved in the alteration inclusions to the macroscopic behavior of the composite materials. Furthermore, the PFEM proposed in this thesis could be adapted to electromagnetism.

Appendix A

Details of homogenization theory

The details and the proofs of homogenization theory necessary for the numerical determination of effective properties are presented in this appendix.

A.1 KUBC homogenization for thermal conductivity problem

A uniform gradient of temperature is imposed at the boundary :

$$u = \mathbf{g}.\mathbf{x} \quad \forall \mathbf{x} \in \partial\Omega$$

According to the gradient theorem (see Appendix A.6):

$$\int_\Omega \nabla u = \int_{\partial\Omega} u\,\mathbf{n}$$

with $\mathbf{n}$ the outgoing normal unit vector to $\partial\Omega$ at $\mathbf{x}$, we have:

$$\begin{aligned}\int_\Omega \nabla u &= \int_{\partial\Omega} u\,\mathbf{n} \\ &= \int_{\partial\Omega} (\mathbf{g}.\mathbf{x})\,\mathbf{n} \\ &= \int_{\partial\Omega} g_i\, x_i\, n_j\, \mathbf{e_j}\end{aligned}$$

so that, $\forall j = 1, 2, 3$:

$$\begin{aligned}\int_\Omega \nabla u\, \mathbf{e_j} &= \int_{\partial\Omega} g_i\, x_i\, n_j \\ &= g_i \int_{\partial\Omega} x_i\, n_j\end{aligned}$$

However:

$$\int_{\partial\Omega} x_i \, n_j = \int_{\Omega} \nabla x_i \, \mathbf{e_j}$$

as $\nabla x_i = \mathbf{e_i}$, we have:

$$\begin{aligned} \int_{\partial\Omega} x_i \, n_j &= \mathbf{e_i} \, \mathbf{e_j} \\ &= \delta_{ij} \end{aligned}$$

Finally, we obtain:

$$\begin{aligned} \int_{\Omega} \nabla u \, \mathbf{e_j} &= \delta_{ij} \, g_i \\ &= g_j \end{aligned}$$

It implies that:

$$\begin{aligned} \langle \nabla u \rangle &= \frac{1}{|\Omega|} \int_{\Omega} \nabla u \\ &= \int_{\Omega} \nabla u \\ &= \mathbf{g} \end{aligned}$$

A.2 SUBC homogenization for thermal conductivity problem

A uniform heat flux is imposed at the boundary:

$$\mathbf{q}.\mathbf{n} = \mathbf{Q}.\mathbf{n}, \quad \forall \mathbf{x} \in \partial\Omega$$

The macroscopic temperature gradient gives:

$$\begin{aligned} \mathbf{G} &= \langle \nabla u \rangle \\ &= \int_{\Omega} \nabla u \end{aligned}$$

With $div(\mathbf{q}) = 0$ in Ω, we have:

$$\begin{aligned} div(x_i \, \mathbf{q}) &= \nabla x_i . \mathbf{q} + x_i \, div(\mathbf{q}) \\ &= \mathbf{e_i}.\mathbf{q} \\ &= q_i \end{aligned}$$

According to the divergence theorem A.4, we write:

$$\begin{aligned}\int_\Omega q_i &= \int_\Omega div(x_i\,\mathbf{q}) \\ &= \int_{\partial\Omega} x_i\,\mathbf{q}.\mathbf{n}\end{aligned}$$

With the SUBC, we have:

$$\begin{aligned}\int_{\partial\Omega} x_i\,\mathbf{q}.\mathbf{n} &= \int_{\partial\Omega} x_i\,\mathbf{Q}.\mathbf{n} \\ &= \mathbf{Q}\int_{\partial\Omega} x_i\,\mathbf{n} \\ &= \mathbf{Q}\int_\Omega \mathbf{e_i}\end{aligned}$$

which leads to the property:

$$\int_\Omega \mathbf{q} = \mathbf{Q}$$

A.3 KUBC homogenization for linear elasticity problem

We impose a displacement at point $\mathbf{x}$ belonging to the boundary $\partial\Omega$:

$$\mathbf{u} = \overline{E}\,\mathbf{x}, \quad \forall \mathbf{x} \in \partial\Omega$$

The spatial average of strain gives:

$$\begin{aligned}\langle\overline{e}\rangle &= \int_\Omega e_{ij}(\mathbf{u}) \\ &= \frac{1}{2}\left(\int_\Omega u_{i,j} + \int_\Omega u_{j,i}\right)\end{aligned}$$

According to the gradient theorem (A.5), we have:

$$\begin{aligned}\int_\Omega u_{i,j} &= \int_\Omega \nabla u_i\,\mathbf{e_j} \\ &= \left(\int_{\partial\Omega} u_i\,\mathbf{n}\right)\mathbf{e_j}\end{aligned}$$

The KUBC implies that:

$$\begin{aligned}\left(\int_{\partial\Omega} u_i\,\mathbf{n}\right)\mathbf{e_j} &= \int_{\partial\Omega}(E_{ik}\,x_k)\,n_j \\ &= E_{ik}\int_{\partial\Omega} x_k\,n_j \\ &= E_{ik}\int_{\partial\Omega}(x_k\,\mathbf{e_j})\,\mathbf{n}\end{aligned}$$

According to the divergence theorem (A.4), we have:

$$\begin{aligned} E_{ik} \int_{\partial\Omega} (x_k \, \mathbf{e_j}) \, \mathbf{n} &= E_{ik} \int_{\Omega} div(x_k \, \mathbf{e_j}) \\ &= E_{ik} \, x_{k,j} \\ &= E_{ik} \, \delta_{kj} \\ &= E_{ij} \end{aligned}$$

So that, we obtain:

$$\int_{\Omega} u_{i,j} = E_{ij}$$

With the same approach, we find:

$$\int_{\Omega} u_{j,i} = E_{ji}$$

As E_{ij} is symmetric, we have:

$$\begin{aligned} \langle \overline{e} \rangle &= \frac{1}{2} \left(\int_{\Omega} u_{i,j} + \int_{\Omega} u_{j,i} \right) \\ &= \frac{1}{2} \left(E_{ij} + E_{ji} \right) \\ &= E_{ij} \end{aligned}$$

A.4 SUBC homogenization for linear elasticity problem

We prescribe a traction vector at the boundary, reads:

$$\overline{\sigma} \, \mathbf{n} = \overline{\Sigma} \, \mathbf{n}, \quad \forall \mathbf{x} \in \partial\Omega$$

We write in index notation:

$$div(\mathbf{x} \, \overline{\sigma}) = \begin{bmatrix} (x_i \, \sigma_{1j})_{,j} \\ (x_i \, \sigma_{2j})_{,j} \\ (x_i \, \sigma_{3j})_{,j} \end{bmatrix} = \begin{bmatrix} x_{i,j} \, \sigma_{1j} + x_i \, \sigma_{1j,j} \\ x_{i,j} \, \sigma_{2j} + x_i \, \sigma_{2j,j} \\ x_{i,j} \, \sigma_{3j} + x_i \, \sigma_{3j,j} \end{bmatrix} = \begin{bmatrix} x_{i,j} \, \sigma_{1j} \\ x_{i,j} \, \sigma_{2j} \\ x_{i,j} \, \sigma_{3j} \end{bmatrix}$$

which implies:

$$div(\mathbf{x} \, \overline{\sigma}) = \overline{\sigma} \, \nabla x_i = \overline{\sigma} \, \mathbf{e_i}$$

With the divergence theorem (A.4), the spatial average of the stress tensor gives:

$$\begin{aligned} \langle \overline{\sigma} \rangle &= \int_{\Omega} \overline{\sigma} \, \mathbf{e_i} \\ &= \int_{\Omega} div(\mathbf{x} \, \overline{\sigma}) \\ &= \int_{\partial\Omega} \mathbf{x} \, \overline{\sigma} \, \mathbf{n} \end{aligned}$$

According to the static uniform boundary condition (1.34):

$$\begin{aligned}\int_{\partial\Omega} \mathbf{x}\,\overline{\sigma}\,\mathbf{n} &= \int_{\partial\Omega} \mathbf{x}\,\overline{\Sigma}\,\mathbf{n} \\ &= \overline{\Sigma}\int_{\partial\Omega} x_i\,\mathbf{n} \\ &= \overline{\Sigma}\,\mathbf{e_i}\end{aligned}$$

So that we have:

$$\langle\overline{\sigma}\rangle = \overline{\Sigma}$$

A.5 Periodic homogenization for linear elasticity problem

Using the multi-scale modelling based on asymptotic expansion, we have the microscopic equation:

$$div_y\left[\mathbb{C}(\mathbf{y})\left(\overline{E} + \overline{e}_y(\mathbf{u}^1)\right)\right] = 0 \tag{A.1}$$

with $\overline{E} \overset{\text{def}}{=} \overline{e}_x(\mathbf{u}^0)$.

We suppose that $\mathbf{u}^1$ is depending on the macroscopic space variable $\mathbf{x}$ and the microscopic space variable $\mathbf{y}$, in index notation we have:

$$\mathbf{u}^1(\mathbf{x},\mathbf{y}) = e_{pqx}(\mathbf{u}^0(\mathbf{x}))\mathbf{w}^{pq}(\mathbf{y}) \tag{A.2}$$

with the functions $\mathbf{w}$ depend on $\mathbf{y}$ and P-periodic.

We then deduce from (1.58) and (A.2) using Kronecker symbol δ_{pk} :

$$\begin{aligned}e^0_{kl} &= e_{klx}(\mathbf{u}^0) + e_{kly}(\mathbf{u}^1) \\ &= e_{klx}(\mathbf{u}^0) + e_{pqx}(\mathbf{u}^0)e_{kly}(\mathbf{w}^{pq}) \\ &= \delta_{pk}\delta_{ql}e_{pqx}(\mathbf{u}^0) + e_{pqx}(\mathbf{u}^0)e_{kly}(\mathbf{w}^{pq}) \\ &= e_{pqx}(\mathbf{u}^0)\left(\delta_{pk}\delta_{ql} + e_{kly}(\mathbf{w}^{pq})\right)\end{aligned} \tag{A.3}$$

Writing the weak formulation of the equation (A.1) on the P-periodic vector fields space of class H^1 on P denoted by $H^1_{periodic}(P)$, we have the following problem to solve:

$$\begin{cases} \forall \boldsymbol{\phi} \in H^1_{periodic}(P), \\ \displaystyle\int_P C_{ijkl}\left[e_{pqx}(\mathbf{u}^0)\left(\delta_{pk}\delta_{ql} + e_{kly}(\mathbf{w}^{pq})\right)\right] e_{ijy}(\boldsymbol{\phi}) = 0 \end{cases}$$

This problem is well-posed in the space $H^1_{periodic}(P)$ with zero average on P and admits a unique solution.

Once the $\mathbf{w}^{pq}$ functions are known, we write the expression of $\overline{\sigma}^0_{ij}$ using the equations (1.59) and (A.3):

$$\begin{aligned}\overline{\sigma}^0_{ij} &= C_{ijkl}\left[e_{pqx}(\mathbf{u}^0)\left(\delta_{pk}\delta_{ql} + e_{kly}(\mathbf{w}^{pq})\right)\right] \\ &= \left[C_{ijpq} + C_{ijkl}e_{kly}(\mathbf{w}^{pq})\right] e_{pqx}(\mathbf{u}^0)\end{aligned}$$

Then, we apply the average operator on P and by identification with $\langle\overline{\sigma}^0\rangle_P = \mathbb{C}^{periodic}\overline{E}$, we obtain the expression of the homogenized coefficients:

$$\begin{aligned}C^{periodic}_{ijpq} &= \frac{1}{|P|}\int_P \left[C_{ijpq} + C_{ijkl}e_{kly}(\mathbf{w}^{pq})\right] \\ &= \underbrace{\frac{1}{|P|}\int_P C_{ijpq}}_{\text{average coefficient}} + \underbrace{\frac{1}{|P|}\int_P C_{ijkl}e_{kly}(\mathbf{w}^{pq})}_{\text{corrective term}}\end{aligned}$$

A.6 Divergence theorem and Gradient theorem

Consider a domain $\Omega \in \mathbb{R}^N$ (with N the dimension of the domain) and a vector field $\mathbf{V}$ defined on Ω, i.e.

$$\forall x \in \Omega,\ \mathbf{V}(x) \in \mathbb{R}^n$$

According to Stokes' theorem, we have the divergence theorem:

$$\int_\Omega div\mathbf{V} = \int_{\partial\Omega} \mathbf{V}.\mathbf{n} \tag{A.4}$$

with $\partial\Omega$ the piecewise smooth boundary of the domain Ω, and $\mathbf{n}$ the outward pointing unit normal field of the boundary $\partial\Omega$.

Corollaries : Consider a scalar field u defined on Ω, we have the gradient theorem:

$$\int_\Omega \nabla u\, dV = \int_{\partial\Omega} u\,\mathbf{n}\, ds \tag{A.5}$$

It can be deduced from the divergence theorem:

$$\begin{aligned}div(u\,\mathbf{e_i}) &= \nabla u.\mathbf{e_i} + u\,div(\mathbf{e_i}) \\ &= \nabla u.\mathbf{e_i}\end{aligned}$$

So that:

$$\int_\Omega div(u\,\mathbf{e_i}) = \int_\Omega \nabla u.\mathbf{e_i}$$

Since:

$$\begin{aligned}\int_{\Omega} div(u\,\mathbf{e_i}) &= \int_{\partial\Omega} u\,\mathbf{e_i}.\mathbf{n} \\ &= \int_{\partial\Omega} u\,\mathbf{n_i} \\ &= \int_{\partial\Omega} u\,\mathbf{n}.\mathbf{e_i}\end{aligned}$$

Hence, we have the gradient theorem (A.5) and the two terms are identical by the projections in all direction $\mathbf{e_i}$.

Appendix B

Linear elasticity tensors

The objective of this appendix is to clarify the writing of symmetric fourth-order tensors intervening in linear elasticity [32].

B.1 Voigt notation

Let's consider $(\mathbf{e}_1, \mathbf{e}_2, \mathbf{e}_3)$ an orthonormal basis of $\mathbb{R}^3$. To express the 81 independent components of a fourth-order tensor, the canonical basis $(\mathbf{e}_i \otimes \mathbf{e}_j \otimes \mathbf{e}_k \otimes \mathbf{e}_l)$ is the natural base.

However, in linear elasticity, Hooke's law connects the tensor $\overline{\sigma}$ and the tensor $\overline{e}$ linearly by means of two symmetric fourth-order tensors, the stiffness tensor $\mathbb{C}$ and the compliance tensor $\mathbb{S}$:

$$\begin{aligned} \overline{\sigma} &= \mathbb{C}\,\overline{e} \\ \sigma_{ij} &= C_{ijkl}\, e_{kl} \qquad \text{with index notation} \\ \overline{e} &= \mathbb{S}\,\overline{\sigma} \\ e_{ij} &= S_{ijkl}\, \sigma_{kl} \qquad \text{with index notation} \end{aligned} \tag{B.1}$$

Hooke's law and the symmetries of the tensor $\overline{\sigma}$ and $\overline{e}$ induce the following symmetries for the components of tensor $\mathbb{C}$: $C_{ijkl} = C_{jikl}$, $C_{ijkl} = C_{jilk}$. The energetic point of view of the Hooke law implies a third symmetry: $C_{ijkl} = C_{klij}$. Thus, there remains only 21 independent components describing this tensor $\mathbb{C}$. We have the same results for the compliance tensor. The canonical base is not adapted to this type of tensor.

To express such a symmetric tensor, we often encounter the Voigt notation in which the components of the stress tensor $\overline{\sigma}$ and the stiffness tensor $\overline{e}$ are

given by $\boldsymbol{\sigma}$ and $\boldsymbol{e}$:

$$\boldsymbol{\sigma} = \begin{bmatrix} \sigma_{11} \\ \sigma_{22} \\ \sigma_{33} \\ \sigma_{23} \\ \sigma_{31} \\ \sigma_{12} \end{bmatrix} \qquad \text{and} \qquad \boldsymbol{e} = \begin{bmatrix} e_{11} \\ e_{22} \\ e_{33} \\ 2e_{23} \\ 2e_{31} \\ 2e_{12} \end{bmatrix} \tag{B.2}$$

The components of the stiffness tensor $\mathbb{C}$ are given by a 6×6 matrix, denoted $\overline{C}$:

$$\overline{C} = \begin{bmatrix} C_{1111} & C_{1122} & C_{1133} & C_{1123} & C_{1131} & C_{1112} \\ C_{2211} & C_{2222} & C_{2233} & C_{2223} & C_{2231} & C_{2212} \\ C_{3311} & C_{3322} & C_{3333} & C_{3323} & C_{3331} & C_{3312} \\ C_{2311} & C_{2322} & C_{2333} & C_{2323} & C_{2331} & C_{2312} \\ C_{3111} & C_{3122} & C_{3133} & C_{3123} & C_{3131} & C_{3112} \\ C_{1211} & C_{1222} & C_{1233} & C_{1223} & C_{1231} & C_{1212} \end{bmatrix} \tag{B.3}$$

Voigt notations for $\overline{\sigma}$, $\overline{e}$ and $\mathbb{C}$ translate well the Hooke's law in stiffness. In other words, the Voigt notation $\boldsymbol{\sigma} = \overline{C}\,\boldsymbol{e}$ is faithful to: $\sigma_{ij} = C_{ijkl}e_{kl}$.

To write the Hooke's law with compliance tensor, $\boldsymbol{e} = \overline{S}\,\boldsymbol{\sigma}$, we have:

$$\begin{bmatrix} e_{11} \\ e_{22} \\ e_{33} \\ 2e_{23} \\ 2e_{31} \\ 2e_{12} \end{bmatrix} = \begin{bmatrix} S_{1111} & S_{1122} & S_{1133} & 2S_{1123} & 2S_{1131} & 2S_{1112} \\ S_{2211} & S_{2222} & S_{2233} & 2S_{2223} & 2S_{2231} & 2S_{2212} \\ S_{3311} & S_{3322} & S_{3333} & 2S_{3323} & 2S_{3331} & 2S_{3312} \\ 2S_{2311} & 2S_{2322} & 2S_{2333} & 4S_{2323} & 4S_{2331} & 4S_{2312} \\ 2S_{3111} & 2S_{3122} & 2S_{3133} & 4S_{3123} & 4S_{3131} & 4S_{3112} \\ 2S_{1211} & 2S_{1222} & 2S_{1233} & 4S_{1223} & 4S_{1231} & 4S_{1212} \end{bmatrix} \begin{bmatrix} \sigma_{11} \\ \sigma_{22} \\ \sigma_{33} \\ \sigma_{23} \\ \sigma_{31} \\ \sigma_{12} \end{bmatrix} \tag{B.4}$$

B.2 Bechterew basis

In writing Hooke's law with Voigt notation, we deal with a basis that is incompatible with the equality: $\mathbb{S} = \mathbb{C}^{-1}$ because of $\overline{S} \neq \overline{C}^{-1}$.

To overcome this, we construct an orthonormal basis (B_I) proposed in 1926

by Bechterew [5]:

$$\begin{aligned} B_1 &= \mathbf{e}_1 \otimes \mathbf{e}_1 \\ B_2 &= \mathbf{e}_2 \otimes \mathbf{e}_2 \\ B_3 &= \mathbf{e}_3 \otimes \mathbf{e}_3 \\ B_4 &= \frac{1}{\sqrt{2}}(\mathbf{e}_2 \otimes \mathbf{e}_3 + \mathbf{e}_3 \otimes \mathbf{e}_2) \\ B_5 &= \frac{1}{\sqrt{2}}(\mathbf{e}_3 \otimes \mathbf{e}_1 + \mathbf{e}_1 \otimes \mathbf{e}_3) \\ B_6 &= \frac{1}{\sqrt{2}}(\mathbf{e}_1 \otimes v\mathbf{e}_2 + \mathbf{e}_2 \otimes \mathbf{e}_1) \end{aligned} \tag{B.5}$$

The components of the stress tensor $\overline{\sigma}$ and the strain tensor $\overline{e}$ are noted as $\widehat{\sigma}$ and $\widehat{e}$:

$$\widehat{\sigma} = \begin{bmatrix} \sigma_{11} \\ \sigma_{22} \\ \sigma_{33} \\ \sqrt{2}\sigma_{23} \\ \sqrt{2}\sigma_{31} \\ \sqrt{2}\sigma_{12} \end{bmatrix} \qquad \text{and} \qquad \widehat{e} = \begin{bmatrix} e_{11} \\ e_{22} \\ e_{33} \\ \sqrt{2}e_{23} \\ \sqrt{2}e_{31} \\ \sqrt{2}e_{12} \end{bmatrix} \tag{B.6}$$

With the help of the Bechterew basis (B_I), the writing of the stiffness tensor $\mathbb{C}$ (respectively the compliance tensor $\mathbb{S}$) is represented by a matrix of size 6×6 denoted $\widehat{C}$ $(\widehat{S})$:

$$\widehat{C} = \begin{bmatrix} C_{1111} & C_{1122} & C_{1133} & \sqrt{2}C_{1123} & \sqrt{2}C_{1131} & \sqrt{2}C_{1112} \\ C_{1112} & C_{2222} & C_{2233} & \sqrt{2}C_{2223} & \sqrt{2}C_{2231} & \sqrt{2}C_{2212} \\ C_{1133} & C_{2233} & C_{3333} & \sqrt{2}C_{3323} & \sqrt{2}C_{3331} & \sqrt{2}C_{3312} \\ \sqrt{2}C_{1123} & \sqrt{2}C_{2223} & \sqrt{2}C_{3323} & 2C_{2323} & 2C_{2331} & 2C_{2312} \\ \sqrt{2}C_{1131} & \sqrt{2}C_{2231} & \sqrt{2}C_{3331} & 2C_{3123} & 2C_{3131} & 2C_{3112} \\ \sqrt{2}C_{1112} & \sqrt{2}C_{2212} & \sqrt{2}C_{3312} & 2C_{2312} & 2C_{3112} & 2C_{1212} \end{bmatrix} \tag{B.7}$$

This notation is faithful to the Hooke's law $\sigma_{ij} = C_{ijkl}\, e_{kl}$ in the sense that $\widehat{\sigma} = \widehat{C}\widehat{e}$ and $\widehat{e} = \widehat{S}\widehat{\sigma}$ with $\widehat{S} = \widehat{C}^{-1}$.

B.3 Special case of an isotropic elasticity tensor

The elasticity properties of an homogeneous isotropic linear elastic materials only determined by any two modulus among these:

- Kelvin parameters: k and μ,

- Lamé parameters: λ and μ,

- Young and Poisson parameters: E and ν.

Thus, given any two, any other of the elasticity modulus can be calculated according to the formulae given in the following table:

	E et ν	λ et μ	k et μ
E	E	$\mu\frac{3\lambda+2\mu}{\lambda+\mu}$	$\frac{9k\mu}{3k+\mu}$
ν	ν	$\frac{\lambda}{2(\lambda+\mu)}$	$\frac{3k-2\mu}{2(3k+\mu)}$
λ	$\frac{\nu E}{(1+\nu)(1-2\nu)}$	λ	$\frac{3k-2\mu}{3}$
μ	$\frac{E}{2(1+\nu)}$	μ	μ
k	$\frac{E}{3(1-2\nu)}$	$\frac{3\lambda+2\mu}{3}$	k

Table B.1: Conversion formulae for elasticity modulus.

Appendix C

Components of the Eshelby tensor for an inclusion in shape of sphere or ellipsoid of revolution

C.1 thermal conductivity problem

In the first part of this appendix, we are interested in the components of the Eshelby tensor in thermal conductivity case. Hatta and Taya have studied, in the manner of Eshelby, the problem of equivalent inclusion for the thermal conductivity of composites and deduced the analytical expressions of the Eshelby tensor for ellipsoidal or spherical inclusion [48].

The Eshelby tensor for inclusion i, denoted $\mathbb{S}_i^E$, is a second-order tensor in the basis $(\mathbf{e}_i \otimes \mathbf{e}_j)$: $\mathbb{S}_i^E = S_{ij}\mathbf{e}_i \otimes \mathbf{e}_j$. The tensor $\mathbb{S}_i^E$ is diagonal for an isotropic material.

Spherical inclusion

For a sphere, the Eshelby tensor is sample:

$$\begin{aligned} S_{ij} &= 0 \text{ if } i \neq j \\ S_{11} = S_{22} &= S_{33} = \frac{1}{3} \end{aligned} \tag{C.1}$$

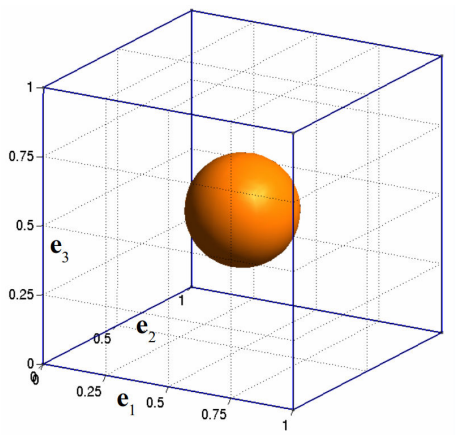

Figure C.1: A sphere inclusion in domain $[0,1]^3$

Oblate ellipsoidal inclusion

Let's consider $(\mathbf{e}_1, \mathbf{e}_2, \mathbf{e}_3)$ an orthonormal basis of $\mathbb{R}^3$.

The ellipsoid of revolution is rotated about $\mathbf{e}_3$ with semi-diameter a, b, c such that $a = b > c$. The aspect ratio $e = c/a$ define the form of the ellipsoid, see Figure C.2.

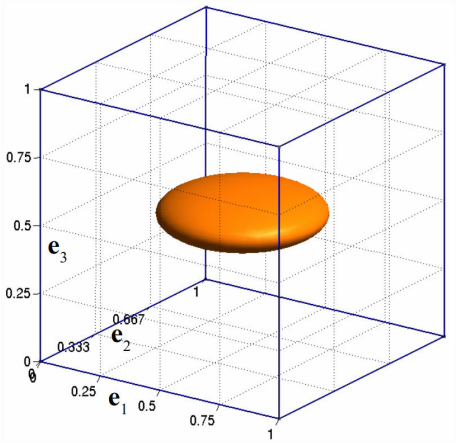

Figure C.2: An ellipsoid rotated about axis $\mathbf{e}_3$ with the aspect ratio $e < 1$

We give the analytical expression of the Eshelby tensor's components for the particular case of the ellipsoid of revolution with parameter a and e:

$$\begin{aligned} &S_{ij} = 0 \text{ if } i \neq j \\ &S_{11} = S_{22} = \frac{e}{2(1-e^2)^{3/2}} \left(acos(e) - e(1-e^2)^{1/2} \right) \\ &S_{33} = 1 - 2S_{22} \end{aligned} \tag{C.2}$$

Prolate ellipsoidal inclusion

Let's consider $(\mathbf{e}_1, \mathbf{e}_2, \mathbf{e}_3)$ an orthonormal basis of $\mathbb{R}^3$.

The ellipsoid of revolution is rotated about $\mathbf{e}_3$ with semi-diameter a, b, c such that $a = b < c$. The aspect ratio $e = c/a$ define the form of the ellipsoid, see Figure C.3.

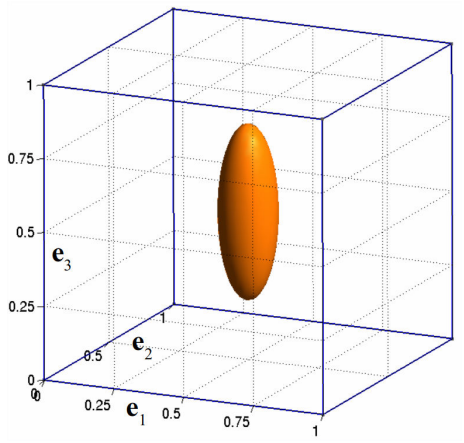

Figure C.3: An ellipsoid rotated about axis $\mathbf{e}_3$ with the aspect ratio $e > 1$

We find the expression of the Eshelby tensor's components:

$$\begin{aligned} S_{ij} &= 0 \text{ if } i \neq j \\ S_{11} = S_{22} &= \frac{e}{2(e^2-1)^{3/2}} \left(e(e^2-1)^{1/2} - acos(e) \right) \\ S_{33} &= 1 - 2S_{22} \end{aligned} \tag{C.3}$$

C.2 Linear elasticity problem

The second part gives the expressions of the Eshelby tensor for three dimensional linear elasticity problem. The results for a sphere or an ellipsoid of revolution given in the following come from the work Micromechanics of defects in solids of T. Mura [83], more precisely from the chapter on the Eshelby tensor referenced to [26–28].

The Eshelby tensor for inclusion i, denoted $\mathbb{S}_i^E$, is a fourth-order tensor in the basis $(\mathbf{e}_i \otimes \mathbf{e}_j \otimes \mathbf{e}_k \otimes \mathbf{e}_l)$: $\mathbb{S}_{Esh}^I = S_{ijkl}\mathbf{e}_i \otimes \mathbf{e}_j \otimes \mathbf{e}_k \otimes \mathbf{e}_l$.

Spherical inclusion

We have the components of Eshelby tensor in this case:

$$\begin{aligned} S_{1111} &= S_{2222} = S_{3333} = \frac{7-5\nu}{15(1-\nu)} \\ S_{1122} &= S_{2233} = S_{3311} = S_{1133} = S_{2211} = S_{3322} = \frac{5\nu-1}{15(1-\nu)} \\ S_{1212} &= S_{2323} = S_{3131} = \frac{4-5\nu}{15(1-\nu)} \end{aligned} \tag{C.4}$$

where ν denotes the Poisson's ratio of the isotropic matrix material.

Oblate ellipsoidal inclusion

Let's consider $(\mathbf{e}_1, \mathbf{e}_2, \mathbf{e}_3)$ an orthonormal basis of $\mathbb{R}^3$.

The ellipsoid of revolution is rotated about $\mathbf{e}_3$ with semi-diameter a, b, c such that $a = b > c$. The aspect ratio $e = c/a$ define the form of the ellipsoid, see Figure C.2.

Naturally, the ellipsoidal inclusion leads to a transversely isotropic tensor. The Eshelby tensor is determined from six coefficients, we introduce the following notations:

$$\begin{aligned} I_1 &= \frac{2\pi e}{(1-e^2)^{3/2}}\left(acos(e) - e\left(1-e^2\right)^{1/2}\right) \\ I_3 &= 4\pi - 2I_1 \\ I_{13} &= \frac{I_1 - I_3}{3(e^2-1)} \\ I_{12} &= \frac{\pi}{3} - \frac{I_{13}}{4} \\ I_{11} &= 3I_{12} \\ I_{33} &= \frac{4\pi}{3e^2} - 2I_{13} \end{aligned} \tag{C.5}$$

The non-zero components of the Eshelby tensor is deduced as below:

$$\begin{aligned} S_{1111} &= QI_{11} + RI_1 \\ S_{3333} &= Qe^2I_{33} + RI_3 \\ S_{1122} &= QI_{12} - RI_1 \\ S_{1133} &= Qe^2I_{13} + RI_1 \\ S_{3311} &= QI_{13} - RI_3 \\ S_{2323} &= \frac{Q}{2}(1+e^2)I_{13} + \frac{R}{2}(I_1 + I_3) \\ S_{1212} &= \frac{1}{2}(S_{1111} - S_{1122}) \end{aligned} \tag{C.6}$$

with

$$Q = \frac{3}{8\pi(1-\nu)} \ , \ R = \frac{1-2\nu}{8\pi(1-\nu)}$$

The other non-zero components are obtained from (C.6) by permutation between the axis $\mathbf{e}_1$ and the axis $\mathbf{e}_2$ (the property of the transversely isotropic, for example $S_{2222} = S_{1111}$ or $S_{1313} = S_{2323}$ etc...) and by a permutation between the first two indices or the last two indices (the property of minor symmetry $S_{ijkl} = S_{jikl} = S_{ijlk}$). All components can not be obtained by this permutation are null (for example, $S_{1232} = S_{1223} = S_{1112} = 0$).

Other writings of the Eshelby tensor can be found in the works of Chow [18] or Dormieux [21].

Prolate ellipsoidal inclusion

The ellipsoid of revolution is rotated about $\mathbf{e}_3$ with semi-diameter a, b, c such that $a = b < c$. The aspect ratio $e = c/a$ is greater than 1 in this case, see Figure C.3.

The components of the Eshelby tensor are almost identical to the oblate case (C.6), except the expression of I_1:

$$I_1 = \frac{2\pi e}{(e^2-1)^{3/2}} \left(e \left(e^2 - 1 \right)^{1/2} - cosh^{-1}(e) \right) \tag{C.7}$$

List of Abbreviations

RVE	**R**epresentative **V**olume **E**lement
FEM	**F**inite **E**lement **M**ethod
XFEM	e**X**tended **F**inite **E**lement **M**ethod
PFEM	**P**hantom domain **F**inite **E**lement **M**ethod
FCM	**F**inite **C**ell **M**ethod
FFT	**F**ast **F**ourier **T**ransform
MT	**M**ori - **T**anaka model
SC	**S**elf - **C**onsistent model
DOFs	**D**egrees **O**f **F**reedom
KUBC	**K**inetic **U**niform **B**oundary **C**ondition
SUBC	**S**tatic **U**niform **B**oundary **C**ondition
cub8	eight-node hexahedral element
qua4	four-node quadrilateral element

List of Symbols

div	divergence differential operator
∇	gradient differential operator
.	dot product operator
:	double dot product operator
$\langle \bullet \rangle_P$	average operator on P, $\langle \bullet \rangle_P = \frac{1}{\|P\|} \int_P \bullet dy$
δ_{ij}	Kronecker delta
u	temperature
$\mathbf{q}$	heat flow
f	heat source
Λ_{mat}	thermal conductivity tensor for the matrix phase
Λ_{inc}	thermal conductivity tensor for the inclusion phase
Λ_i	thermal conductivity tensor for phase i of composite
Λ^{eff}	effective thermal conductivity tensor
Λ^{MT}	effective thermal conductivity tensor calculated by Mori-Tanaka model
Λ^{SC}	effective thermal conductivity tensor calculated by self-consistent model
Λ^{kubc}	effective thermal conductivity tensor computed with kinematic uniform boundary condition
Λ^{subc}	effective thermal conductivity tensor computed with static uniform boundary condition
Λ^{hom}	homogenized thermal conductivity tensor
λ	thermal conductivity coefficient
$c_{thermal}$	contrast parameter in the thermal case
$\mathbf{u}$	displacement field

$\overline{\sigma}$	stress tensor
$\overline{e}$	strain tensor
$\mathbb{C}_{mat}$	stiffness tensor for the matrix phase
$\mathbb{C}_{inc}$	stiffness tensor for the inclusion phase
$\mathbb{C}_i$	stiffness tensor for phase i of composite
$\mathbb{C}^{eff}$	effective stiffness tensor
$\mathbb{S}$	compliance tensor
$\mathbb{A}$	strain concentration tensor
$c_{elastic}$	contrast parameter in the elastic case
E	Young's modulus
ν	Poisson's ratio
k	bulk modulus
μ	shear modulus
$\mathbb{S}_i^E$	Eschelby tensor of the inclusion i
V_i	volume of the inclusion i
ρ	volume fraction of the inclusion
ε	characteristic length of an RVE
$\mathbb{G}$	Green's function
$\overline{\tau}$	polarization tensor
$\boldsymbol{\xi}$	Fourier space variable
$\widehat{f}$	quantity f in the Fourier space
Ω	domain
Ω_{inc}	domain of the inclusion phase
P	periodic domain
P_{inc}	periodic domain of the inclusion phase
H^1	Sobolev space
J	quadratic energy functional
S	substitution matrix
$\mathbb{I}$	identity matrix
N_{rve}	RVE mesh resolution
h_{rve}	characteristic length of an element of the RVE mesh

h_{inc}	characteristic length of an element of the inclusion mesh
η	characteristic length ratio between RVE mesh and inclusion mesh

List of Figures

Bibliography

[1] Allaire, G. Homogenization and Two-Scale Convergence. SIAM Journal on Mathematical Analysis 23, 6 (Nov. 1992), 1482–1518.

[2] Allaire, G., and Brizzi, R. A Multiscale Finite Element Method for Numerical Homogenization. Multiscale Modeling & Simulation 4, 3 (Jan. 2005), 790–812.

[3] Barbe, F., Decker, L., Jeulin, D., and Cailletaud, G. Intergranular and intragranular behavior of polycrystalline aggregates. Part 1: F.E. model. International Journal of Plasticity 17, 4 (Jan. 2001), 513–536.

[4] Bathe, K.-J. Finite Element Procedures. Prentice Hall, 1996.

[5] Bechterew, P. Analytical study of the generalized hooke's law. application of the method of coordinate transformation. Zh Russ Fiz-khim Obshch Leningrad Univ Fizika 58, 3 (1926), 415–446.

[6] Belytschko, T., Gracie, R., and Ventura, G. A review of extended/generalized finite element methods for material modeling. Modelling and Simulation in Materials Science and Engineering 17, 4 (2009).

[7] Bensoussan, A., Lions, J.-L., and Papanicolaou, G. Asymptotic analysis for periodic structures. North-Holland Publishing Company, 1978.

[8] Benveniste, Y. A new approach to the application of Mori-Tanaka's theory in composite materials. Mechanics of Materials 6, 2 (June 1987), 147–157.

[9] Bezrukov, A., and Stoyan, D. Simulation and Statistical Analysis of Random Packings of Ellipsoids. Particle & Particle Systems Characterization 23, 5 (Dec. 2006), 388–398.

[10] Bigg, D. M. Thermal conductivity of heterophase polymer compositions. In Thermal and Electrical Conductivity of Polymer Materials, vol. 119. Springer-Verlag, Berlin/Heidelberg, 1995, pp. 1–30.

[11] Bornert, M., Bretheau, T., and Gilormini, P. Homogénéisation en mécanique des matériaux, Tome 1 : Matériaux aléatoires élastiques et milieux périodiques. Hermes science, 2001.

[12] Bourgeois, S., Cartraud, P., and Débordes, O. Homogenization of periodic sandwiches. Mechanics of Sandwich Structures (1998), 131–138.

[13] Brisard, S., Dormieux, L., and Sab, K. A variational form of the equivalent inclusion method for numerical homogenization. International Journal of Solids and Structures 51, 3-4 (Feb. 2014), 716–728.

[14] Bucataru, I., and Slawinski, M. A. Invariant Properties for Finding Distance in Space of Elasticity Tensors. Journal of Elasticity 94, 2 (Feb. 2009), 97–114.

[15] Buryachenko, V. Micromechanics of Heterogeneous Materials. Springer, 2007.

[16] Caillerie, D. Thin elastic and periodic plates. Math. Meth. in the Appl. Sci. 6 (1984), 159–191.

[17] Chikhi, M., Agoudjil, B., Haddadi, M., and Boudenne, A. Numerical modelling of the effective thermal conductivity of heterogeneous materials. Journal of Thermoplastic Composite Materials 26, 3 (Apr. 2013), 336–345.

[18] Chow, T. S. Elastic moduli of filled polymers: The effect of particle shape. Journal of Applied Physics 48, 10 (Oct. 1977), 4072–4075.

[19] Cowin, S. C., and Mehrabadi, M. M. On the identification of material symmetry for anisotropic elastic materials. The Quarterly Journal of Mechanics and Applied Mathematics 40, 4 (1987), 451–476.

[20] Decolon, C. Analysis of Composite Structures. Kogan Page Science, London, 2002.

[21] Dormieux, L., Kondo, D., and Ulm, F. Microporomechanics. Wiley, 2006.

[22] Drugan, W., and Willis, J. A micromechanics-based nonlocal constitutive equation and estimates of representative volume element size for elastic composites. Journal of Mechanics and Physics of Solids 44, 4 (1996), 497–524.

[23] Duan, H. L., and Karihaloo, B. L. Effective thermal conductivities of heterogeneous media containing multiple imperfectly bonded inclusions. Physical Review B 75, 6 (Feb. 2007).

[24] Débordes, O. Homogenization computations in the elastic or plastic collapse range. applications to unidirectionnal composites and perforated sheets. Proceedings of the 4th International Symposium Innovative Numerical Methods in Engineering (1986), 453–458.

[25] Düster, A., Sehlhorst, H.-G., and Rank, E. Numerical homogenization of heterogeneous and cellular materials utilizing the finite cell method. Computational Mechanics 50, 4 (Oct. 2012), 413–431.

[26] Eshelby, J. D. The Determination of the Elastic Field of an Ellipsoidal Inclusion, and Related Problems. Proceedings of the Royal Society of London. Series A, Mathematical and Physical Sciences 241, 1226 (1957), 376–396.

[27] Eshelby, J. D. The Elastic Field Outside an Ellipsoidal Inclusion. Proceedings of the Royal Society of London. Series A, Mathematical and Physical Sciences 252, 1271 (1959), 561–569.

[28] Eshelby, J. D. Elastic inclusions and inhomogeneities. Progress in Solid Mechanics 2 (1961), 89–140.

[29] Eyre, D. J., and Milton, G. W. A fast numerical scheme for computing the response of composites using grid refinement. The European Physical Journal Applied Physics 6, 1 (Apr. 1999), 41–47.

[30] Feyel, F. Multiscale FE2 elastoviscoplastic analysis of composite structures. Computational Materials Science 16, 1-4 (Dec. 1999), 344–354.

[31] Francfort, G. A., and Murat, F. Homogenization and optimal bounds in linear elasticity. Archive for Rational Mechanics and Analysis 94, 4 (1986), 307–334.

[32] François, M. Bases de tenseurs. In Ecole d'été MatSyMat (Nantes, 2014).

[33] Fries, T., and Belytschko, T. The extended / generalized finite element method: An overview of the method and its applications. Int. J. Numer. Methods. Eng. 84, 3 (2010), 253–304.

[34] Geuzaine, C., and Remacle, J.-F. Gmsh: A 3-D finite element mesh generator with built-in pre- and post-processing facilities. International Journal for Numerical Methods in Engineering 79, 11 (Sept. 2009), 1309–1331.

[35] Ghossein, E., and Lévesque, M. A fully automated numerical tool for a comprehensive validation of homogenization models and its application to spherical particles reinforced composites. International Journal of Solids and Structures 49, 11-12 (June 2012), 1387–1398.

[36] Girault, V., and Glowinski, R. Error analysis of a fictitious domain method applied to a Dirichlet problem. Japan Journal of Industrial and Applied Mathematics 12, 3 (1995), 487–514.

[37] Gitman, I., Askes, H., and Sluys, L. Representative volume : existence and size determination. Engineering Fracture Mechanics 74 (2007), 2518–2534.

[38] Glowinski, R., Pan, T.-W., and Periaux, J. A fictitious domain method for Dirichlet problem and applications. Computer Methods in Applied Mechanics and Engineering 111, 3-4 (Jan. 1994), 283–303.

[39] Glowinski, R., Pan, T. W., Periaux, J., and Ravachol, M. A fictitious domain method for the incompressible Navier-Stokes equations. In The finite element method in the 1990's. Springer, 1991, pp. 410–417.

[40] Hashin, Z. The elastic moduli of heterogeneous materials. Journal of Applied Mechanics 29 (1962), 143–150.

[41] Hashin, Z. Analysis of Composite Materials—A Survey. Journal of Applied Mechanics 50, 3 (1983), 481.

[42] Hashin, Z., and Shtrikman, S. A variational approach to the theory of the elastic behaviour of multiphase materials. Journal of the Mechanics and Physics of Solids 11, 2 (Mar. 1963), 127–140.

[43] Haslinger, J., and Renard, Y. A new fictitious domain approach inspired by the extended finite element method. SIAM Journal on Numerical Analysis 47, 2 (2009), 1474–1499.

[44] Herve, E. Thermal and thermoelastic behaviour of multiply coated inclusion-reinforced composites. International Journal of Solids and Structures 39, 4 (Feb. 2002), 1041–1058.

[45] Herve, E., and Zaoui, A. n-layered inclusion-based micromechanical modelling. International Journal of Engineering Science 31, 1 (1993), 1 – 10.

[46] Hill, R. Elastic properties of reinforced solids: Some theoretical principles. Journal of the Mechanics and Physics of Solids 11, 5 (Sept. 1963), 357–372.

[47] Hill, R. A self-consistent mechanics of composite materials. Journal of the Mechanics and Physics of Solids 13, 4 (Aug. 1965), 213–222.

[48] Hiroshi, H., and Minoru, T. Equivalent inclusion method for steady state heat conduction in composites. International Journal of Engineering Science 24, 7 (Jan. 1986), 1159–1172.

[49] Hoang, D. Contribution à l'homogénéisation de matériaux hétérogènes viscoélastiques. Milieux aléatoires et périodiques et prise en compte des interfaces. PhD thesis, Université Paris-Est Marne la Vallée, 2011.

[50] Hollister, S. J., and Kikuchi, N. A comparison of homogenization and standard mechanics analyses for periodic porous composites. Computational Mechanics 10, 2 (1992), 73–95.

[51] Hounkpati, V., Salnikov, V., Vivet, A., and Karamian, P. On the choice of homogenization method to achieve effective mechanical properties of composites reinforced by ellipsoidal and spherical particles, 2017.

[52] Huynh, Q. V. Estimation des propriétés poromécaniques effectives des argilites : apport des méthodes d'homogénéisation. PhD thesis, Institut national polytechnique de Lorraine, 2006.

[53] Kanit, T., Forest, S., Galliet, I., Mounoury, V., and Jeulin, D. Determination of the size of the representative volume element for random composites: statistical and numerical approach. International Journal of Solids and Structures 40, 13-14 (June 2003), 3647–3679.

[54] Kari, S., Berger, H., Rodriguez-Ramos, R., and Gabbert, U. Computational evaluation of effective material properties of composites reinforced by randomly distributed spherical particles. Composite Structures 77, 2 (Jan. 2007), 223–231.

[55] Kielbasiewicz, N. Introduction à Gmsh, Oct. 2013.

[56] Kröner, E. Statistical Continuum Mechanics. Springer-Verlag, 1972.

[57] Le Bris, C. Systèmes multi-échelles : modélisation et simulation. Mathématiques & Applications. Springer, Berlin, Heidelberg, New York, 2005.

[58] Le Bris, C. Some Numerical Approaches for Weakly Random Homogenization. In Numerical Mathematics and Advanced Applications 2009, G. Kreiss, P. Lötstedt, A. Målqvist, and M. Neytcheva, Eds. Springer Berlin Heidelberg, Berlin, Heidelberg, 2010, pp. 29–45.

[59] Le Bris, C., Legoll, F., and Thomines, F. Multiscale Finite Element approach for "weakly" random problems and related issues. ESAIM: Mathematical Modelling and Numerical Analysis 48, 3 (May 2014), 815–858.

[60] Le-Quang, H., Bonnet, G., and He, Q.-C. Size-dependent Eshelby tensor fields and effective conductivity of composites made of anisotropic phases with highly conducting imperfect interfaces. Physical Review B 81, 6 (Feb. 2010).

[61] Legoll, F., and Thomines, F. On a variant of random homogenization theory: convergence of the residual process and approximation of the homogenized coefficients. ESAIM: Mathematical Modelling and Numerical Analysis 48, 2 (Mar. 2014), 347–386.

[62] Legrain, G., Chevreuil, M., and Takano, N. Prediction of apparent properties with uncertain material parameters using high-order fictitious domain methods and PGD model reduction. International Journal for Numerical Methods in Engineering 109, 3 (Jan. 2017), 345–367.

[63] Lemaitre, S. Modélisation des matériaux composites multiphasiques à microstructures complexes. Étude des propriétés effectives par des méthodes d'homogénéisation. PhD thesis, Université de CAEN Normandie, 2017.

[64] Lemaitre, S., Salnikov, V., Choï, D., and Karamian-Surville, P. Influence of morphological parameters in 3D composite materials on their effective thermal properties and comparison with effective mechanical properties. soumis à IJSS (2016).

[65] Lian, W.-D., Legrain, G., and Cartraud, P. Image-based computational homogenization and localization: comparison between X-FEM/levelset and voxel-based approaches. Computational Mechanics 51, 3 (2013), 279–293.

[66] Magoariec, H. Adaptation élastoplastique et homogénéisation périodique. PhD thesis, Université de la méditerranée, 2003.

[67] Melenk, J., and Babuška, I. The partition of unity finite element method: Basic theory and applications. Computer Methods in Applied Mechanics and Engineering 139, 1-4 (Dec. 1996), 289–314.

[68] Michel, J., Moulinec, H., and Suquet, P. Effective properties of composite materials with periodic microstructure: a computational approach. Computer Methods in Applied Mechanics and Engineering 172, 1-4 (Apr. 1999), 109–143.

[69] Michel, J. C., Moulinec, H., and Suquet, P. A Computational Method Based on Augmented Lagrangians and Fast Fourier Transforms for Composites with High Contrast. CMES 1, 2 (2000), 79–88.

[70] Michel, J. C., Moulinec, H., and Suquet, P. A computational scheme for linear and non-linear composites with arbitrary phase contrast. International Journal for Numerical Methods in Engineering 52, 12 (2001), 139–160.

[71] Milton, G. W. The Theory of Composites. Cambridge University Press, May 2002.

[72] Mishnaevsky, L. L. Automatic voxel-based generation of 3d microstructural FE models and its application to the damage analysis of composites. Materials Science and Engineering: A 407, 1-2 (Oct. 2005), 11–23.

[73] Moakher, M., and Norris, A. N. The Closest Elastic Tensor of Arbitrary Symmetry to an Elasticity Tensor of Lower Symmetry. Journal of Elasticity 85, 3 (Oct. 2006), 215–263.

[74] Monchiet, V., and Bonnet, G. A polarization-based FFT iterative scheme for computing the effective properties of elastic composites with arbitrary contrast. International Journal for Numerical Methods in Engineering 89, 11 (Mar. 2012), 1419–1436.

[75] Monchiet, V., and Bonnet, G. Numerical homogenization of nonlinear composites with a polarization-based FFT iterative scheme. Computational Materials Science 79 (Nov. 2013), 276–283.

[76] Mori, T., and Tanaka, K. Average stress in matrix and average elastic energy of materials with misfitting inclusions. Acta Metallurgica 21, 5 (May 1973), 571–574.

[77] Moulinec, H., and Silva, F. Comparison of three accelerated FFT-based schemes for computing the mechanical response of composite materials. International Journal for Numerical Methods in Engineering 97, 13 (Mar. 2014), 960–985.

[78] Moulinec, H., and Suquet, P. A fast numerical method for computing the linear and nonlinear properties of composites. C.R.Acad.Sc. Paris Tome 2 (1994), 1417 – 1423.

[79] Moulinec, H., and Suquet, P. A FFT based-numerical method for computing the mechanical properties of composites from images of their microstructure. R.Pyrz, Ed.,Microstructure-Property Interactions in Composites Materials, 1995.

[80] Moulinec, H., and Suquet, P. A numerical method for computing the overall response of nonlinear composites with complex microstructure. Computer Methods in Applied Mechanics and Engineering 157, 1-2 (Apr. 1998), 69–94.

[81] Moës, N., Cloirec, M., Cartraud, P., and Remacle, J.-F. A computational approach to handle complex microstructure geometries. Comput. Meth. Appl. Mech. Eng. 192 (2003), 3163–3177.

[82] Moës, N., Dolbow, J., and Belytschko, T. A finite element method for crack growth without remeshing. International Journal for Numerical Methods in Engineering 46, 1 (Sept. 1999), 131–150.

[83] Mura, T., N.-N. S., and Oravas, G. Micromechanics of defects in solids, vol. 3 of Mechanics of Elastic and Inelastic Solids. Springer Netherlands, Dordrecht, 1987.

[84] Nguyen, T. K. Numerical homogenization of periodic stuctures by Fourier transform : composite materials and porous media. PhD thesis, Université Paris-Est, dec 2010.

[85] Norris, A. A differential scheme for the effective moduli of composites. Mechanics of Materials 4, 1 (Mar. 1985), 1–16.

[86] Ostoja-Starzewski, M. Random field models of heterogeneous materials. International Journal of Solids and Structures 35, 19 (1998), 2429–2455.

[87] Parvizian, J., Düster, A., and Rank, E. Finite cell method: h- and p-extension for embedded domain problems in solid mechanics. Computational Mechanics 41, 1 (Sept. 2007), 121–133.

[88] Ramière, I., A.-P., and Belliard, M. A fictitious domain approach with spread interface for elliptic problems with general boundary conditions. Computer Methods in Applied Mechanics and Engineering 225 (2007), 766–781.

[89] Reine, B. Étude et simulation de la conductivité thermique de matériaux composites à matrice organique chargée et renforcée de fibres de carbone PITCH. PhD thesis, Université Toulouse 3 Paul Sabatier, 2014.

[90] Rektorys, K. Existence of the weak solution of a boundary value problem. v-ellipticity. the lax-milgram theorem. Variational Methods in Mathematics, Science and Engineering (1977), 383 – 398.

[91] Reuss, A. Calculation of the flow limits of mixed crystals on the basis of the plasticity of monocrystals. Zeitschrift fur Angewandte Mathematik und Mechanik, 9 (1929), 49–58.

[92] Salnikov, V., Choï, D., and Karamian-Surville, P. On efficient and reliable stochastic generation of RVEs for analysis of composites within the framework of homogenization. Computational Mechanics 55, 1 (Jan. 2015), 127–144.

[93] Salnikov, V., Lemaitre, S., Choï, D., and Karamian-Surville, P. Measure of combined effects of morphological parameters of inclusions within composite materials via stochastic homogenization to determine effective mechanical properties. Composite Structures 129 (2015), 122 – 131.

[94] Sanchez-Palencia, E. Non-Homogeneous Media and Vibration Theory. Lecture Notes in Physics. Springer, Berlin, 1980.

[95] Sanchez-Palencia, E., and Sanchez-Hubert, J. Introduction aux méthodes asymptotiques et à l'homogénéisation - Application à la mécanique des milieux continus. Masson, 1992.

[96] Schneider, K., K.-B., and Bargmann, S. Automatic three-dimensional geometry and mesh generation of periodic representative volume elements for matrix-inclusion composites. Advances in Engineering Software 99 (2016), 177 – 188.

[97] Segurado, J., and Llorca, J. A numerical approximation to the elastic properties of sphere-reinforced composites. Journal of the Mechanics and Physics of Solids 50, 10 (Oct. 2002), 2107–2121.

[98] Springer, G. S., and Tsai, S. W. Thermal Conductivities of Unidirectional Materials. Journal of Composite Materials 1, 2 (apr 1967), 166–173.

[99] Stránský, J., Vorel, J., Zeman, J., and Šejnoha, M. Mori-Tanaka Based Estimates of Effective Thermal Conductivity of Various Engineering Materials. Micromachines 2, 2 (Apr. 2011), 129–149.

[100] Sukumar, N., Chopp, D. L., Moës, N., and Belytschko, T. Modeling holes and inclusions by level sets in the extended finite-element method. Computer methods in applied mechanics and engineering 190, 46 (2001), 6183–6200.

[101] Tran, A. B., Yvonnet, J., He, Q.-C., Toulemonde, C., and Sanahuja, J. A multiple level set approach to prevent numerical artefacts in complex microstructures with nearby inclusions within XFEM. International Journal for Numerical Methods in Engineering 85, 11 (Mar. 2011), 1436–1459.

[102] Voigt, W. Ueber die Beziehung zwischen den beiden Elasticitätsconstanten isotroper Körper. Annalen der Physik 274, 12 (1889), 573–587.

[103] Wiener, O. Die theorie des mischkörpers für das feld der stationären strömung : Die mittelwertsätze für kraft. Polarisation und Energie 1 (1913).

[104] Willis, J. Bounds and self-consistent estimates for the overall properties of anisotropic composites. Journal of the Mechanics and Physics of Solids 25, 3 (June 1977), 185–202.

[105] Yvonnet, J. A fast method for solving microstructural problems defined by digital images: a space Lippmann–Schwinger scheme. International Journal for Numerical Methods in Engineering 92, 2 (2012), 178–205.

[106] Yvonnet, J., Quang, H. L., and He, Q. C. An XFEM/level set approach to modelling surface/interface effects and to computing the size-dependent effective properties of nanocomposites. Computational Mechanics 42, 1 (Apr. 2008), 119–131.

[107] Zaoui, A. Plasticité: approches en champ moyen. In Homogénéisation en mécanique des matériaux, Tome 2 : Comportements non linéaires et problèmes ouverts (chap. 5), M. Bornert, T. Bretheau, and P. Gilormini, Eds. Hermes science, 2001, pp. 17–44.

[108] Zohdi, T. I., and Wriggers, P., Eds. An Introduction to Computational Micromechanics, vol. 20 of Lecture Notes in Applied and Computational Mechanics. Springer Berlin Heidelberg, Berlin, Heidelberg, 2005.